

本科生毕业设计(论文)

脉石英制备半导体及光伏级高纯石英砂 工艺流程设计

Process Design of Preparing Semiconductor and Photovoltaic Grade High Purity Quartz Sand by Vein Quartz

作者:刘琦导师:任伊苏

中国矿业大学 2025年6月

中国矿业大学 本科生毕业设计(论文)

脉石英制备半导体及光伏级高纯石英砂 工艺流程设计

Process Design of Preparing Semiconductor and Photovoltaic Grade High Purity Quartz Sand by Vein Quartz

| 作 | 者刘琦 | 学 | 号 | 01210111 |
|---|---------|---|---|----------|
| 导 | 师任伊苏 | 职 | 称 | 准聘副教授 |
| 学 | 院矿业工程学院 | 专 | 业 | 新能源科学与工程 |

毕业设计(论文)原创性声明

本人郑重声明:所呈交的毕业设计(论文)《脉石英制备半导体及光伏级高纯石英砂工艺流程设计》,是本人在指导教师指导下,在中国矿业大学攻读学位期间进行的研究工作所取得的成果。据我所知,除文中已经标明引用的内容外,本论文不包含任何其他个人或集体已经发表或撰写过的研究成果。本人完全意识到本声明的法律结果由本人承担。

作者签名: 刘琦 2025年06月10日

中国矿业大学

本科毕业设计(论文)诚信承诺书

本人郑重声明: 所呈交的毕业设计(论文)是本人在导师的指导下独立进行研究所取得的成果。尽我所知,除了文中特别加以标注和致谢的内容外,本设计(论文)不包含任何其他个人或集体已经发表或撰写的成果作品。对本设计(论文)所涉及的研究工作作出贡献的其他个人和集体,均已在文中以明确方式标明。

作者签名: 刘琦 2025 年 06 月 10 日

中国矿业大学 毕业设计(论文)使用授权声明

本人完全了解中国矿业大学有关收集、保留和使用本人所送交的毕业设计 (论文)的规定,即:本科生在校攻读学位期间毕业设计(论文)工作的知识产 权单位属中国矿业大学。学校有权保留并向国家有关部门或机构送交毕业设计 (论文)的复印件和电子版,允许论文被查阅和借阅,可以公布论文的全部或部 分内容,可以采用影印、缩印或扫描等复制手段保存、汇编论文。保密的论文在 解密后适用本声明。

论文涉密情况:

☑ 不保密

□ 保密, 保密期(起讫日期:

作者签名: 刘琦 2025年06月10日 导师签名: 任伊苏 2025 年 06 月 10 日

)

致谢

行文至此, 惊觉四载春秋匆匆流逝, 感谢旅途上遇见的每一个人。

感谢我的父母,感谢他们数十年如一日的理解支持与尊重,感谢从我呱呱坠 地开始地爱护和包容,感谢在我每一个崩溃的夜里安慰我的怀抱,感谢每一顿从 早上五点开始做起的早餐,感谢每一晚回家后陪伴,感谢他们给予我一往无前的 勇气和奔赴山海的能力,感谢他们对我的爱。

感谢我的姐姐和姐夫,感谢他们一直以来对我的支持和帮助,感谢他们对我生活无微不至的照顾,感谢每一次在机场的深夜等候,感谢无数次的默默守护,感谢他们对我的信任和爱。

感谢我的导师任伊苏老师对我毕业设计的悉心指导与大力支持。从论文的选 题立意、研究框架的构建、关键问题的解决到最终的修改定稿,每一步都凝聚着 老师的心血。感谢老师在我试验遇到困难时提供关键性的指导与无私的帮助。

感谢我的朋友们,感谢折枝,鹿鹿在我每一次坏情绪时的劝解,感谢我们一起经历的七年,感谢我们长长久久的未来。感谢桂林理工大学的李同学在我每次低谷时投喂的蛋糕和礼物。感谢 2092 全体成员,感谢遇见,让我拥有了美好的大学时光。感谢其他未提到的朋友,我爱你们。

感谢大学期间给予我帮助的每位老师,感谢你们对我的谆谆教诲和指导。 最后感谢我自己。

我坚信市场的能量只有未被挖掘,而不会因为竞争而饱和。我要不问前程地 投身自己的热爱,并在心中默念"你一直想做一个鲜活的人"你的坚持是因为 有一件事在等你,而我终于知道人人在说的竞争力,原来就是要用更多的坚持去 摆脱爱好者的流俗与肤浅。

感谢走的很慢但一直在向前的自己。

落幕的是我的大学生活, 而不是我依然有着千万种可能的人生。

感恩相遇, 愿万事顺遂。

中国矿业大学本科毕业设计(论文)任务书

设计(论文)题目:脉石英制备半导体及光伏级高纯石英砂工艺流程设计

| 学院 | 矿业工程学院 | 专业年级 | 新能源科学与工程 2021 级 |
|------|--------|------|--------------------|
| 学生姓名 | 刘琦 | 学号 | 01210111 |

1、设计(论文)的主要内容

- (1)了解高纯石英定义、高纯石英杂质危害及不同高纯砂产品的工艺要求;
- (2)了解石英中杂质的赋存状态、熟练高纯石英提纯的流程并进行实验:如物理(重选、磁选、浮选)、化学(煅烧-水淬、酸浸、氯化、高温掺杂)等除杂流程方法;
- (3) 对比分析国内外高纯石英矿床脉石英矿石原料,以 A1、Fe、K、Na、Ca、Mg 及总杂质金属元素的去除率为指标,选择合适的提纯工艺流程对脉石英进行提纯,找到 4N8 级以上脉石英型高纯石英矿源;
- (4) 研究矿石组成及结构,分析石英矿物学和流体包裹体特征,建立高纯石英原矿评价"基因检测";
- (5) 改变不同工艺流程的参数,如煅烧温度、酸液配比等,检测提纯高纯石英的杂质差异:
- (6) 对煅烧过程、酸浸过程、氯化过程进行宏观-微观分析,探索各个工艺流程中石英中杂质元素的迁移和净化机理等。

2、设计(论文)的基本要求

- (1) 学生在指导教师指导下独立完成论文,正文字数一般不少于 15000 字, 英语翻译原文不少于 7000 词,翻译成中文后不少于 3000 字,查阅参考文献不少于 20 篇,其中查阅的外文文献不少于 5 篇;
- (2) 学生注重分析问题、解决问题和创新思维能力的培养:
- (3) 学生恪守学术道德和学术规范。

设计(论文)的时间要求

- (1) 2024年12月26日前,完成选题报告的编写,并在系统内上传,制作PPT,进行选题汇报;
- (2)每周日前,学生在系统提交指导日志,指导老师审核,共需要提交至少12次指导日志:
- (3) 2025年3月20日前,上传中期设计(论文),制作PPT,进行中期汇报;

- (4) 2025年5月10日前,完成毕业设计(论文)的所有内容,进行知网查重,并在毕设系统上传设计(论文)定稿;
- (5) 2025 年 5 月 20 日前, 学生根据评审意见修改完善设计(论文)、上传设计(论文) 定稿、完成知网查重;
- (6) 2025年5月25日前,制作PPT,进行答辩;
- (7) 2025 年 6 月 3 日前,根据第一次答辩提出的意见,所有毕业设计(论文)完成修改和学术不端检测等工作,上传设计(论文)最终稿。

指导教师签字: 任伊苏

中国矿业大学毕业设计(论文)指导教师评阅书

| 学生姓名 | 刘琦 | 学号 | 01210111 |
|----------|---------|------|--------------|
| 设计(论文)题目 | 脉石英制备半导 | 体及光伏 | 级高纯石英砂工艺流程设计 |

指导教师评语(①基础理论及基本技能的掌握;②独立解决实际问题的能力;③研究内容的理论依据和技术方法;④取得的主要成果及创新点;⑤工作态度及工作量;⑥总体评价及建议成绩;⑦存在问题;⑧是否同意答辩等);

此次毕业设计结构完整、逻辑连贯、流程设计思路清晰,选取国内外不同产地 脉石英为原料,设计提纯工艺并结合分析方法,明确了不同原料的提纯效果及适用 领域,部分样品达到半导体及光伏级标准。

该设计以脉石英为研究对象,开展了制备半导体及光伏级高纯石英砂工艺流程设计。该同学搜集归纳相关文献,掌握了高纯石英砂提纯技术的研究现状与行业标准,对关键工艺的原理及作用机制进行了分析。该同学在数据处理、毕设论文撰写等方面展示了基本的科研素养。

此次毕业设计投入时间较短、因提纯测试环节耗时久,实验环节略有欠缺,所做实验内容不够完善;该同学在独立完成提纯及测试全流程实验方面有欠缺,不够 严谨认真,希望后续进行改进。

鉴于此次设计基本完成了毕业设计(论文)的要求,同意参加答辩。

成绩: 85.0

指导教师签字: 任伊苏 2025 年 06 月 03 日

中国矿业大学毕业设计(论文)评阅教师评阅书

| 学生姓名 | 刘琦 | 学号 | 01210111 |
|----------|---------|------|--------------|
| 设计(论文)题目 | 脉石英制备半导 | 体及光伏 | 级高纯石英砂工艺流程设计 |

评阅教师评语(①选题的意义;②基础理论及基本技能的掌握;③综合运用所学知识解决实际问题的能力;④工作量的大小;⑤取得的主要成果及创新点;⑥写作的规范程度;⑦总体评价及建议成绩;⑧存在问题;⑨是否同意答辩等);

评阅人1评阅意见:

该论文选题来源于高纯石英砂的制备工艺问题,研究提纯的综合工艺流程,不同工艺阶段石英的杂质去除效果、不同产地脉石英原矿品位及除杂效果等内容。该论文围绕高纯石英矿床分布特征和脉石英加工高纯石英研究方面开展了国内外研究现状综述。通过实验测试和理论分析方法,综合分析了脉石英提纯难点和质量标准要求、脉石英提纯工艺研究,样品提纯实验和不同工艺阶段石英的杂质去除效果等,在高纯石英砂的制备工艺流程方面有一定的指导意义,说明书写作较规范。建议修改内容:

- (1) 论文格式存在一定的不规范问题,如参考文献,表格,图等;
- (2) 研究内容出现"了解……"、"掌握……"等宽泛性用语,进行修改调整。
- (3) 第5章和第6章合并。
- (4) 第1.1 选题背景与意义,修改为"研究背景与意义",且细分为1.1.1 研究背景和1.1.2 研究意义,对该部分内容进行适当精简。
- (5) 章节题目是否可以进一步明确具体的研究内容。
- (6) 第2章缺少"本章小结"。

该论文对 "Trace element compositions and defect structures of high-purity quartz from the Southern Ural Region, Russia" 论文进行了翻译,翻译较准确。该生认真独立完成。整个论文表明作者具有扎实的专业知识和解决问题的能力,建议进行答辩。

评阅人2评阅意见:

毕业设计"脉石英制备半导体及光伏级高纯石英砂工艺流程设计"一文探讨了 国内外不同产地脉石英转化为高纯石英砂的潜力,文章采取一系列提纯工艺来实 现不同产地原料的杂质深度脱除,从而评价了对应来源地原料的利用方向。文章总 体认为所开展的工作提升了脉石英的纯度,并为高纯石英砂制备提供了方法。论文 总体工作量得当,研究目标清晰、研究手段合理、研究路线可行、论文整体结构脉 络均较为合理。文章在以下方向可进一步改进:

- (1) 文章格式与正式格式不一,建议作者以模板为准调整论文格式。
- (2) 英文中二氧化硅化学式表述不对,需要修正。
- (3) 论文多处对图表未有在正文中引用,如表 2-1,表 2-2,图 2-1,图 2-2等。
- (4) 文章部分图表需要修正,如表 2-4 中字体大小不一,表 2-6 中分列错误,表 2-5 中单位缺失等。
- (5) 关于显微镜分析脉石英部分,建议对样品处理方法进行简要叙述。

成绩: 85.0

95.0

评阅教师签字:严红

冯晓巍

2025年05月19日

中国矿业大学毕业设计(论文)答辩及综合成绩

| 答辩情 | 况 | | | | |
|--|----------|------|----------|----------|------|
| | | 回 2 | 答 | 可题 | |
| 提出问题 | 正确 | 基本正确 | 有一 般性 错误 | 有原 则性 错误 | 没有回答 |
| 技术路线图不清楚,且没有图名;缺少页眉横线;翻译部分摘要要放置在段前 | √ | | | | |
| 建议补充1节工艺流程,形成一套流程方法,体现出论文设计 | √ | | | | |
| 目录不需要设置段前段后;论文中的折线图需要进一步美化;部分图片需要标注引用。 | √ | | | | |

答辩委员会评语及建议成绩:

该生完成了《脉石英制备半导体及光伏级高纯石英砂工艺流程设计》毕业设计,选题具有较好的实际意义,汇报思路清晰、回答问题正确、说明书符合规范,翻译了《Trace Element Compositions and Defect Structures of High-Purity Quartz from the Southern Ural Region, Russia》,译文准确。答辩委员会委员一致认为,该设计达到了新能源科学与工程专业毕业设计(论文)的要求,说明作者具有良好的专业知识和解决复杂性问题的能力。

成绩: 90.0

答辩委员会主任签字: 张源 2025年06月08日

成绩评定:

| 成绩组成 | 指导教师 | 评阅教师 | 答辩成绩 | 其他 | 总评 |
|------|------|-------|------|------|----|
| 成绩比例 | 0.13 | 0. 27 | 0.60 | 0.00 | |
| 评分 | 85.0 | 90.0 | 90.0 | 0 | 优秀 |

学院领导签字:

2025年06月08日

摘要

高纯石英砂是半导体及光伏产业的关键材料,其纯度影响着高端产品的性能。 我国脉石英储量丰富,但矿床品质低,提纯技术存在短板,使得国产高纯石英砂 难以满足半导体与光伏行业的需求。针对这一现状,本文选取国内外不同产地脉 石英作为原料,设计高纯石英砂的制备工艺。

本文设计煅烧-水淬、磨矿-筛分、磁选、浮选、酸洗及氯化的综合提纯工艺。 煅烧-水淬(1050℃)能够有效破坏流体包裹体并降低石英机械强度,磁选利用磁 性差异去除石英中的铁磁性杂质,在酸性条件下,浮选利用捕收剂与抑制剂,实 现石英与长石、云母的高效分离,酸洗使用 HCl:HF:HNO₃=3:1:1 的混合酸,显著 降低金属杂质,氯化通过高温氯气反应去除碱金属(Na、K、Li),实现杂质深 度脱除。

本文结合矿物学分析、ICP-OES 检测及显微镜下分析,系统评估了非洲(LQBS-1)、印度(LQBS-2)、贵州(LQBS-3)及黑龙江(LQBS-4及 LQBS-5)脉石英的提纯潜力。试验表明:非洲脉石英(LQBS-1)经处理后总杂质含量降至 8.75ppm,SiO₂纯度达 99.999%(5N 级),满足半导体及光伏级高纯石英砂标准(总杂质<20ppm),其中 Al、Fe 等关键杂质分别降至 4.68ppm 和 0.53ppm,仅需进一步优化 Ca 含量即可用于半导体砂;印度脉石英总杂质降至 9.95ppm,SiO₂纯度达 5N 级,满足半导体及光伏级高纯石英砂标准(总杂质<20ppm);贵州脉石英总杂质为 40.50ppm,SiO₂纯度达 4N6 级(99.996%),可作为乳白坨料使用;黑龙江脉石英因提纯后仍无法满足高纯标准,仅适用于工业硅等低端领域。

本文对比国际高端产品标准,非洲与印度样品已接近尤尼明 IOTA 系列产品,但国内脉石英受限于晶格杂质,需进一步优化提纯工艺。我国高纯石英产业需加强优质矿源勘探、开发绿色提纯技术,以降低对进口高纯石英砂的依赖。本文设计的工艺流程提升了脉石英纯度,为制备高纯石英砂提供了方法。

该论文有图 25 幅, 表 28 个, 参考文献 54 篇。

关键词: 高纯石英砂; 脉石英; 提纯工艺; 半导体; 光伏

Abstract

High-purity quartz sand is a key material in the semiconductor and photovoltaic industries, and its purity affects the performance of high-end products. China's vein quartz reserves are abundant, but the quality of the ore deposit is low, and there are shortcomings in purification technology, which makes it difficult for domestic high-purity quartz sand to meet the needs of the semiconductor and photovoltaic industries. In view of this situation, this paper selects vein quartz from different origins at home and abroad as raw materials to design the preparation process of high-purity quartz sand.

In this paper, a comprehensive purification process of calcination-water quenching, grinding-screening, magnetic separation, flotation, pickling and chlorination is designed. Calcination-water quenching (1050°C) can effectively destroy the fluid inclusions and reduce the mechanical strength of quartz, magnetic separation uses magnetic differences to remove ferromagnetic impurities in quartz, under acidic conditions, flotation uses collectors and inhibitors to achieve efficient separation of quartz from feldspar and mica, pickling uses HCl:HF:HNO₃=3:1:1 mixed acid to significantly reduce metal impurities, chlorination removes alkali metals (Na, K, Li) through high-temperature chlorine reaction, and realizes the deep removal of impurities.

In this paper, the purification potential of vein quartz from Africa (LQBS-1), India (LQBS-2), Guizhou (LQBS-3) and Heilongjiang (LQBS-4 and LQBS-5) was systematically evaluated by combining mineralogical analysis, ICP-OES detection and microscopic analysis. The test results show that the total impurity content of African vein quartz (LQBS-1) is reduced to 8.75ppm after treatment, and the purity of SiO₂ reaches 99.999% (5N grade), which meets the standard of semiconductor and photovoltaic grade high-purity quartz sand (total impurities < 20ppm), of which the key impurities such as Al and Fe are reduced to 4.68ppm and 0.53ppm respectively, and can be used for semiconductor sand only need to further optimize the Ca content; (total impurities < 20ppm); The total impurity of Guizhou vein quartz is 40.50ppm, and the purity of SiO₂ reaches 4N6 grade (99.996%), which can be used as milky white lump material; Heilongjiang vein quartz still cannot meet the high purity standard after purification, and is only suitable for low-end fields such as industrial silicon.

Compared with the international high-end product standards, the samples from Africa and India are close to the Unimin IOTA series products, but the domestic vein quartz is limited by lattice impurities, and the purification process needs to be further

optimized. China's high-purity quartz industry needs to strengthen the exploration of high-quality mineral sources and develop green purification technology to reduce its dependence on imported high-purity quartz sand. The process designed in this paper improves the purity of vein quartz and provides a method for the preparation of high-purity quartz sand.

The paper has 25 figures, 28 tables and 54 references.

Keywords: high-purity quartz sand; vein quartz; purification process; semiconductor; photovoltaic

目 录

| 摘星 | 要 | I |
|------------|-------------------|----|
| 目表 | 录 | IV |
| | 绪论 | |
| | | |
| | 研究背景与意义 | |
| 1.2 | 国内外研究现状 | 3 |
| 1.3 | 主要内容、研究方法及拟要解决的问题 | 5 |
| 2 月 | 脉石英提纯难点及业内标准 | 7 |
| 2.1 | 石英晶体中的杂质种类及赋存状态 | 7 |
| 2.2 | 脉石英提纯难点 | 9 |
| 2.3 | 脉石英业内标准 | 10 |
| 3 月 | 脉石英提纯试验 | 14 |
| 3.1 | 煅烧-水淬 | 14 |
| 3.2 | 磨矿-筛分 | 15 |
| 3.3 | 磁选 | 16 |
| 3.4 | 浮选 | 16 |
| 3.5 | 酸洗 | 17 |
| 3.6 | 氯化 | 19 |
| 3.7 | 本章小结 | 20 |
| 4 E | 成品分析检测 | 21 |
| 4.1 | 手标本分析 | 21 |
| 4.2 | 镜下分析 | 22 |
| 4.3 | ICP-OES 分析 | 24 |
| 4.4 | 样品对比 | 33 |
| 4.5 | 本章小结 | 37 |
| 5 ½ | 结论与展望 | 39 |
| | 考文献 | |
| 翻记 | 译部分 | 43 |

Contents

| Abstract | I |
|--|----|
| Contents | IV |
| 1 Introduction | 1 |
| 1.1 Background and Significance of the Research | 1 |
| 1.2 Current Research Status at Home and Abroad | 3 |
| 1.3 Main Contents, Research Methods and Problems to be Solved | 5 |
| 2 Difficulties in Purification of Vein Quartz and Industry Standards | 7 |
| 2.1 Types and Occurrence States of Impurities in Quartz Crystals | 7 |
| 2.2 Difficulty in Purifying Vein Quartz | 9 |
| 2.3 Vein Quartz Industry Standard | 10 |
| 3 Vein Quartz Purification Test | 14 |
| 3.1 Calcination-Water Quenching | 14 |
| 3.2 Grinding-Screening | 15 |
| 3.3 Magnetic Selection. | 16 |
| 3.4 Flotation | 16 |
| 3.5 Acid Pickling | 17 |
| 3.6 Chlorination | 19 |
| 3.7 Chapter Summary | 20 |
| 4 Analysis and Testing of Finished Products | 21 |
| 4.1 Analysis of Hand Specimens | 21 |
| 4.2 Microscopic Analysis | 22 |
| 4.3 ICP-OES Analysis | 24 |
| 4.4 Sample Comparison | 33 |
| 4.5 Chapter Summary | 37 |
| 5 Conclusion and Outlook | 39 |
| References | 40 |
| Translation section | 43 |

1 绪论

1 Introduction

1.1 研究背景与意义(Background and Significance of the Research)

石英矿是一种以 SiO_2 形式存在的埋藏在地下(或分布于地表)的可供人类利用的天然矿物资源 $^{[1]}$ 。石英在自然界中存在多种同质多象变体,根据唐翠华等人的研究,斯石英中的 Si 呈现六次八面体配位,与金红石型结构相似;而 α -石英、 β -石英、 α -鳞石英、 α -方石英、 β -方石英、 β -所石英、柯石英等石英中,Si 均以四次四面体配位的形式存在,硅氧四面体的 4 个角顶与相邻四面体共用形成架状结构 $^{[2]}$ 。石英化学性质稳定,仅与 HF 发生反应生成四氟化硅气体,并易被浓磷酸缓慢腐蚀。同时,石英微溶于 KOH 溶液和 1,2-二羟基苯。

高纯石英是杂质元素总含量低于 50ppm 的石英^[3]。高纯石英凭借其优异的化学稳定性、低热膨胀系数、绝缘耐压特性以及突光电性能,成为石英玻璃及石英坩埚制备的核心原料。

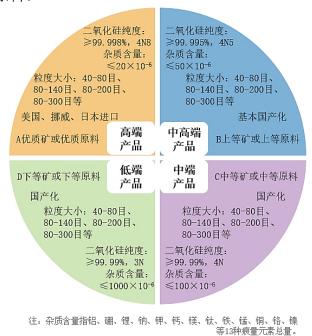


图 1-1 高纯石英产品等级

Figure 1-1 High-purity quartz product grade

高纯石英的高端产品被广泛应用于多个战略性领域,例如:在电子信息产业中支撑大规模集成电路、半导体和微电子器件制造;在新能源领域应用于太阳能电池与光伏组件生产;在光通信技术中被制作为光纤;除此之外,航空航天装备、国防军工、高功率激光装置、精密光学仪器以及高温照明设备等尖端科技领域也

有高纯石英的应用。美国尤尼明公司(Unimin)长期垄断着全球 4N8 级(纯度 ≥99.998%)及以上超高纯石英砂市场,旗下"IOTA"系列产品的纯度指标被视为石英砂产品品质的评判标准^[4]。

表 1-1 美国尤尼明公司 IOTA 石英系列产品及应用

| T 11 1 1 TOTA | | 1 . 1 | 1 1 | |
|------------------------|--------------|--------------|---------------|-------------|
| Table 1-1 IOTA | martz series | products and | Lapplications | of unimin |
| I WOID I I I O I I I C | mark berres | products are | appireamons | OI WIIIIIII |

| | | | 1 11 |
|----------|---------|--------------------|---------------------------|
| 编号 | 纯度 (%) | 成分 | 应用 |
| IOTA-STD | 99.998 | 纯 SiO2 | 可制成低膨胀系数的透明石英玻璃,应用于高温封 |
| | | | 接的汞灯、卤钨灯、低成本半导体石英制品。 |
| IOTA-4 | 99.999 | 纯 SiO ₂ | 可制成透明石英玻璃,应用于工艺管、硅片处理、 |
| | | | 石英块、提单晶硅用的半导体坩埚 |
| IOTA-6 | 99.9991 | 纯 SiO ₂ | 可制成石英玻璃,应用于低碱的石英制品、扩散管 |
| | | | 及固体内杂质不允许扩散的 CZ 坩埚 |
| IOTA-8 | 99.9992 | 纯 SiO2 | 可制成超高纯石英玻璃,应用于 12 英寸或更大尺寸 |
| | | | 硅片,大直径坩埚 |

随着光伏、半导体等战略性新兴产业的高速发展,我国对高纯石英材料的市场需求逐年增加,但国际垄断企业通过产能调控等手段控制市场价格,严重威胁我国高纯石英砂的稳定供给。特别是美国对光伏级超高纯石英材料实施出口管制,进一步加剧了原材料供应的风险。若我国在石英提纯技术领域无法实现突破,将在光伏、半导体、电子通信等关键领域形成发展瓶颈,影响国家战略性新兴产业的技术升级进程^[5]。



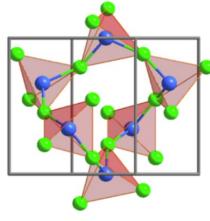


图 1-2 石英晶体及硅氧四面体结构

Figure 1-2 Quartz crystal and silicon-oxygen tetrahedral structure

高纯石英一般经过前期选矿和后期提纯加工而成,最初的原料为天然水晶^[6]。随着我国天然水晶资源因长期开采而趋于枯竭,脉石英已成为高纯石英的主要生产原料。脉石英因其成分单一,伴生矿物少,SiO₂含量较高,晶体颗粒粗,易分离等优点是制备高纯石英最有潜力的原料矿之一。脉石英矿床的成因是由于岩浆活动时分泌的 SiO₂ 热溶液沿岩石裂隙通道侵入,冷却时经气化作用和热液作用结晶而形成的地质体^[7]。该类型矿床主要呈脉状或透镜状,矿体厚度介于数米至

数十米之间,延伸长度可达数百米,但矿床规模普遍偏小^[8]。脉石英的类型根据成因主要可以分为两种,一种是岩浆热液型,另一种是变质热液型。岩浆热液型脉石英以花岗岩浆为主,该热液脉石英主要发育富 H₂O 贫 CO₂ 气体的流体包裹体,并可见含盐晶体的流体包裹体。变质热液型脉石英是岩浆运动下的矿物变质释放大量水形成变质热液溶液,热液流体一般为低盐度、富 CO₂ 流体,在构造应力的作用下,这些热液流体沿韧性剪切带运动,随着温压的变化,SiO₂ 发生过饱和析出,最终在有利部位发生结晶沉淀^[9]。

我国脉石英矿床具有显著的贫矿多、富矿少的特征,大型矿床极少。可开采的石英矿床中矿石平均品位不高,仅达 97.46%,满足高纯石英原料要求的优质矿产地仅占资源总量的 7.81%^[10]。脉石英中杂质元素赋存形态复杂,可分为脉石矿物、包裹体和晶格杂质元素,石英矿物晶格杂质和微小包裹体制约了脉石英型高纯石英的质量和品级^[11]。高品位石英矿中除了 Al 以外,还含有痕量碱金属元素(Li、Na、K)、碱土金属元素(Ca、Mg)以及 Fe、Ti 等过渡金属杂质,并且也存在 B、P 等非金属杂质元素^[12]。对于脉石英型高纯石英,通常需要利用物理-化学等方法提纯。

1.2 国内外研究现状 (Current Research Status at Home and Abroad)

1.2.1 国外研究现状

全球高纯石英矿床主要集中于北美、北欧及环太平洋三大区域,包含美国、巴西、加拿大、挪威、澳大利亚、俄罗斯和中国等国家。除中国外,共有矿床 14处,其中 7 处正在生产,7 处尚未生产^[13]。北美地区的美国斯普鲁斯派恩(Spruce Pine)矿床规模最大,探明储量超 1000 万吨;北欧板块的挪威德拉格(Drag)矿床储量最少,仅有 26.7 万吨。



图 1-3 全球高纯石英原料分布

Figure 1-3 Global distribution of high-purity quartz raw materials

截至到 2019 年底,全球已探明的高纯石英原料储量为 7300 万吨。巴西以 2111 万吨资源量居首,矿床类型主要为天然水晶; 美国以 1822 万吨排名第二,矿床类型主要为花岗伟晶岩型石英; 加拿大以 1000 万吨脉石英资源排名第三,矿石类型主要为脉石英^[14]。具备被制成 4N8 级(SiO₂≥99.998%)及以上高纯石英潜力的原料,主要来自于美国 Spruce Pine 地区花岗伟晶岩型石英矿床,以储量大、品质好最为著名^[15]。

1.2.2 国内研究现状

我国石英矿产资源丰富,主要有石英岩、石英砂岩、脉石英和天然石英砂这几种矿床类型,但存在资源分散、以中小型为主、品味低等特点^[16]。我国的脉石英型高纯石英原料矿床主要有以下几个产区:湖北蕲春,SiO₂含量为 99.35%;江苏东海,SiO₂含量为 99.19%;安徽旌德,SiO₂含量为 99.01%和太湖等地区,除此之外还有安徽凤阳、江苏新沂、新疆阿勒泰地区等地区^[17]。4N5 级(SiO₂含量>99.995%)及以上的高纯石英原料矿床在我国几乎没有分布,目前仍大量依靠进口。国内的脉石英矿床,以目前的技术条件,脉石英中能用作坩埚中内层原料的矿石不足 1%。

目前我国脉石英加工高纯石英的研究已有较大突破,刘理根^[18]等基于 SiO₂ 含量为 99.76%的脉石英,采取磁选-浮选-酸浸的方法加工出 4N 高纯石英。茆令文^[19]等在常规除杂工艺后,进一步采用高温氯化及煅烧脱气等手段,制备出了杂质总量为 25.29×10⁻⁶ 的高纯石英。汪灵等发明了二次煅烧水淬,多种酸混合的酸浸的优化工艺,获得了 SiO₂ 纯度 4N5 以上的高纯石英^[20],并通过无氯化焙烧等工艺制备了 SiO₂ 纯度 99.9985%的高纯石英。

我国在高纯石英加工技术领域取得阶段性突破,目前已实现 4N 级中端产品的规模化生产,但与国际相比仍存在显著差距。具体表现为: (1)产品纯度尚未突破 4N8 级高端技术门槛; (2)成品存在明显短板,缺乏覆盖不同纯度指标与粒度规格的系列化产品; (3)企业生产规模较小,无法实现大规模生产。

此次研究以国内外脉石英为研究对象,其中不同等级的脉石英原料包含印度脉石英、非洲脉石英、国内贵州脉石英和黑龙江脉石英,研究石英矿中杂质矿物种类和杂质元素赋存状态;根据不同品级石英矿的矿物学特征存在的明显差异,确定石英原矿性质、选矿提纯工艺方案和提纯后产品方向(坩埚中外层料、半导体级电子砂、石英坨料或拉管料);以Al、Fe、K、Na、Ca、Mg及总杂质金属元素的去除率为评价标准,制备符合 4N8 级标准的高端石英产品,降低我国高新技术产业在这一关键材料领域对国外的依赖。

1.3 主要内容、研究方法及拟要解决的问题 (Main Contents, Research Methods and Problems to be Solved)

1.3.1 研究内容

- (1)确定各类脉石英中石英矿物中杂质赋存状态、不同杂质危害及不同品级高纯砂产品的工艺要求;
- (2)设计高纯石英提纯的流程并进行实验:如物理(磁选、浮选)、化学(煅烧-水淬酸浸、氯化、高温掺杂)等除杂流程方法;
- (3)对比分析国内外高纯石英矿床脉石英矿石原料,以 A1、Fe、K、Na、Ca、Ma 及总杂质金属元素的去除率为指标选择合适的提纯工艺流程;
- (4)研究矿石组成及结构,分析石英矿物学和流体包裹体特征,建立高纯石英原矿评价"基因检测";
- (5) 对煅烧过程、酸浸过程、氯化工艺产生的石英砂进行元素、包裹体分析,探索各个工艺流程中石英中杂质元素的迁移和净化规律等。

1.3.2 研究方法与技术路线

- (1)对国内外不同产地脉石英进行矿物学分析,利用光学显微镜分析石英的形态、粒度、数量、以及石英所含流体包裹体的数量、分布、尺寸等特征;
- (2)利用 ICP-OES 分析脉石英原矿的杂质含量及各工艺阶段后的杂质含量,对比分析工艺去除效果;
- (3)分别采用热压酸浸、高温焙烧、氯化焙烧等加工提纯工艺,设计出一套能有效去除脉石英杂质的综合优化工艺。

此研究采用高纯石英提纯试验、理论分析等方法,对脉石英制备半导体及光 伏级高纯石英砂工艺流程进行研究设计,将所得结果进行归纳,为我国高纯石英 高端产品领域提供技术支持与应用探索。

技术路线图如下:

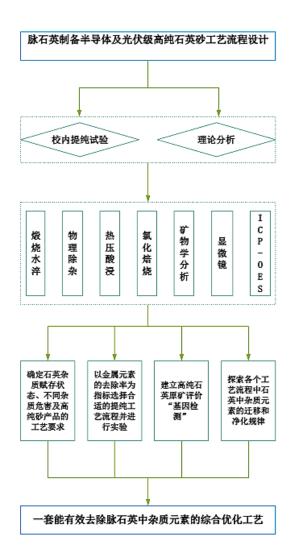


图 1-4 技术路线图 Figure 1-4 Technology roadmap

1.3.3 拟要解决的问题

- (1)对比分析国内外高纯石英矿床脉石英矿石原料,对脉石英进行精细的矿物学分析,找到4N8级以上脉石英型高纯石英矿源;
- (2)了解石英中杂质的赋存状态、熟练高纯石英提纯的流程并进行实验: 如物理(磁选、浮选)、化学(煅烧-水淬、酸浸、氯化)等除杂流程方法;
- (3)根据不同产地不同品级脉石英矿物学特性、杂质赋存状态和流体包裹体特征选择不同提纯方案,提纯后对标高纯石英砂不同档次产品;
- (4) 对同一种脉石英原料进行石英提纯并进行实验,检测提纯后高纯石英中杂质含量差异;设计出一套能有效去除脉石英中杂质元素的综合优化工艺;
- (5)了解对煅烧过程、酸浸过程、氯化过程元素除杂原理,探索各个工艺 流程中石英中杂质元素的迁移和净化机理等。

2 脉石英提纯难点及业内标准

2 Difficulties in Purification of Vein Quartz and Industry Standards

2.1 石英晶体中的杂质种类及赋存状态(Types and Occurrence States of Impurities in Quartz Crystals)

2.1.1 矿物包裹体

矿物包裹体是指形成于主体矿物内部并被其包裹的伴生矿物。矿物包裹体有两种形成因素:一是在变质过程中由于晶体界面的位移而产生的,二是在变质条件下石英重结晶时所形成的异种矿物。常见矿物包裹体包括白云母、黑云母、钾长石、斜长石、高岭石、赤铁矿、黄铁矿、方解石及金红石等,尺寸一般为 0.1 μ m~10mm^[21]。

2.1.2 气液包裹体

气液包裹体又称流体包裹体,是指以气体、液体、气液两相或气液固三相混合体形式存在于石英晶体中的杂质,主要成型于岩石冷却时石英的初始结晶阶段。除此之外,还可能成型于与地质运动相关的石英二次结晶过程中 $^{[22]}$ 。常见石英流体包裹体中主要含有 $^{[22]}$ 0、 $^{[23]}$ 0、 $^{[23]}$ 0、 $^{[23]}$ 0、 $^{[23]}$ 0、 $^{[23]}$ 0。表 $^{[23]}$ 2-1 气液包裹体杂质主要的存在形式

Table 2-1 The main forms of impurities in gas-liquid inclusions

| 名称 | 存在形式 | 物质名称 |
|-------|---------------|---|
| | | 气相: H ₂ O、H ₂ 、N ₂ 、CO、CO ₂ 、 CH ₄ 、 |
| 气液包裹体 | 均匀分布或沿解理面分布 | H ₂ S、SO ₂ 、HCL、CL ₂ 、F ₂ 液相: Na ⁺ 、Ca ²⁺ 、K ⁺ 、Mg ²⁺ 、F ⁻ Cl ⁻ 、 |
| 分子杂质 | 以分子形式散布于石英结构中 | SO_4^{2-} , H_2O , H_2 , CO , CO_2 , |

2.1.3 晶格杂质

天然石英矿物中的微量元素主要以两种机制赋存于石英晶格中: (1) 类质同象: 石英中的 Al^{3+} , Ti^{4+} , Ge^{4+} , Ga^{4+} , Fe^{3+} 和 P^{5+} 等离子通过置换石英 Si—O 四面体中的 Si^{4+} 进入石英晶格 (2) 电价补偿: Li^{+} , Na^{+} , K^{+} , H^{+} 等离子通过电价补偿进入石英晶格 $[2^{4}]$ 。在类质同象替代过程中, Ge^{4+} 和 Ti^{4+} 等四价离子因与 Si^{4+}

价态匹配可直接进行替代,而 Al^{3+} , Fe^{3+} , B^{3+} 等三价异价离子发生类质同象现象时必须遵守需遵循电荷补偿原则,即当 Al^{3+} 等三价离子置换 Si^{4+} 时,需由正一价碱金属离子(Li^+ 、 Na^+ , K^+)以及 H^+ 作为电荷补偿离子进入晶格间隙以维持电荷平衡。此外, Al^{3+} 和 P^{5+} 可通过类质同象联合置换的方式进入石英晶格中,即 Al^{3+} 和 P^{5+} 通过同时置换两个相邻 Si—O 四面体中的 $Si^{4+[25]}$ 。

表 2-2 晶格杂质主要发生状态及存在形式

Table 2-2 Main occurrence states and forms of lattice impurities

| 元素 | 发生状态 | 存在形式 |
|----|---------------|---|
| Al | 独立矿物和类质同象 | 粘土矿物; Al ³⁺ 取代 Si ⁴⁺ |
| Fe | 独立矿物、包裹体和类质同象 | 赤铁矿、黄铁矿等;微米包裹体;Fe ³⁺ 取代 Si ⁴⁺ |
| Ca | 独立矿物和包裹体 | 方解石和萤石;包裹体中的 Ca ²⁺ |
| Mg | 独立矿物和包裹体 | 白云石和云母;包裹体中的 Mg ²⁺ |
| K | 独立矿物、包裹体和类质同象 | 钾长石和粘土矿;包裹体中的 K+; 电荷补偿杂质 |
| Li | 包裹体和类质同象 | 包裹体中的 Li+; 电荷补偿杂质 |
| Na | 独立矿物、包裹体和类质同象 | 钾长石和云母;包裹体中的 Na+; 电荷补偿杂质 |
| Ti | 独立矿物和类质同象 | 金红石;Ti ⁴⁺ 取代Si ⁴⁺ |
| В | 类质同象 | B ³⁺ 取代 Si ⁴⁺ |
| Н | 包裹体和类质同象 | 包裹体中的水和有机物; 电荷补偿杂质 |

表 2-2 石英中杂质元素的赋存状态和存在形式(引自 Müller et al., 2012; Guo et al., 2019)

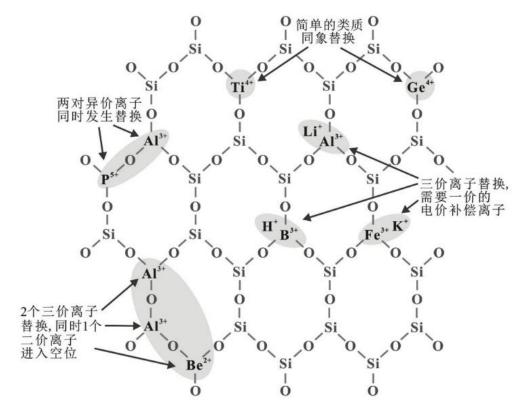


图 2-1 微量元素在石英晶格中存在形式的结构简图

Figure 2-1 Schematic diagram of the existence of trace elements in quartz lattice

2.1.4 高纯石英杂质危害

石英中的杂质元素会降低石英玻璃的各种性能,例如碱金属(Na⁺、K⁺、Li⁺) 离子会造成石英玻璃软化点降低,导致高温工况下产品尺寸失稳^[26];过渡金属元素会导致石英玻璃的绝缘性变差,高温下变色等情况;气液包裹体会导致石英玻璃出现气泡,一方面降低石英玻璃的透光性,另一方面使得石英玻璃出现结构性缺陷,劣化石英玻璃的机械强度^[27]和使用寿命等。

2.2 脉石英提纯难点(Difficulty in Purifying Vein Quartz)

2.2.1 流体包裹体

石英矿物中普遍存在的流体包裹体是制约高纯石英品质的关键因素。石英中流体包裹按内含物质状态可以分为: 纯气体包裹体、纯液体包裹体、气液混合包裹体和三相包裹体^[28]。由于气液包裹体的形成机制,在形成过程中会捕获过饱和流体,当环境温度降低时,过饱和溶液会结晶析出钾盐、硅酸盐等矿物,是高纯石英中杂质重要来源之一^[29]。

相比于杂质矿物,流体包裹体的特殊赋存形式使其难以被常规的物理及化学提纯技术去除,这导致流体包裹体成为影响最终石英产品质量的关键性因素之一^[30]。尽管目前国内外针对去除流体包裹体的方法研究已久,但在去除尺寸较小的流体包裹体方面仍未取得有效方法。因此在原料选择时,可以选择流体包裹体含量极少或无流体包裹体的石英。

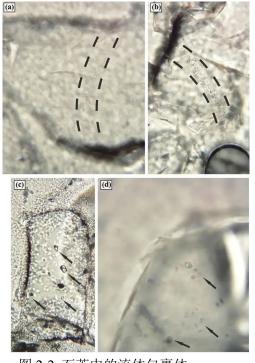


图 2-2 石英中的流体包裹体 Figure 2-2 Fluid inclusions in quartz

2.2.2 晶格杂质

石英晶体在结晶过程中会发生类质同象和电价补偿现象,部分元素(如 Al³+, Ti⁴+, Ge⁴+, Ga⁴+, Fe³+、P⁵+等)取代硅氧四面体中的 Si⁴+进入晶格形成结构性杂质,这些杂质含量虽然低,但去除难度极大。在这些杂质元素中, Al含量最高,并且当 Al 元素大量存在时, Li、K、Na 等杂质元素的含量也会相应的增加,晶格元素杂质已成为制约高纯石英最终质量的关键^[31]。基于现有提纯工艺的局限性,能够成为制备高纯石英原料的优质矿床应满足以下要求: 化学成分纯净、极少的晶格杂质和包裹体、伴生矿物容易去除。

2.3 脉石英业内标准(Vein Quartz Industry Standard)

2.3.1 光伏用高纯石英砂

根据 GB/T32649—2016 规定,光伏用石英砂二氧化硅含量应大于或等于99.99%,即 4N 级以上高纯石英砂,杂质元素总含量应小于或等于25µg/g,其中钾、锂、钠含量总和小于2.5µg/g,各杂质元素含量见下表:

表 2-3 光伏用高纯石英砂

Table 2-3 High-purity quartz sand for photovoltaic 杂质元素 允许含量(μg/g)

| 杂质元素 | 允许含量(μg/g) |
|-------|------------|
| 铝(Al) | <20 |
| 钙(Ca) | <1 |
| 铁(Fe) | < 0.5 |
| 钠(Na) | <1 |
| 钾(K) | <1 |
| 锂(Li) | <1 |
| 镁(Mg) | < 0.5 |
| 铬(Cr) | < 0.1 |
| 镍(Ni) | < 0.1 |
| 硼(B) | < 0.1 |
| 锰(Mn) | < 0.2 |
| 铜(Cu) | < 0.1 |
| 钛(Ti) | <1.5 |

2.3.2 石英坩埚高纯内层砂

我国不同行业石英坩埚用高纯石英砂杂质元素要求如下: 表 2-4 不同行业石英坩埚用高纯石英砂

Table 2-4 High-purity quartz sand for quartz crucibles in different industries

| 元素 | 半导体 | 半导体单晶硅 | | 光伏单晶硅 | | 电子专用材料单晶硅 | |
|----|------|--------|-------|-------|------|-----------|--|
| 儿系 | 内层 | 外层 | 内层 | 外层 | 内层 | 外层 | |
| Al | 9.00 | 13.50 | 13.50 | 18.00 | 7.70 | 16.00 | |
| Ca | 0.80 | 1.20 | 1.20 | 1.20 | 0.80 | 1.20 | |
| | | | 10 | | | | |

| Mg | 0.10 | 0.10 | 0.10 | 0.10 | 0.05 | 0.10 |
|--------------------|---------|---------|--------|----------|---------|--------|
| Ba | 0.05 | 0.10 | 0.10 | 0.10 | - | 0.10 |
| Cr | 0.05 | 0.10 | 0.10 | 0.10 | - | 0.10 |
| Cu | 0.10 | 0.10 | 0.10 | 0.10 | - | 0.10 |
| Fe | 0.05 | 0.05 | 0.05 | 0.05 | 0.20 | 0.05 |
| Ni | 0.05 | 0.10 | 0.10 | 0.10 | - | 0.10 |
| Mn | 0.10 | 0.10 | 0.10 | 0.10 | - | 0.10 |
| Li | 0.50 | 0.80 | 0.80 | 1.00 | 0.10 | 1.00 |
| Na | 0.50 | 0.80 | 0.80 | 1.00 | 0.20 | 1.00 |
| K | 0.50 | 0.80 | 0.80 | 1.00 | 0.10 | 1.00 |
| Zr | 0.50 | 0.50 | 0.50 | 0.50 | - | 0.50 |
| Ti | 1.50 | 2.00 | 2.00 | 2.00 | 1.40 | 2.00 |
| Ge | 1.50 | 1.50 | 2.00 | 2.00 | 0.70 | 0.70 |
| P | 0.05 | 0.05 | 0.10 | 0.10 | - | 0.10 |
| В | 0.05 | 0.05 | 0.10 | 0.10 | < 0.10 | < 0.10 |
| SUM | 15.9 | 22.4 | 22.9 | 28.0 | 11.4 | 20.0 |
| SiO ₂ % | 99.9984 | 99.9978 | 99.997 | 999.9979 | 99.9989 | 99.998 |

2.3.3 电子产品用高纯石英砂

根据中华人民共和国电子行业标准 SJ/T 3228.1《电子产品用高纯石英砂》规定,半导体砂杂质元素含量要求如下:

表 2-5 电子产品用高纯石英砂

Table 2-5 High-purity quartz sand for electronic products

| -T II | | 指标 | _ |
|-------|----------|----------|----------|
| 项目 | 一级 | 二级 | 三级 |
| 二氧化硅 | ≥99.991% | ≥99.990% | ≥99.998% |
| 杂质元素 | | 允许含量(μg/ | /g) |
| 铝(Al) | ≤8.00 | ≤8.00 | ≤16.00 |
| 钙(Ca) | ≤0.50 | ≤0.60 | ≤0.80 |
| 铁(Fe) | ≤0.15 | ≤0.30 | ≤0.30 |
| 钠(Na) | ≤0.10 | ≤0.60 | ≤0.90 |
| 钾(K) | ≤0.10 | ≤0.50 | ≤0.60 |
| 锂(Li) | ≤0.30 | ≤0.50 | ≤0.90 |
| 镁(Mg) | ≤0.05 | ≤0.10 | ≤0.20 |
| 铬(Cr) | ≤0.05 | ≤0.05 | ≤0.05 |
| 镍(Ni) | ≤0.05 | ≤0.05 | ≤0.05 |
| 硼(B) | ≤0.04 | ≤0.06 | ≤0.08 |
| 锰(Mn) | ≤0.05 | ≤0.05 | ≤0.05 |
| 铜(Cu) | ≤0.02 | ≤0.03 | ≤0.05 |

2.3.4 美国尤尼明 IOTA 产品质量指标

美国尤尼明公司(Unimin)在高纯度石英砂的研发、生产和供应等方面被视为高纯石英砂行业标准,其原料来自美国斯普鲁斯派恩(Spruce Pine)矿床,石英矿天然杂质极少。IOTA系列高纯度石英砂以其超高纯度、极低杂质含量和稳定品质成为被全球半导体和光伏行业公认的顶级原材料,IOTA系列具体标准见下表:

表 2-6 美国尤尼明 IOTA 产品质量指标 Table 2-6 Product Quality Index of IOTA

| 化学元素 | IOTA4 | IOTA 6 | IOTA 6-SV | IOTA 8 | IOTA STD-SV | IOTA CG | IOTA STD |
|------|-------|--------|-----------|---------|-------------|---------|----------|
| Al | 8 | 8 | 8 | 8 | 14 | 14 | 14 |
| В | | | < 0.05 | | | < 0.10 | |
| Ca | 0.7 | 0.7 | 0.5 | 0.4 | 0.3 | 0.6 | 0.6 |
| Cr | 0.007 | 0.003 | 0.002 | 0.001 | 0.004 | 0.007 | 0.006 |
| Cu | 0.004 | 0.001 | 0.001 | < 0.001 | 0.003 | 0.019 | 0.028 |
| Fe | 0.3 | 0.2 | 0.1 | < 0.05 | 0.1 | 0.3 | 0.3 |
| K | 0.4 | 0.1 | < 0.1 | < 0.05 | 0.5 | 0.5 | 0.5 |
| Li | 0.2 | 0.2 | 0.2 | < 0.05 | 0.5 | 0.5 | 0.5 |
| Mg | 0.07 | 0.07 | 0.02 | 0.01 | 0.01 | 0.04 | 0.04 |
| Mn | 0.013 | 0.008 | 0.004 | 0.001 | 0.007 | 0.029 | 0.039 |
| Na | 1.0 | < 0.1 | | < 0.05 | | 1.00 | 1.00 |
| Ni | 0.002 | 0.002 | 0.001 | < 0.001 | 0.001 | 0.001 | 0.001 |
| P | 0.1 | 0.1 | < 0.0 |)5 | 0.1 | 0.1 | 0.1 |
| Ti | 1.4 | 1.4 | 1.3 | 1.3 | 1.1 | 1.2 | 1.2 |

2.3.5 挪威 TQC 公司产品质量指标

挪威石英公司(TQC)是全球高纯度石英砂领域的顶尖企业之一,其原料主要来自于挪威西部的德拉格(Drag),该地区石英矿的天然纯度高且杂质元素分布均匀,少部分原料来自美国斯普鲁斯派恩(Spruce Pine)矿床。TQC 的 NW 系列是其高纯度石英砂产品线中的重要组成,主要服务于光伏、半导体及特种玻璃行业,具体标准见下表:

表 2-7 挪威 TQC 公司产品质量指标 Table 2-7 Product Quality Index of Norway TQC

| | . , | |
|------|--------|--------|
| 化学元素 | NW-4A | NW-4X |
| В | * | * |
| K | 1.17 | 0.23 |
| Na | 1.03 | 0.10 |
| Li | 0.26 | 0.35 |
| Ca | 1.27 | 1.88 |
| Al | 13.85 | 12.37 |
| Mg | 0.15 | 0.13 |
| Cr | < 0.05 | < 0.05 |
| Cu | < 0.05 | < 0.05 |
| | | |

2 脉石英提纯难点及业内标准

| Fe | 0.52 | 0.21 |
|----|--------|--------|
| Mn | * | * |
| Ni | < 0.05 | < 0.05 |
| 总量 | 18.40 | 15.42 |

3 脉石英提纯试验

3 Vein Quartz Purification Test

本次试验以脉石英为原料进行提纯工艺的研究,采用印度脉石英、非洲脉石 英、贵州脉石英和黑龙江脉石英,样品编号如下:

表 3-1 样品编号及产地

| | 样品编号 | 产地 |
|---|--------|--------|
| 1 | LQBS-1 | 非洲脉石英 |
| 2 | LQBS-2 | 印度脉石英 |
| 3 | LQBS-3 | 贵州脉石英 |
| 4 | LQBS-4 | 黑龙江脉石英 |
| 5 | LQBS-5 | 黑龙江脉石英 |

Table 3-1 Sample number and place of origin

3.1 煅烧-水淬 (Calcination-Water quenching)

石英矿在煅烧-水淬过程中,温度骤变会引起矿物内部结构的剧烈变化。当 石英矿经历高温煅烧后放入水中时,其内部会因为急速的热胀冷缩而发生剧烈形 变,由于石英矿不同位置的收缩速度不一致,导致石英内部应力不均匀分布,在 薄弱区域形成微裂纹或直接碎裂。这种结构性破坏显著降低了石英的整体机械强 度,便于后续制砂。

石英中的流体包裹体通常包含水、二氧化碳或盐类溶液等,在高温下,流体 包裹体内部因受热而急剧膨胀,导致内部压力骤增,超过石英的机械强度时,气 液包裹体附近产生微裂纹或破裂[32]。对于矿物包裹体而言,由于杂质与石英热膨 胀系数的差异, 升温时两者交界处会形成应力集中区域。 当温度导致的形变差异 足够大时, 交界处产生裂痕。 裂痕的产生使得原本紧密嵌布在石英中的矿物包裹 体暴露出来,为后续酸洗、浮选等提纯工序提供了有利条件。

综上所述, 煅烧-水淬工艺主要有三个作用:

- (1) 使石英晶体产生结构性转变,降低石英的机械强度;
- (2) 有效去除石英中的流体包裹体;
- (3) 为后续去除石英中的矿物包裹体提供有利条件[33]。

煅烧开始前, 先对石英矿石进行擦洗脱泥, 去除石英表面的杂质, 擦洗干净 后进行煅烧。设置煅烧温度 1050℃, 煅烧时长 120 分钟。煅烧完成后, 将样品倒 入水中进行水淬。





图 3-1 水淬时的样品 Figure 3-1 Sample during water quenching

待样品完全冷却,将样品取出放入烘干箱内烘干,得到干燥的样品。



图 3-2 烘干后的样品 Figure 3-2 Sample after drying

3.2 磨矿-筛分(Grinding-Screening)

进行磨矿-筛分工作,得到粒径在 60-150 目的砂,不同磨矿时间对目标粒级的石英产率影响较大,适当的磨矿时间可以增加目标粒级的产率,而过长的磨矿时间将导致过磨,使得目标粒级产率降低^[34]。

研磨涉及对两种不同类型石英原料的研磨处理:第一类为经过煅烧-水淬工艺处理的石英,其研磨目的在于获得适宜粒径的砂以便于后续提纯工序;第二类为未经煅烧-水淬的石英原矿,研磨目的在于制备原矿砂样品。研磨两种不同类型的石英原料旨在通过对比分析原始矿物与预处理矿物在提纯过程中的差异性表现,从而科学评估工艺流程对石英的提纯效果。





图 3-3 玛瑙研钵及筛网 Figure 3-3 Agate mortar and sieve

3.3 磁选 (Magnetic Selection)

矿物可按磁性分为: 抗磁性矿物、顺磁性矿物和铁磁性矿物,表 3-2 为常见矿物磁性分类。

表 3-2 常见矿物磁性分类

Table 3-2 Magnetic classification of common minerals

| 常见矿物磁性分类 | | | |
|----------|--------------------------|--|--|
| 铁磁性矿物 | 磁铁矿、黄铁矿等 | | |
| 顺磁性矿物 | 黑云母、独居石、钛铁矿、金红石、铬铁矿、赤铁矿等 | | |
| 抗磁性矿物 | 石英、斜长石、方解石、锆石、磷灰石等 | | |

磁选是常用的物理分离方法,利用不同矿物的磁导率差异,通过外加磁场作用将不同矿物分离。由于含铁杂质易被磁化,而石英不能被磁化^[35],利用此性质可将赤铁矿、褐铁矿、黑云母及磁铁矿等杂质有效去除,但磁选对于弱磁性或者非磁性矿物的除杂效果不好,要进一步提纯石英粉,还需进行浮选等后续操作^[36]。

3.4 浮选(Flotation)

浮选是利用矿物表面疏水性差异,实现长石、云母等硅酸盐矿物与石英分离的选矿方法^[37]。影响浮选的因素较多,除矿浆浓度、给料粒度、浮选温度和调浆时间外,最重要的是浮选介质的 PH 值、药剂种类和用量^[38]。浮选需要浮选药剂、搅拌装置和充气装置,浮选药剂包括捕收剂、PH 调节剂、抑制剂、起泡剂和活化剂等。使用浮选药剂的目的是为了扩大目标矿物和其他矿物的疏水性差异,从而使不同的矿物在浮选过程中表现出不同的上浮或下沉现象,便于得到目标矿物。抑制剂的原理是通过化学吸附或化学反应,使目标矿物亲水,难以上浮。捕收剂

的原理是其选择性吸附在目标矿物表面,使目标矿物表面疏水,能够随着气泡上浮至矿浆表面,实现分离。常用捕收剂有石油磺酸钠、油酸钠、部分燃油和各种胺类捕收剂^[39]。按照目标矿物在浮选过程中的上浮或下沉现象,浮选可分为正浮选和反浮选^[40]。目标矿物上浮随气泡浮出浮选槽为正浮选,杂质上浮随气泡浮出浮选槽,目标矿物沉在浮选槽底部为反浮选。

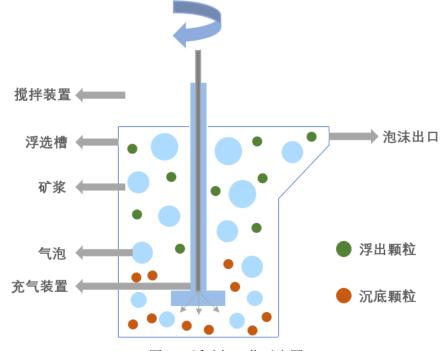


图 3-4 浮选机工作示意图

Figure 3-4 Schematic diagram of the flotation machine

浮选的目的主要是分离石英砂和杂质矿物,主要涉及石英和长石的分离、石英和云母的分离等^[41]。石英、长石和云母的浮选分离主要依赖特定化学环境下的表面性质差异和药剂选择性作用。在强酸性环境中加入氢氟酸作为活化剂,氢氟酸会轻微腐蚀长石和云母表面,暴露出铝相关的活性位点(如 Al³+),石英的硅氧结构相对稳定,吸附能力较弱。此时加入捕收剂,带正电的胺类分子会优先吸附在长石和云母的铝活性位点上,使其表面疏水,而石英因缺乏这类活性位点且被抑制剂包裹,仍保持亲水性^[42]。在充气搅拌过程中,云母由于层状结构的解理面天然疏水性较强,再加上捕收剂的强化作用,会优先附着气泡上浮。剩余矿浆中的长石在持续捕收剂作用下逐渐疏水,通过二次浮选被分离。最后残留的石英因亲水性强而沉降在矿浆底部。

本次试验使用 HF 作为 PH 调节剂,抑制剂 A 和捕收剂 B 进行浮选。

3.5 酸洗(Acid pickling)

酸洗是一种常用的提纯手段。磁选和浮选等方法只能去除石英砂表面附着的杂质矿物,对于石英内部的杂质则需要进行酸洗处理。酸洗是利用石英仅溶于氢

氟酸的特性,去除石英颗粒内金属杂质及共伴生杂质矿物的有效方法。酸的种类、浓度和酸浸温度、时间等都会影响除杂效果^[43]。常用酸的种类包括硫酸、盐酸和硝酸等。在实际酸洗提纯过程中,为了实现更好的酸洗效果并彻底去除杂质矿物,一般用强酸加上氢氟酸形成的混合酸制备高纯石英^[44]。对石英砂提纯质量影响程度从大到小依次为:酸浸时间>酸浸温度>酸液质量分数>液固^[45]。在酸洗时添加少量氢氟酸,可以破坏石英颗粒的表面结构,使得石英内部的杂质暴露,增加杂质与酸液的接触面积,可以极大地提高酸浸的提纯效果。酸洗根据不同的压力条件划分为常压酸洗与热压酸洗两大类。常压酸洗是指在恒定压力下进行的酸洗,而热压酸洗则涉及更高的温度和压力环境,以此来加速反应速率并提高提纯效率。

研究表明,只有在稀酸与 HF 同时存在的情况下,才可以有效除去 Fe、Al、Mg、Ca 等金属杂质,但需要控制 HF 的量,否则 HF 会侵蚀石英颗粒^[46],一般 HF 的量不超过总酸量的 10%。而不同种类的酸的提纯加工质量不同,其中 HCl 与 HF 混酸的加工效果最好^[47]。

据此,本文以HCl:HF:HNO₃=3:1:1 配置成的混合酸为浸出液,反应温度90℃, 反应时间24h。

本次试验用酸如下表:

表 3-3 试验用酸 Table 3-3 Acid for test

| 酸 | 含量(%) |
|-----|-----------|
| 盐酸 | 36.0~38.0 |
| 硝酸 | 65.0~68.0 |
| 氢氟酸 | ≥40.0 |

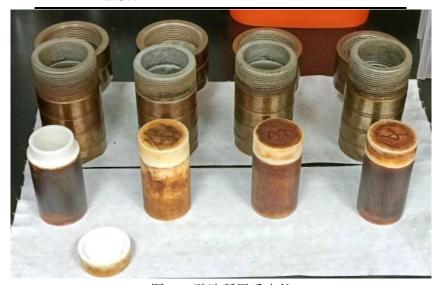


图 3-5 酸洗所用反应釜

Figure 3-5 Reactor used for pickling

3.6 氯化(Chlorination)

在现有提纯工艺中,石英中的绝大部分杂质和气液包裹体都能够被有效去除,但晶格杂质的去除仍然存在明显问题^[48]。过量增加酸的用量或延长处理时间会导致石英的整体溶蚀,造成产率的下降。因此,要获得更高品质的高纯石英,需要在现有工艺基础上引入深度提纯工艺。

氯化焙烧是一种深度提纯工艺,其原理通过控制温度、气氛等,利用氯化剂将石英矿中的部分杂质转变为氯化物,利用石英颗粒矿物表面与内部在高浓氯气作用下产生的化学位梯度,促使矿物内部的包裹体扩散出去^[49]。石英颗粒表层的碱金属元素(Na、K、Li)和残余的包裹体等杂质在高温下与氯气反应生成气态氯化物,相较于其他金属离子,Al 和 B 的反应活性较低,高温气流将这些杂质元素的氯化物带走^[50]。内部杂质转变为气相或者凝聚相氯化物,从而脱离原有石英体系得到去除,实现深度提纯的目的^[51]。

现阶段的氯化焙烧技术主要包含三种:中温氯化焙烧、高温氯化焙烧以及氯化一离析,其具体区别见下表:

表 3-4 不同氯化焙烧的区别
Table 3-4 Differences between different chlorinated roasts

| 技术 | 流程 | 效果 |
|------------|--------------|--------------|
| 中温氯化焙烧 | 生成固体氯化物,后续进行 | 工业上应用较早,工艺较为 |
| (氯化锻烧-浸出法) | 酸洗去除。 | 成熟,但是去除效率较低。 |
| 高温氯化焙烧 | 生成气体金属氯化物逸出。 | 利于金属回收。 |
| (高温氯化挥发法) | 土风气冲壶周泉化初返山。 | 71 1 並周凹収。 |
| 氯化一离析法 | 生成金属单质,后续物理选 | |
| | 矿去除。 | |
| | | |

氯化剂分为固体氯化剂和气体氯化剂,固体氯化剂包括 NaCl、KCL、CaCl₂和 NH₄Cl,气体氯化剂包括 HCl 和 Cl₂。以 Cl₂为例,Cl₂在高温下具有强氧化性能与 Al₂O₃、Fe₂O₃等金属氧化物发生氯化反应,部分反应方程式如下:

| $Al_2O_3+Cl_2\uparrow \longrightarrow AlCl_3\uparrow +O_2\uparrow$ | (3-1) |
|--|-------|
| $FeO+Cl_2\uparrow \rightarrow FeCl_2\uparrow +O_2\uparrow$ | (3-2) |
| $FeCL_2+Cl_2\uparrow \rightarrow FeCl_3\uparrow$ | (3-3) |
| $TiO_2+Cl_2\uparrow \longrightarrow TiCl_4\uparrow+O_2\uparrow$ | (3-4) |
| $CuO+Cl_2\uparrow \rightarrow CuCl_2\uparrow +O_2\uparrow$ | (3-5) |
| $MnO_2+Cl_2\uparrow \rightarrow MnCl_4\uparrow +O_2\uparrow$ | (3-6) |
| $CaO+Cl_2\uparrow \rightarrow CaCl_2\uparrow +O_2\uparrow$ | (3-7) |
| $MgO+Cl_2\uparrow \rightarrow MgCl_2\uparrow +O_2\uparrow$ | (3-8) |

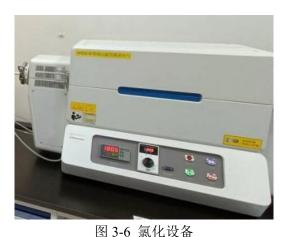


Figure 3-6 Chlorination equipment

3.7 本章小结(Chapter Summary)

本章主要进行了脉石英提纯工艺试验,通过煅烧-水淬、磨矿-筛分、磁选、 浮选、酸洗及氯化等工序,去除脉石英杂质元素。

- (1)煅烧-水淬:通过 1050℃高温煅烧及水淬处理,促使石英产生微裂纹,有效破坏流体包裹体,为后续物理-化学提纯创造有利条件。
 - (2)磨矿-筛分: 研磨筛分, 获得 60-150 目砂样, 避免过磨导致产率降低。
 - (3)磁选:利用磁性差异去除磁铁矿、黄铁矿等含铁杂质。
 - (4)浮选:在酸性条件下利用捕收剂和抑制剂,分离长石和云母。
 - (5)酸洗: 采用 HC1-HF-HNO3 混合酸, 去除石英中的金属杂质。
 - (6)氯化:通过高温氯气反应去除碱金属(Na、K、Li)。

本章为脉石英制备高纯石英砂的工艺流程设计提供了试验依据。

4 成品分析检测

4 Analysis and Testing of Finished Products

4.1 手标本分析(Analysis of Hand Specimens)

分析手标本是为了简单快速获取石英矿的宏观特征信息,为后续深入研究提供初步判断和方向。通过直接观察样品的颜色、结构、构造、硬度等物理性质,初步筛选出符合实验目标的样品,减少不必要的成本。手标本的宏观观察结果能与微观薄片及元素检测数据相互印证,综合分析工艺效果。

表 4-1 各样品手标本分析

描号照片宏观分析LQBS-1整体呈无色-浅烟灰色,块状结构,贝壳状断口、油脂光泽。LQBS-2整体呈无色-浅烟灰色,砂糖状结构,石英颗粒较小。

LQBS-3



整体呈现瓷白色,石英隐 晶质块状结构、局部可见 少量水晶晶体。



整体呈茶色,块状结构, 含较多裂隙、部分石英晶 型较好、无色透明。



LQBS-4



整体呈茶色,块状结构、 裂隙中铁质较多、部分石 英晶型较好、无色透明。

基于手标本分析,LQBS-1与LQBS-2整体透亮,LQBS-3整体瓷白色,局部见少量水晶,LQBS-4和LQBS-5呈茶色,铁质较多。

4.2 镜下分析 (Microscopic Analysis)

4.2.1 探针片

通过显微镜镜下观察脉石英探针片,分析样品原矿中杂质矿物的种类、气液包裹体含量及分布、嵌布特征及石英晶体缺陷等,预测样品提纯难度,评估原矿的经济性价值,减少无效操作,降低成本且提高纯度^[52]。

(1)LQBS-1: 镜下见少量包裹体,属于高品位脉石英矿床。

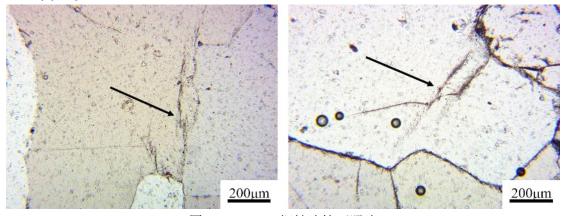


图 4-1 LQBS-1 探针片镜下照片

Figure 4-1 Photograph of the LQBS-1 probe piece

(2) LQBS-2: 镜下偶见气液包裹体,属于高品位脉石英矿床。

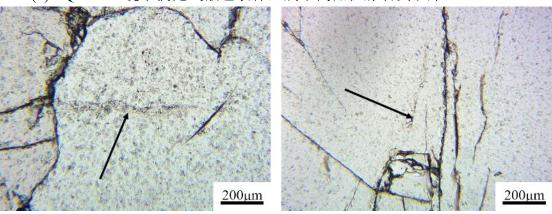


图 4-2 LQBS-2 探针片镜下照片 Figure 4-2 Photograph of the LQBS-2probe piece

(3) LQBS-3: 镜下石英表面浑浊,极多微小包裹体。

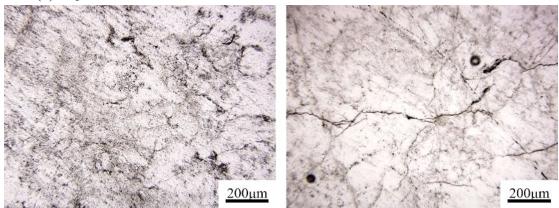


图 4-3 LQBS-3 探针片镜下照片 Figure 4-3 Photograph of the LQBS-3probe piece

(4) LQBS-4: 镜下石英污浊,极多气液包裹体。

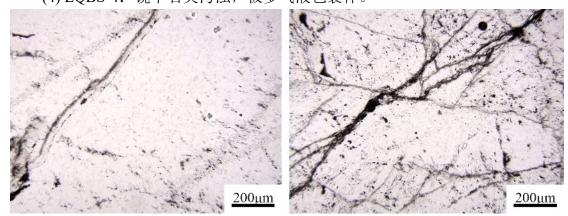


图 4-4 LQBS-4 探针片镜下照片 Figure 4-4 Photograph of the LQBS-4probe piece

(5) LQBS-5: 镜下石英污浊,极多气液包裹体。

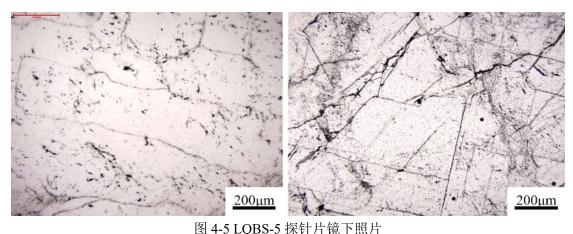


图 4-3 LQBS-3 旅行月银下照月

Figure 4-5 Photograph of the LQBS-5probe piece

4.2.2 各阶段砂

通过显微镜镜下观察各阶段的砂,对石英砂的浮选过程、酸浸过程、氯化过程进行微观分析,探索各个工艺流程对石英内部包裹体的去除效果。

表 4-2 各阶段砂镜下分析

Table 4-2 Analysis under sand microscope at each stage

 浮选后的砂
 酸洗后的砂

 氯化后的砂

浮选砂在镜下可见大量气液包裹体,酸洗砂中气液包裹体数量明显降低,但仍存在部分残余,氯化砂中气液包裹体数量极少,仅偶见残余。镜下各阶段砂进行分析表明,原矿样品经浮选-酸浸-氯化工艺处理后,石英内部包裹体及云母数量均大幅减少,最终产物的纯净度较原料样品获得显著提升。

4.3 ICP-OES 分析(ICP-OES Analysis)

4.3.1 原理

电感耦合等离子体发射光谱法(ICP-OES)的原理是利用物质被激发后发射的特征光谱特性进行元素分析^[53]。样品溶液通过雾化系统转为气溶胶颗粒,由氩气带入高温电感耦合等离子体中。高温能够将样品分解、原子化、离子化,并进一步使原子外层电子被激发到高能态。当这些激发态的电子从高能级跃迁回低能级时,会释放出特定波长的光辐射,形成特征谱线。特征光谱按波长分离后,由光电倍增管或电荷耦合器件(CCD)测量其强度。光谱强度与样品中元素的浓度在

一定范围内呈正比关系,通过与已知浓度的标准样品对比,即可实现元素的定性和定量分析^[54]。

电感耦合等离子体发射光谱法(ICP-OES)具有以下特点:

- (1)多元素同时检测。ICP-OES 最突出的优势之一。除氩以外的自然界存在的元素,都能够用 ICP-OES 检测,可以在一次进样中同时测定数十种元素的含量,大幅提升分析效率。
- (2)低检测限和线性分析范围宽。元素周期表内绝大多数元素在水溶液中的 检出限达 0.1-100ng/ml。ICP-OES 的工作曲线通常覆盖 5~6 个数量级的浓度范 围,这意味着在同一检测中,ICP-OES 既能分析痕量元素,也能直接测定高浓度 组分,减少样品稀释或浓缩的步骤,降低操作误差。
- (3)抗干扰能力强和样品适用性广。ICP-OES 具有较高的蒸发、原子化和激发能力,干扰水平比较低。可分析液体、固体和气体样品。将样品制成溶液再进行分析,可以消除样品宏观的结构干扰和非均匀性。

4.3.2 ICP-OES 结果分析

通过 ICP-OES 技术,对样品在原矿、浮选、酸洗和氯化阶段的元素含量进行检测,追踪关键杂质元素在不同工艺中的浓度变化,结合原矿杂质含量数据系统对比浮选、酸洗、氯化这三个步骤对石英杂质元素的去除效果。

(1) LQBS-1

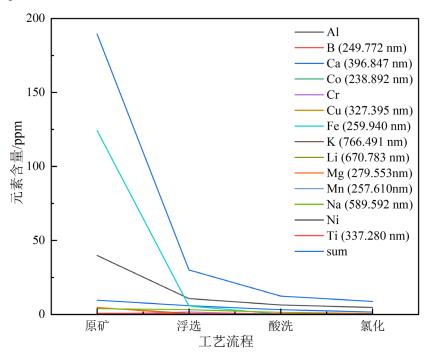


图 4-6 LOBS-1 样品各工艺阶段元素变化

Figure 4-6 Elemental changes in each process stage of the LQBS-1 sample

如图所示,LQBS-1 样品经浮选-酸洗-氯化工艺处理后,各杂质元素含量明显降低,其中,总杂质元素含量浓度<50ppm,Al<30ppm,Ti<10ppm,符合定义为适用于高科技应用的"高纯度"石英(HPQ)的标准,SiO2纯度99.9991%(5N级)。

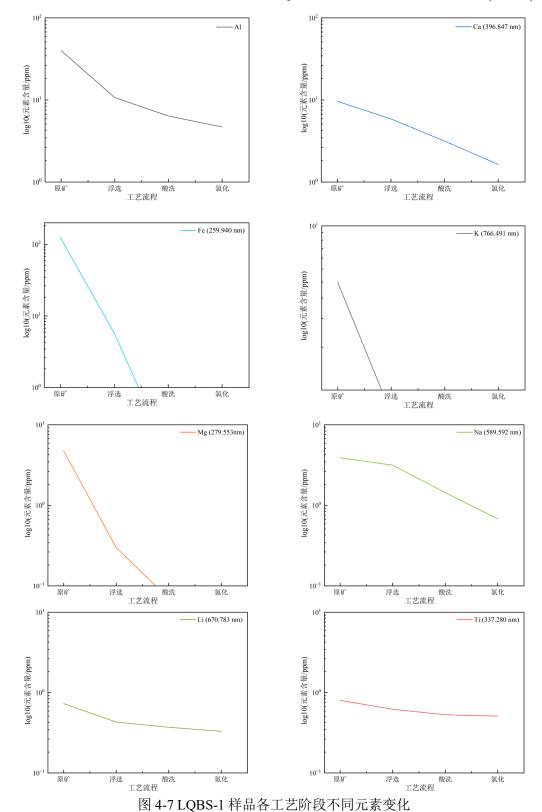


Figure 4-7 Changes of different elements in each process stage of LQBS-1 sample

| 表 4-3 LQBS-1 样品 ICP-OES 元素检测结果 | |
|--|---|
| Table 4-3 ICP-OES element test results of LQBS-1 sampl | e |

| 样品编号 | Al | В | Ca | Co | Cr | Cu | Fe | K |
|-----------|----------|----------|----------|----------|------|----------|----------|----------|
| | | (249.772 | (396.847 | (238.892 | | (327.395 | (259.940 | (766.491 |
| | | nm) | nm) | nm) | | nm) | nm) | nm) |
| LQBS-1 原矿 | 39.86 | 0.2 | 9.63 | 0.02 | 0.15 | 0.17 | 124.28 | 4.53 |
| LQBS-1 浮选 | 10.68 | 0.05 | 5.88 | 0.02 | 1.67 | 0.06 | 5.73 | 0.72 |
| LQBS-1 酸测 | 6.37 | 0.03 | 3.15 | 0.01 | 0.02 | 0.02 | 0.12 | 0.22 |
| LQBS-1 氯化 | 4.68 | 0.03 | 1.64 | 0.01 | 0.09 | 0.02 | 0.53 | 0.09 |
| 样品编号 | Li | Mg | Mn | Na | Ni | Ti | sum | |
| | (670.783 | (279.553 | (257.610 | (589.592 | | (337.280 | | |
| | nm) | nm) | nm) | nm) | | nm) | | |
| LQBS-1 原矿 | 0.73 | 4.75 | 0.31 | 3.89 | 0.18 | 0.8 | 189.5 | |
| LQBS-1 浮选 | 0.43 | 0.3 | 0.06 | 3.15 | 0.68 | 0.62 | 30.05 | |
| LQBS-1 酸测 | 0.37 | 0.07 | 0.01 | 1.44 | 0.01 | 0.53 | 12.37 | |
| LQBS-1 氯化 | 0.33 | 0.08 | 0.01 | 0.68 | 0.05 | 0.51 | 8.75 | |

如图 4-6、4-7 及表 4-3 所示,LQBS-1 原矿检测结果显示:初始 Al 含量为 39.86ppm,Fe 为 124.28ppm,是主要杂质元素。经浮选处理后,Al 含量从 39.86ppm 降至 10.68ppm,去除率为 73%;Fe 从 124ppm 降至 5.73ppm,去除率为 95%。 这证明磁选和浮选可以有效去除石英中的长石和磁铁矿。

经酸洗处理后,Fe 和 Al 进一步被去除。Al 从 10.68ppm 降至 6.37ppm,去除率 40.3%; Fe 从 5.73ppm 降至 0.12ppm,去除率 97.9%; Na 从 3.15ppm 降至 1.44ppm,去除率达 54.3%; Cr 从 1.67ppm 降至 0.02ppm,去除率达 98.8%。这表明酸洗不仅能去除石英表面的金属杂质,还可渗透至石英微裂隙中去除石英内部杂质。经氯化处理后,Na 和 K 含量下降,这是由于高温下氯气与碱金属(如 Na、K、Li)反应生成挥发性氯化物,说明氯化对碱金属杂质去除效果较好。

从整体杂质变化来看,总杂质从 189.5ppm 降至 8.75ppm,总去除率达 95.38%,满足高纯石英 (HPQ) 的总杂质<50ppm 标准。Al 最终含量 4.68ppm 满足半导体及光伏级高纯石英砂要求,但 Ca(1.64ppm)仍高于高端应用门槛。总体而言,该样品已经具有制成半导体及光伏级高纯石英砂的应用潜力,但仍需在 Ca 含量和工艺稳定性上进一步突破。

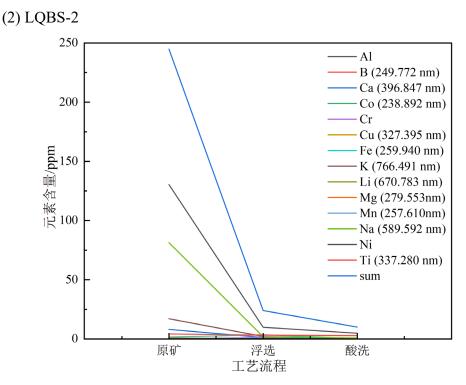
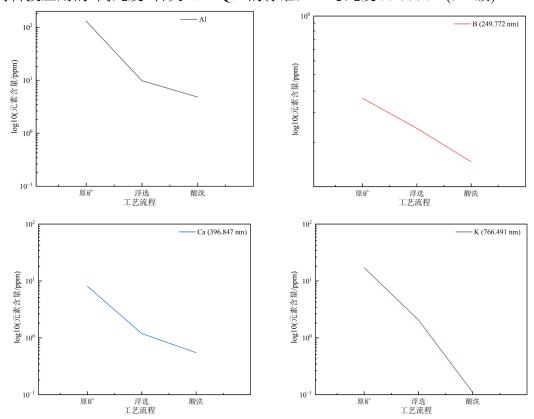


图 4-8 LQBS-2 样品各工艺阶段元素变化

Figure 4-8 Elemental changes in each process stage of the LQBS-2 sample

如图所示,LQBS-2 样品经浮选-酸洗工艺处理后,各杂质元素含量明显降低,其中,总杂质元素含量浓度<50ppm,Al<30ppm,Ti<10ppm,符合定义为适用于高科技应用的"高纯度"石英(HPQ)的标准,SiO2 纯度 99.9990%(5N 级)。



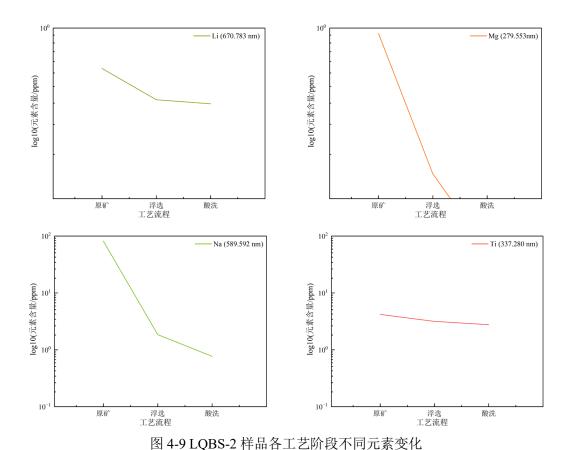


Figure 4-9 Changes of different elements in each process stage of LQBS-2 sample 表 4-4 LQBS-2 样品 ICP-OES 元素检测结果

Table 4-4 ICP-OES element test results of LQBS-2 sample

| | | | | | _ | 1 | | |
|-----------|----------|----------|----------|----------|------|----------|----------|----------|
| 样品编号 | Al | В | Ca | Co | Cr | Cu | Fe | K |
| | | (249.772 | (396.847 | (238.892 | | (327.395 | (259.940 | (766.491 |
| | | nm) | nm) | nm) | | nm) | nm) | nm) |
| LQBS-2 原矿 | 130.37 | 0.33 | 8.06 | 0.03 | 0.09 | 0.07 | 1.65 | 17.05 |
| LQBS-2 浮选 | 9.81 | 0.22 | 1.19 | 0.01 | 1.18 | 0.05 | 3.47 | 2.06 |
| LQBS-2 酸测 | 4.82 | 0.14 | 0.55 | 0.01 | 0.03 | 0.04 | 0.27 | 0.11 |
| 样品编号 | Li | Mg | Mn | Na | Ni | Ti | sum | |
| | (670.783 | (279.553 | (257.610 | (589.592 | | (337.280 | | |
| | nm) | nm) | nm) | nm) | | nm) | | |
| LQBS-2 原矿 | 0.58 | 0.93 | 0.09 | 81.38 | 0.01 | 4.19 | 244.83 | |
| LQBS-2 浮选 | 0.38 | 0.14 | 0.03 | 1.85 | 0.44 | 3.16 | 23.99 | |
| LQBS-2 酸测 | 0.36 | 0.05 | 0.01 | 0.77 | 0.02 | 2.77 | 9.95 | |

如图 4-8、4-9 及表 4-4 所示, LQBS-2 原矿样品中 Al 含量为 130.37ppm, Na 含量为 81.38ppm, Fe 含量为 1.65ppm, 这表明原矿中可能富含钠长石、云母等矿物, 而铁矿物含量较低。经过浮选处理后 Al 从 130.37ppm 降至 9.81ppm, 去除率达 92.5%; Na 从 81.38ppm 降至 1.85ppm, 去除率达 97.7%, 证明浮选对钠长石和云母的分离效率极高。经过酸洗处理后, Al 从 9.81ppm 降至 4.82ppm, 去

除率 50.9%; Fe 从 3.47ppm 降至 0.27ppm, 去除率 92.2%, 说明酸洗对金属元素的去除效果显著。

从整体杂质变化来看,总杂质从 244.83ppm 降至 9.95ppm,总去除率达 95.94%,满足高纯石英 (HPQ) 的总杂质<50ppm 标准。总体而言,LQBS-2 样品 已具有制备半导体及光伏级高纯石英砂的潜力。

(3) LQBS-3

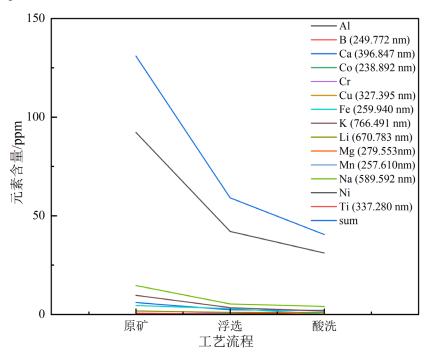
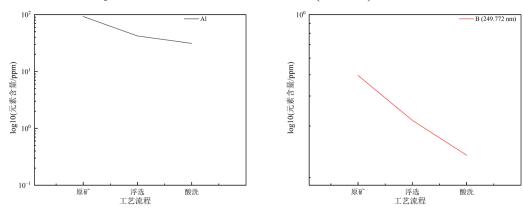


图 4-10 LQBS-3 样品各工艺阶段元素变化

Figure 4-10 Elemental changes in each process stage of the LQBS-3 sample

如图所示,LQBS-3 样品经浮选-酸洗工艺处理后,总杂质元素含量浓度 <50ppm,Al 接近 30ppm,Ti<10ppm,整体元素含量接近适用于高科技应用的"高纯度"石英(HPQ)的标准,SiO₂纯度 99.996%(4N6 级)。



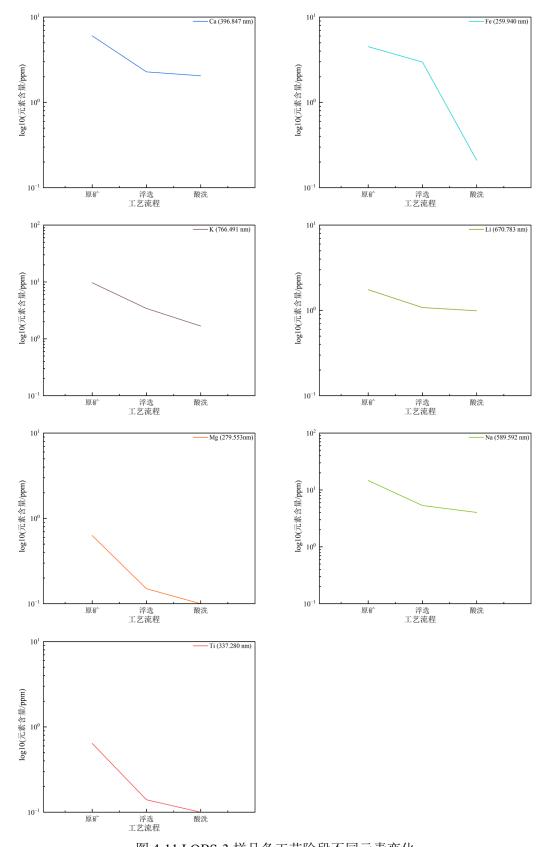


图 4-11 LQBS-3 样品各工艺阶段不同元素变化

Figure 4-11 Changes of different elements in each process stage of LQBS-3 sample

| 表 4-5 LQBS-3 样品 ICP-OES 元素检测结果 | |
|---|---|
| Table 4-5 ICP-OES element test results of LQBS-3 sample | e |

| 样品编号 | Al | В | Ca | Co | Cr | Cu | Fe | K |
|---------------|----------|----------|----------|----------|------|----------|----------|----------|
| | | (249.772 | (396.847 | (238.892 | | (327.395 | (259.940 | (766.491 |
| | | nm) | nm) | nm) | | nm) | nm) | nm) |
| LQBS-3 原矿 | 92.23 | 0.44 | 6.02 | 0.02 | 0.04 | 0.11 | 4.5 | 9.67 |
| LQBS-3 浮选 | 42.08 | 0.24 | 2.28 | 0.01 | 0.99 | 0.03 | 2.97 | 3.42 |
| LQBS-3 样 1 酸测 | 30.73 | 0.17 | 2.15 | 0 | 0.02 | 0.02 | 0.17 | 1.67 |
| LQBS-3 样 2 酸测 | 31.12 | 0.15 | 2.05 | 0.01 | 0.02 | 0.02 | 0.21 | 1.68 |
| 样品编号 | Li | Mg | Mn | Na | Ni | Ti | sum | |
| | (670.783 | (279.553 | (257.610 | (589.592 | | (337.280 | | |
| | nm) | nm) | nm) | nm) | | nm) | | |
| LQBS-3 原矿 | 1.75 | 0.63 | 0.15 | 14.66 | 0.09 | 0.64 | 130.95 | _ |
| LQBS-3 浮选 | 1.08 | 0.15 | 0.02 | 5.32 | 0.35 | 0.14 | 59.08 | |
| LQBS-3 样 1 酸测 | 0.98 | 0.1 | 0.01 | 3.9 | 0.02 | 0.11 | 40.05 | |
| LQBS-3 样 2 酸测 | 0.99 | 0.1 | 0.01 | 4.02 | 0.01 | 0.1 | 40.49 | |

如图 4-10、4-11 及表 4-5 所示, LQBS-3 原矿总杂质含量为 131.03ppm, Al、 Na 和 K 是主要杂质, Al、Na 和 K 含量较高。经浮选处理后, Al 从 92.23ppm 降 至 42.08ppm, 去除率为 54.3%, Na 和 K 的去除率分别为 63.7%和 64.6%。经酸 洗处理后,总杂质减少至40.05ppm,Fe从2.97ppm降至0.17ppm,去除率达94.3%, 但 Al 从 42.08ppm 降至 30.73ppm, 去除率仅为 26.9%, 是限制纯度提升的主要 问题。两次酸洗的检测结果高度一致,证明了工艺稳定性较好,样品酸洗后 Na 含量还是比较高,大约在 4ppm,K 含量为 1.6ppm,碱金属含量比较高,可能是 流体包裹体含量较多,含有较多碱金属和碱土金属元素。

LOBS-3 在 Na、K 和 Fe 上去除效果明显,但其 Al 含量仍较高,还需后续引 入氯化或改变酸洗配方等方法进一步除杂,LQBS-3 由于其瓷白特性,可尝试作 为乳白坨料。

(4) LQBS-4 和 LQBS-5 表 4-6 LQBS-4 样品 ICP-OES 元素检测结果 Table 4-6 ICP-OES elemental test results of LQBS-4 sample

0.39

114.94

样品编号

LQBS-4 样 2 酸测

K A1 В Fe Ca Co Cr Cu (249.772 (396.847 (238.892 (327.395 (259.940 (766.491 nm) nm) nm) nm) nm) nm) LQBS-4 样 1 酸测 118.24 0.39 0.46 0.01 0.02 0.03 1.48 1.8

0.01

0.02

0.04

1.44

1.72

0.47

| 样品编号 | Li | Mg | Mn | Na | Ni | Ti | sum |
|---------------|----------|----------|----------|----------|------|----------|--------|
| | (670.783 | (279.553 | (257.610 | (589.592 | | (337.280 | |
| | nm) | nm) | nm) | nm) | | nm) | |
| LQBS-4 样 1 酸测 | 5.38 | 0.2 | 0.24 | 6.97 | 0.01 | 17.4 | 152.63 |
| LQBS-4 样 2 酸测 | 5.23 | 0.2 | 0.24 | 6.75 | 0.02 | 17.01 | 148.48 |

表 4-7 LQBS-5 样品 ICP-OES 元素检测结果

Table 4-7 ICP-OES elemental test results of LQBS-5 sample

| | | | | ` | | 1 | | |
|---------------|----------|----------|----------|----------|------|----------|----------|----------|
| 样品编号 | Al | В | Ca | Co | Cr | Cu | Fe | K |
| | | (249.772 | (396.847 | (238.892 | | (327.395 | (259.940 | (766.491 |
| | | nm) | nm) | nm) | | nm) | nm) | nm) |
| LQBS-5 样 1 酸测 | 112.57 | 0.51 | 0.43 | 0.01 | 0.02 | 0.03 | 1.4 | 1.59 |
| LQBS-5 样 2 酸测 | 111.72 | 0.4 | 0.56 | 0.01 | 0.02 | 0.03 | 1.43 | 1.61 |
| 样品编号 | Li | Mg | Mn | Na | Ni | Ti | sum | |
| | (670.783 | (279.553 | (257.610 | (589.592 | | (337.280 | | |
| | nm) | nm) | nm) | nm) | | nm) | | |
| LQBS-5 样 1 酸测 | 5.06 | 0.19 | 0.23 | 6.43 | 0.03 | 16.38 | 144.88 | |
| LQBS-5 样 2 酸测 | 5.05 | 0.21 | 0.23 | 6.37 | 0.02 | 16.33 | 143.99 | |

LQBS-4 和 LQBS-5 样品由于其原矿品位低,提纯效果受限,经过一系列提纯工艺后,杂质元素仍大量残留,无论是总含量还是单项元素含量均远超高纯石英标准,总杂质含量在 140ppm 左右,这一结果与其显微镜下特征中含有大量的流体包裹体、石英表面浑浊、气液包裹体片状广泛分布相呼应,证实其不具备成为高纯石英砂 4N5 级石英砂的潜力。

LQBS-4 和 LQBS-5 样品现阶段仅适用于低端工业硅领域,若想将其加工成半导体及光伏级高纯石英砂,主要存在两方面限制:一是因为原矿本身品位低难以满足高端需求;二是需要经过多道复杂提纯工序,经济成本大幅增加。

4.4 样品对比(Sample Comparison)

根据第四章 ICP-OES 检测结果,对五个样品(LQBS-1 到 LQBS-5)的总杂质去除率和主要元素去除率进行分析,同时根据前文 2.3 章节给出的标准对比成品,判断工艺效果。

4.4.1 总杂质去除率对比

表 4-8 各样品总杂质去除率

Table 4-8 Total impurity removal rate of each sample

| 样品编号 | 原矿总杂质 (ppm) | 酸洗后总杂质(ppm) | 总杂质去除率(%) |
|------|--------------|---------------|-----------|
| | 床》心示灰(ppiii) | 政机用心示灰(ppiii) | 心亦灰 4 |

| LQBS-1 | 189.5 | 12.37 | 93.5% |
|--------|--------|--------|-------|
| LQBS-2 | 244.83 | 9.95 | 95.9% |
| LQBS-3 | 130.95 | 40.49 | 69.1% |
| LQBS-4 | - | 148.48 | - |
| LQBS-5 | - | 143.99 | - |

LQBS-1 和 LQBS-2 总杂质去除率均超 90%, 达到高纯石英标准(总杂质 <50ppm)。LQBS-1 经酸洗后总杂质降至 12.37ppm, LQBS-2 酸洗后总杂质降至 9.95ppm, LQBS-3 去除率为 69.08%, 总杂质降至 40.49ppm。LQBS-4 和 LQBS-5 原矿品位低, 酸洗后总杂质仍超 150ppm, 无法满足高纯要求。

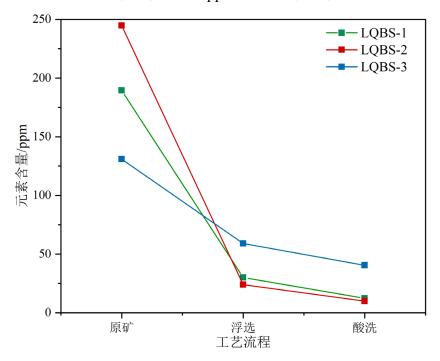


图 4-12 各样品不同工艺流程的总杂质含量

Figure 4-12 The total impurity content of each sample in different processes

4.4.2 主要元素去除率对比

(1) Al

表 4-9 各样品 Al 去除率 Table 4-9 Al removal rate of each sample

| 样品编号 | 原矿含量 (ppm) | 处理后含量 (ppm) | 去除率(%) |
|--------|------------|-------------|--------|
| LQBS-1 | 39.86 | 6.37 | 84.0% |
| LQBS-2 | 130.37 | 4.82 | 96.3% |
| LQBS-3 | 92.23 | 31.12 | 66.7% |
| LQBS-4 | - | 114.94 | - |
| LQBS-5 | - | 111.72 | - |

(2) Fe

表 4-10 各样品 Fe 去除率

| Table 4-10 Fe removal rate of each sample |
|---|
|---|

| 样品编号 | 原矿含量 (ppm) | 处理后含量 (ppm) | 去除率 (%) |
|--------|------------|-------------|---------|
| LQBS-1 | 124.28 | 0.12 | 99.9% |
| LQBS-2 | 1.65 | 0.27 | 83.6% |
| LQBS-3 | 4.50 | 0.21 | 95.3% |
| LQBS-4 | - | 1.44 | - |
| LQBS-5 | - | 1.43 | - |

(3) Ca

表 4-11 各样品 Ca 去除率

Table 4-11 Ca removal rate of each sample

| 样品编号 | 原矿含量 (ppm) | 处理后含量(ppm) | 去除率(%) |
|--------|------------|------------|--------|
| LQBS-1 | 9.63 | 3.15 | 67.3% |
| LQBS-2 | 8.06 | 0.55 | 93.2% |
| LQBS-3 | 6.02 | 2.05 | 65.9% |
| LQBS-4 | - | 0.47 | - |
| LQBS-5 | - | 0.56 | - |

(4) Na

表 4-12 各样品 Na 去除率

Table 4-12 Na removal rate of each sample

| 样品编号 | 原矿含量(ppm) | 处理后含量 (ppm) | 去除率 (%) |
|--------|-----------|-------------|---------|
| LQBS-1 | 3.89 | 1.44 | 62.9% |
| LQBS-2 | 81.38 | 0.77 | 99.05% |
| LQBS-3 | 14.66 | 4.02 | 72.6% |
| LQBS-4 | - | 6.75 | - |
| LQBS-5 | - | 6.37 | - |

(5) Ti

表 4-13 各样品 Ti 去除率

Table 4-13 Ti removal rate of each sample

| 样品编号 | 原矿含量 (ppm) | 处理后含量 (ppm) | 去除率 (%) |
|--------|------------|-------------|---------|
| LQBS-1 | 0.8 | 0.53 | 33.8% |
| LQBS-2 | 4.19 | 2.77 | 33.9% |
| LQBS-3 | 0.64 | 0.1 | 84.4% |
| LQBS-4 | - | 17.01 | - |

LQBS-5 - 16.33 -

由上表可得,LQBS-1 样品 AI 去除率为 84.0%,LQBS-2 样品 AI 去除率为 96.3%,表明该工艺对 AI 的去除效果显著,LQBS-3 的 AI 去除率仅为 66.7%,可能是原矿中 AI 的分布形式较为复杂,需进一步优化工艺。LQBS-1、LQBS-2 和 LQBS-3 三组样品的铁去除率均表现优异,证明工艺对铁的去除能力较强。LQBS-1 和 LQBS-3 的 Ca 含量未达标准,需调整后续工艺以去除。LQBS-2 的 Na 去除率为 99.05%,表明工艺对钠长石等含钠矿物分离效果显著。但 LQBS-1 和 LQBS-3 的去除率偏低,可能是 Na 赋存在石英晶格中难以通过常规工艺去除。

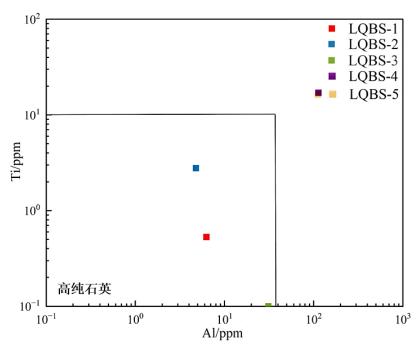


图 4-13 各样品及高纯石英标准

Figure 4-13 Samples and high-purity quartz standards

4.4.3 与业内标准对比

根据 2.3 章节给出的业内标准,对五个样品(LQBS-1 到 LQBS-5)分析如下:

(1) LQBS-1

表 4-14 LQBS-1 与业内标准对比

Table 4-14 Comparison of LQBS-1 with industry standards

| 标准类型 | 关键元素超标项 | 是否符合标准 | 适用领域 |
|------------|----------------------|--------|----------------|
| 光伏用高纯石英砂 | Ca (1.64 ppm)>1 | 部分符合 | 除 Ca 后可用于光伏砂 |
| 石英坩埚高纯内层砂 | Ca (1.64 ppm)>1 | 部分符合 | 除 Ca 后可用于坩埚内层砂 |
| 电子产品用高纯石英砂 | Ca (1.64 ppm)>0.8 | 部分符合 | 除 Ca 后可用于半导体砂 |
| 尤尼明 IOTA-8 | Ca (1.64 ppm) > 0.7 | 部分符合 | 接近 IOTA-8 标准 |
| TQC NW-4A | Ca (1.64 ppm)>1.27 | 部分符合 | 接近 IOTA-8 标准 |

综上: LQBS-1 样品经浮选-酸洗-氯化处理后,总杂质含量为 8.75ppm, SiO₂ 含量达 99.9991%,即 5N 级石英砂,已接近国际顶尖高纯石英砂水平,可经过进一步除 Ca 后作为半导体及光伏级高纯石英砂使用。

(2) LQBS-2

表 4-15 LOBS-2 与业内标准对比

Table 4-15 Comparison of LQBS-2 with industry standards

| 标准类型 | 关键元素超标项 | 是否符合标准 | 适用领域 |
|------------|---------|--------|--------------------|
| 光伏用高纯石英砂 | / | 符合 | 可用于光伏砂 |
| 石英坩埚高纯内层砂 | Al 含量略低 | 部分符合 | 进行掺 Al 工艺后可用于坩埚内层砂 |
| 半导体级高纯石英砂 | / | 符合 | 可作为半导体砂 |
| 尤尼明 IOTA-8 | / | 符合 | 接近 IOTA-8 标准 |

综上: LQBS-2 样品经浮选-酸洗处理后,总杂质含量为 9.95ppm, SiO₂ 含量 达 99.999%,即 5N 级石英砂,但若想作为石英坩埚高纯内层砂使用,Al 含量略低,可在后续加入掺 Al 工艺解决,掺 Al 使 Al 元素含量达到 7-8ppm 后可作为 半导体及光伏级高纯石英砂使用。

(3) LQBS-3

表 4-16 LQBS-3 与业内标准对比

Table 4-16 Comparison of LQBS-3 with industry standards

| 标准类型 | 关键元素超标项 | 是否符合标准 | 适用领域 |
|------------|---------------|--------|----------|
| 光伏用高纯石英砂 | 总杂质 40.49 ppm | 不符合 | 不能用于高端产品 |
| 石英坩埚高纯内层砂 | 总杂质 40.49 ppm | 不符合 | 不能用于高端产品 |
| 半导体级高纯石英砂 | 总杂质 40.49 ppm | 不符合 | 不能用于高端产品 |
| 尤尼明 IOTA-8 | 总杂质 40.49 ppm | 不符合 | 不能用于高端产品 |
| TQC NW-4A | 总杂质 40.49 ppm | 不符合 | 不能用于高端产品 |

综上: LQBS-3 样品经浮选-酸洗处理后,总杂质含量为 40.49ppm,SiO₂ 含量达 99.996%,但多项杂质元素含量均超标,可作为乳白坨料使用。

(4) LQBS-4 和 LQBS-5

所有元素(Al、Ti、Li、Na、K 等)均远超于高纯标准,仅适用于工业硅、玻璃纤维等低端用途,无法用于半导体或光伏领域。

4.5 本章小结(Chapter Summary)

本章通过手标本分析、镜下观察及 ICP-OES 检测,分析了不同工艺阶段石英的杂质去除效果,为工艺流程设计提供数据支撑。

- (1)手标本分析:通过宏观特征判断 LQBS-1 与 LQBS-2 样品呈高品位特征,而 LQBS-4 和 LQBS-5 因铁含量高,初步判定为低品位原料。
- (2)镜下分析:对不同样品进行镜下分析,发现随着工艺的进行,包裹体数量显著减少,证明煅烧-酸浸-氯化工艺对包裹体的有效去除能力。

(3)ICP-OES 分析: LQBS-1 总杂质由 189.5ppm 降至 8.75ppm, 去除率 95.38%, SiO₂ 含量达 99.999%, 可作为半导体及光伏级高纯石英砂使用; LQBS-2 由 244.83ppm 降至 9.95ppm, 去除率 95.94%, SiO₂ 含量达 99.999%, 可作为半导体及光伏级高纯石英砂使用; LQBS-3 因总杂质元素残留量较高需强化提纯,可做乳白坨料; LQBS-4 和 LQBS-5 因原矿品位低,总杂质超限,仅适用于低端领域。

5 结论与展望

5 Conclusion and Outlook

5.1 结论(Conclusion)

本研究以脉石英为原料,设计了一套从物理选矿到化学提纯的综合工艺流程,通过对样品 LQBS-1 至 LQBS-5 的结果分析,得出不同产地脉石英的提纯潜力及适用领域。

- (1)设计煅烧-水淬、磨矿-筛分、磁选、浮选、酸洗及氯化的综合提纯工艺。 煅烧-水淬(1050℃)降低了石英的机械强度,有效去除石英中的流体包裹体,磁选 利用矿物的磁性,去除铁磁性杂质,浮选在酸性条件下利用捕收剂和抑制剂,成 功分离石英砂和长石、云母等杂质矿物,酸洗采用 HCL:HF:HNO₃ 为 3:1:1 的混 合酸,进一步去除石英内部杂质,氯化利用高温氯气,将碱金属(Na、K、Li) 转化为挥发性氯化物,有效去除碱金属杂质。
- (2) 采用手标本分析、镜下观察及 ICP-OES 检测,对比分析不同工艺阶段石英的杂质去除效果。LQBS-1: 总杂质降至 8.75ppm,SiO₂ 含量达 99.999%,即 5N级石英砂,经过进一步除 Ca 后可作为半导体及光伏级高纯石英砂使用。LQBS-2: 总杂质降至 9.95ppm,SiO₂ 含量达 99.999%,即 5N 级石英砂,掺 Al 后可作为半导体及光伏级高纯石英砂使用。LQBS-3: 总杂质降至 40.50 ppm 以下 SiO₂ 含量达 99.996%,即 4N6 级石英砂,可作为乳白坨料使用。LQBS-4 和 LQBS-5: 所有元素均远超标准,无法用于半导体或光伏领域。
- (3)对比分析不同产地的脉石英原矿品位及除杂效果。非洲(LQBS-1):原矿品位高,成品接近国际顶尖水平;印度(LQBS-2):浮选效率优异,但Al含量略低,后续需进行掺Al工艺;中国贵州(LQBS-3):原矿含少量水晶,酸浸难以完全去除;中国黑龙江(LQBS-4/LQBS-5)提纯成本高,经济性差。

5.2 展望(Outlook)

本文系统的研究了脉石英制备半导体及光伏级高纯石英砂的工艺流程,验证了煅烧-水淬、磨矿-筛分、磁选、浮选、酸洗及氯化综合工艺的可行性,并通过试验揭示了不同产地脉石英的提纯潜力。尽管取得了阶段性成果,但由于时间和能力有限,还存在一些问题有待研究。

- (1) 现有工艺对 Ca 的去除仍不完全,需进一步优化酸洗及氯化工艺。
- (2) 优质矿源高度依赖进口,应加强对我国高潜力脉石英矿床筛选。
- (3) 工艺内包含强酸及氯气,存在环境风险,未来可探索绿色替代方案。

参考文献

- [1] 李作敏,谭秀民,张亮,等.我国石英资源的开发利用特点及应用进展[J].矿产保护利用,202 4,44(02):115-123.
- [2] 唐翠华, 魏景明, 朱建喜,等. SiO₂ 同质多象体矿物表面差异性及其对有机物吸附的初步研究[J]. 矿物学报, 2012(s1):49-49.
- [3] MÜLLER A, WANVIK J E, IHLEN P M. Petrological and chemical characterisation of high-purity quartz deposits with examples from Norway[M]. Berlin: Springer, 2012: 71-118.
- [4] 张艳红,杨静,韩雅芳,等.高纯石英的发展现状、消费及市场预测[J].建材世界,2023,44(02):
- [5] 张生辉,王振涛,李永胜,等.中国关键矿产清单、应用与全球格局[J].矿产保护与利用,2022,42(05):138-168.
- [6] 刘国库,张文军,马正先,等.硅石选矿提纯工艺研究现状[J].有色矿冶,2007,(06):26-30.
- [7] 彭寿,陈志强.我国硅质原料产业现状及发展趋势[J].国外建材科技,2008,(02):40-46.
- [8] 郝文俊,詹建华,张徐,等.安徽脉石英矿地质特征及成矿规律探讨[J].中国非金属矿工业导刊,2024,(02):1-5.
- [9] 胡修权,张立,张晋,等.湖北部分区域不同类型硅质原料矿物学特征研究[J].中国非金属矿工业导刊,2024,(06):33-38+88.
- [10] 詹建华,王依,陈正国,等.我国脉石英资源现状分析[J].中国非金属矿工业导刊,2020,(05):1-4.
- [11] 刘慧阳,孙增青,李晓宇,等.高纯石英砂氯化焙烧技术研究进展[J/OL].化工矿物与加工,1-9[2025-05-21].http://kns.cnki.net/kcms/detail/32.1492.TQ.20240925.1621.012.html.
- [12] 张大虎.以脉石英为原料加工 5N 高纯石英的试验研究[D].成都:成都理工大学, 2016.
- [13] 王九一.全球高纯石英原料矿的资源分布与开发现状[J].岩石矿物学杂志,2021,40(01):13 1-141.
- [14] 申士富.高纯石英砂研究与生产现状[J].中国非金属矿工业导刊,2006,(05):13-16.
- [15] 王登红,王岩,陈郑辉,等.试论高纯石英原料矿的找矿方向[J].地球学报,2025,46(01):8-14.
- [16] 胡晓宙.天然石英砂的应用矿物学研究[D].成都:成都理工大学,2020.
- [17] 于雷.中国石英砂资源概况及应用前景分析[J].吉林地质,2024,43(02):17-22.
- [18] 刘理根,高惠民,张凌燕.高纯石英砂选矿工艺研究[J].非金属矿,1996,(04):39-41+14.
- [19] 茆令文,谷翠红,吴建新,等.脉石英替代水晶生产高纯石英砂试验研究[J].建材世界,2010,3 1(01):1-4.
- [20] 滕伟峰,高纯石英提纯加工及酸浸废水处理工艺研究[D].成都:成都理工大学,2021.

- [21] 张亮,刘磊,朱黎宽,等.关于高纯石英原料矿石地质学评价方法的探讨[J].岩石学报,2024,4 0(04):1311-1326.
- [22] 裴振宇.脉石英反浮选与加压浸出纯化新技术研究[D].武汉:武汉理工大学,2014.
- [23] Hou Q L, Li J, Yin R M, et al. Study on Gas-Liquid Inclusions in Quartz Sand und er Microwave Field[J]. Advanced Materials Research, 2012, 581: 689-693.
- [24] 汤中昉.脉石英包裹体特征及其对高纯石英提纯效果的影响[D].成都:成都理工大学,201 8.
- [25] Lin M, Liu Z, Wei Y, et al. A critical review on the mineralogy and processing for high-grade quartz[J]. Mining, Metallurgy & Exploration, 2020, 37: 1627-1639.
- [26] 董芸谷.晶体硅太阳能电池正面银浆用玻璃粉的制备与研究[D].上海:东华大学,2020.
- [27] 杜鑫.粉石英矿高纯加工基础与选矿提纯工艺研究[D].北京:中国矿业大学(北京),2022.
- [28] Xudong W, Pei N I, Shunda Y, et al. Fluid inclusion studies of the Huangsha quartz-vein type tungsten deposit, Jiangxi Province[J]. Acta Petrologica Sinica, 2012, 28(1): 122-132.
- [29] 武志超,张海啟,谭秀民,等.高纯石英应用及化学提纯技术研究进展[J].化工矿物与加工,2 023,52(09):72-80.
- [30] Wang S, Yu D, Ma C, et al. A New Insight into the Influence of Fluid Inclusions in High-Purity Quartz Sand on the Bubble Defects in Quartz Glass: A Case Study from Vein Quartz in the Dabie Mountain[J]. Minerals, 2024, 14(8): 794.
- [31] Wei Z, Li Y, Li P, et al. Migration Mechanisms of Al3+/Li+ Lattice Impurities durin g Phase Transition from α-Quartz to β-Quartz: An Implication for Purification of Hig h-Purity Quartz[J]. Minerals, 2023, 13(10): 1280.
- [32] 陈平飞.广西灌阳石英矿中金属杂质剔除工艺研究[D].株洲:湖南工业大学,2021.
- [33] 郜润博,黄业豪,尚保忠,等.高纯石英加工提纯技术研究现状与展望[J/OL].中国矿业,1-16 [2025-05-21].http://kns.cnki.net/kcms/detail/11.3033.td.20250418.1017.004.html.
- [34] 曾牧源,马博华,赵李欣然,等.湖北省恩施某光伏玻璃用石英砂提纯制备实验[J].矿产综合利用,2024,45(02):144-150.
- [35] 国洪晨,沈建兴,王泰林,等.物理处理在超纯石英制备中的作用[J].山东陶瓷,2020,43(04):1 0-14.
- [36] 徐雯雯.高纯石英粉制备工艺研究[D].青岛:中国海洋大学,2013.
- [37] 葛禧龙,任子杰,印航,等.难选粗粒长石与石英浮选分离药剂优化试验研究[J].化工矿物与加工,2024,53(11):24-29.
- [38] L·阿历山大诺娃,魏明安. 温度对石英-十二胺浮选体系中物理化学特性的影响[J]. 国外金属矿选矿,1999(8):2-6.

- [39] A·M·维艾拉, 张兴仁, 等. 胺的种类、PH 和矿粒粒度对石英浮选的影响[J]. 国外金属矿选矿, 2007, 44(12):31-34.
- [40] 王睿哲.低品位石英矿中高岭土的去除研究[D].昆明:昆明理工大学,2024.
- [41] 王硕,聂轶苗,刘永强,等.石英矿中杂质赋存状态与去除方法研究进展[J/OL].矿产综合利用,1-10[2025-05-21].http://kns.cnki.net/kcms/detail/51.1251.TD.20250116.1233.002.html.
- [42] 李爱民.我国石英与长石浮选分离的研究进展[J].矿产保护与利用,2021,41(06):27-34.
- [43] 汪灵, 李彩侠, 王艳. 一种以脉石英为原料加工 4N 高纯石英的方法[P]. 中国, CN1028 87519A, 2013-1-23.
- [44] 张煜.陕西汉中石英砂岩酸浸除铁实验研究[D].成都:成都理工大学,2023.
- [45] 汪本高,安莲英,黎春阁. 石英砂提纯工艺研究[J]. IM&P 化工矿物与加工,2013,3: 15-18.
- [46] 苏英, 周永恒, 黄武, 等. 石英玻璃与 HF 酸反应动力学的研究[J]. 硅酸盐学报, 2004,3 2(3):287-293.
- [47] 汪本高,李丹妮. 乐山石英础岩除铁提纯试验研究[J]. 中国非金属矿工业导刊,2013,3:24-27.
- [48] 马超,冯安生,刘长淼,等.高纯石英原料矿物学特征与加工技术进展[J].矿产保护与利用,2 019,39(06):48-57.
- [49] 潘俊良.氯化焙烧法制备 4N8 标准级高纯石英试验研究[D].成都:成都理工大学,2015.
- [50] Guo W, Lu H, Zhang Z, et al. Crystal structure transformation and lattice impurities migration of quartz during chlorine roasting[J]. International Journal of Mining Scienc e and Technology, 2024, 34(10): 1465-1474.
- [51] 施娅颖,王小强,张会,等.高纯石英的杂质类型及深度提纯技术研究进展[J].造纸装备及材料,2023,52(12):76-78.
- [52] 吴逍,孙红娟,彭同江,等.青海某地脉石英矿工艺矿物学研究及可选性试验[J].矿治,2015,2 4(02):71-77.
- [53] 董园园,张俊美,徐智宝,等.电感耦合等离子体发射光谱法测定铅精矿中二氧化硅含量[J]. 冶金与材料,2023,43(05):67-69.
- [54] 黄京柠,余吹儿,陈旗标,等.地质岩矿样品中稀有元素的 ICP-OES 分析测试[J].世界有色金属,2024,(23):190-192.

翻译部分

英文原文





Article

Trace Element Compositions and Defect Structures of High-Purity Quartz from the Southern Ural Region, Russia

Jens Götze 1,*, Yuanming Pan 2, Axel Müller 3,4, Elena L. Kotova 5 and Daniele Cerin 2

- Institute of Mineralogy, TU Bergakademie Freiberg, Brennhausgasse 14, 09596 Freiberg, Germany
- Department of Geological Sciences, University of Saskatchewan, Saskatoon, SK S7N5E2, Canada; yuanming.pan@usask.ca (Y.P.); dac176@mail.usask.ca (D.C.)
- Naturhistorisk Museum, Universitet i Oslo, P.O. Box 1172, Blindern, 0318 Oslo, Norway; a.b.muller@nhm.uio.no
- 4 Natural History Museum, Cromwell Road, London SW7 5BD, UK
- Mining State University St. Petersburg, 21st Line, St. Petersburg 199106, Russia; museum_spmi@spmi.ru
- Correspondence: jens.goetze@mineral.tu-freiberg.de; Tel.: +49-3731-392638

Received: 14 September 2017; Accepted: 5 October 2017; Published: 11 October 2017

Abstract: Quartz samples of different origin from 10 localities in the Southern Ural region, Russia have been investigated to characterize their trace element compositions and defect structures. The analytical combination of cathodoluminescence (CL) microscopy and spectroscopy, electron paramagnetic resonance (EPR) spectroscopy, and trace-element analysis by inductively coupled plasma mass spectrometry (ICP-MS) revealed that almost all investigated quartz samples showed very low concentrations of trace elements (cumulative concentrations of <50 ppm with <30 ppm Al and <10 ppm 'f') and low abundances of paramagnetic defects, defining them economically as "high-purity" quartz (HPQ) suitable for high-tech applications. EPR and CL data confirmed the low abundances of substitutional Ti and Fe, and showed Al to be the only significant trace element structurally bound in the investigated quartz samples. CL microscopy revealed a heterogeneous distribution of luminescence centres (i.e., luminescence active trace elements such as Al) as well as features of deformation and recrystallization. It is suggested that healing of defects due to deformation-related recrystallization and reorganization processes of the quartz lattice during retrograde metamorphism resulted in low concentrations of CL activator and other trace elements or vacancies, and thus are the main driving processes for the formation of HPQ deposits in the investigated area.

Keywords: quartz; cathodoluminescence; electron paramagnetic resonance; trace elements

1. Introduction

Quartz and other silica minerals are some of the most important rock-forming minerals of the Earth's crust, and are important industrial raw materials. Owing to their abundance and physical and chemical properties, natural silica raw materials have a wide range of industrial and technological applications [1,2].

In particular, high-purity quartz (HPQ), with less than 50 ppm of contaminating trace elements [3,4], is of high economic value, resulting in prices up to 20 times higher than those of low-quality ("common") silica raw materials [5,6]. High-purity quartz is of strategic importance for the high-tech industry, because it is a critical material for the manufacture of crucibles used for single crystal growth of silicon metal (needed for solar panel and micro-chip production), high-temperature lamp tubing, telecommunications, optics, and semiconductor materials. Because

Minerals 2017, 7, 189 2 of 19

of the increasing demand for HPQ there are increasing exploration activities underway to search for potential deposits worldwide.

The specific quality requirements of the quartz material are challenging with respect to analytics due to the very low concentrations (from 0.1 to 50 ppm) of impurity trace elements [2]. Natural silica materials, in particular quartz, are characterized by specific properties—including lattice defects, abundance of lattice-"foreign" trace elements, degree of recrystallization, etc.—which are the result of the regional geological history and the related specific conditions of formation. Therefore, the knowledge of the interrelations between genetic conditions and quartz properties can be used both for the reconstruction of geological processes and for the prediction of deposit location and quality as well as for specific industrial applications [7]. In particular, information about the number and types of defects is important for the processing of the raw materials and the potential technical applications.

The present study presents results of a comprehensive mineralogical and geochemical study on potential HPQ deposits of different genetic types from 10 sites in the Southern Ural region, Russia. The investigation aims to obtain detailed information about the type and abundance of lattice defects and contaminating trace elements of these quartz materials in order to determine the critical processes and conditions responsible for the formation of HPQ deposits. This aim is achieved by a combination of multiple high-sensitivity analytical techniques ranging from cathodoluminescence (CL) microscopy and spectroscopy to electron paramagnetic resonance (EPR) spectroscopy and trace-element analysis by inductively coupled plasma mass spectrometry (ICP-MS) and laser ablation ICP-MS.

2. Materials and Methods

2.1. Geological Background and Sample Material

Potential high-purity quartz from 10 different localities of the Southern Ural region northwest of Chelyabinsk (Russia) was investigated (Figure 1, Table 1). The sample material includes quartz from a pegmatite, hydrothermal quartz veins, tectonically deformed and partially recrystallized hydrothermal quartz, and quartz from two quartzite occurrences.

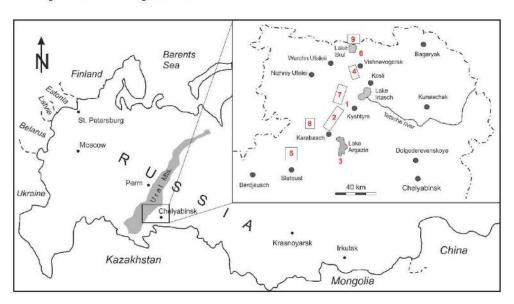


Figure 1. Topographic sketch showing the investigated quartz occurrences of the Southern Ural region northwest of Chelyabinsk (Russia); 1—Berkutinskaya (Berkut), 2—Kyshtym (sample Ky-175), 3—Argazinskoe (Arg), 4—Vjasovka (Vja), 5—Itkulskoe (Itkul), 6—Bolotnaya (Bol), 7—Kuznechikhinsk (Ku-414, Ku-2136), 8—Yurma ridge (Yur), and 9—Taganai ridge (MT-09). Numbers relate to the locations and quartz types in Table 1.

Minerals 2017, 7, 189 3 of 19

| Table 1. Investigate | d quartz samples fro | m the Southern U | ral region (Russia). |
|----------------------|----------------------|------------------|----------------------|
|----------------------|----------------------|------------------|----------------------|

| Location Type | | Sample |
|------------------|--|---------|
| 1 Berkutinskaya | Pegmatite | Berkut |
| 2 Kyshtym | Hydrothermal vein | Ky-175 |
| 3 Argazinskoe | Hydrothermal vein | Arg |
| 4 Vjazovka | Hydrothermal vein | Vja |
| 5 Itkulskoe | Hydrothermal vein | Itkul |
| 6 Bolotnaya | Hydrothermal vein | Bol |
| 7 Kuznechikhinsk | Hydrothermal vein, metamorphic overprint | Ku-414 |
| 7 Kuznechikhinsk | Hydrothermal vein, metamorphic overprint | Ku-2136 |
| 8 Yurma ridge | Quartzite | Yur |
| 9 Taganai ridge | Quartzite | MT-09 |

All quartz bodies occur within the Ufalei metamorphic (gneiss—migmatite) complex, consisting of two tectonometamorphic units which lay on top of each other. Highly metamorphosed Upper Proterozoic rocks of the Ufalei suite belong to the lower unit and form the core of an anticlinorium. The hydrothermal vein deposits from Kyshtym (sample Ky-175), Kuznechikhinsk (10 km southwest of Kosli, samples Ku-414, Ku-2136), and Argazinskoe (on the southwest coast of Lake Argazin, sample Arg), and the quartzite massifs of Yurma (north of Karabasch on the Yurma ridge) as well as the Taganai ridge (north of Slatoust, sample MT-09) are situated within this unit (Table 1). The pegmatite body of the Berkutinskaya deposit is situated within the Berkut ridge near Kyschtym. The upper unit of the Ufalei metamorphic complex comprises Ordovician and Lower Devonian sequences represented by terrigenous schistose meta-sediments surrounding the anticlinorium core. This unit hosts the hydrothermal vein deposits Vjazovka near Vyschnevogorsk, Bolotnaya and Itkulskoe (north coast of Lake Itkul) (Figure 1, Table 1).

All quartz bodies were formed during long-lasting and multi-stage metamorphism in the Ural region [8]. Two main stages of metamorphism can be distinguished in the investigated area: (1) the Late Cambrian stage, which correlates with the formation of the Ufalei anticlinorium and is subdivided into two sub-stages—an early phase of progressive metamorphism (sillimanite-almandine subfacies of the amphibolite facies), followed by retrograde metamorphism; and (2) the Middle Paleozoic stage, which is characterized by metamorphic transformations of the gneiss core and schist frame (staurolite—quartz subfacies of the amphibolite facies). Silica mobilization and formation of hydrothermal quartz veins and bodies are supposedly related to the retrograde stages of both metamorphic events [9].

2.2. Analytical Methods

Polished thin sections were prepared for microscopic and cathodoluminescence (CL) investigations from all samples listed in Table 1. Polarizing microscopy was carried out using a Zeiss Axio Imager A1m (ZEISS Microscopy, Jena, Germany) to document the grain-size and microstructure of the different quartz types. Micrographs were recorded using a digital camera MRc5 and the software Axiovision (ZEISS Microscopy, Jena, Germany).

CL microscopy and spectroscopy were performed on carbon-coated thin sections using a hot-cathode CL microscope HC1-LM (LUMIC, Bochum, Germany) [10]. The system was operated at 14 kV and 0.2 mA (current density $\sim 10~\mu A/mm^2$) with a defocused electron beam. Luminescence images were captured during CL operations using a peltier cooled digital video-camera (OLYMPUS DP72, OLYMPUS Deutschland GmbH, Hamburg, Germany). CL spectra in the wavelength range of 370–920 nm were recorded with an Acton Research SP-2356 digital triple-grating spectrograph with a Princeton Spec-10 charge-coupled device (CCD) detector (OLYMPUS Deutschland GmbH, Hamburg, Germany) that was attached to the CL microscope by a silica-glass fibre guide. CL spectra were measured under standardized conditions (wavelength calibration by a Hg-halogen lamp, spot width 30 μ m, measuring time 5 s). Irradiation experiments were performed to document the behaviour of the

Minerals 2017, 7, 189 4 of 19

quartz samples under electron irradiation. Samples were irradiated 5 min under constant conditions (14 kV, 0.2 mA) and spectra were measured initially and after every 1 min.

The paramagnetic centres of quartz-powder samples were investigated by EPR spectroscopy using a Bruker EMX spectrometer (Bruker Corporation, Billerica, MA, USA) operated with the X-band microwave frequencies at both room temperature and liquid-nitrogen temperature. Experimental conditions for room-temperature EPR included a microwave frequency of \sim 9.63 GHz, modulation frequency of 100 kHz, modulation amplitude of 0.1 mT, and microwave powers from 0.02 mW to 20 mW. The spectral resolutions were \sim 0.146 mT for wide scans 50–6500 mT and 0.024 mT for narrow scans 300–350 mT. All samples after room-temperature EPR measurements were irradiated at room temperature in a 60 Co cell for a dose of \sim 10 kGy. Low-temperature (85 K) EPR measurements were made immediately after gamma-ray irradiation, with similar experimental conditions used for the room-temperature analyses except for a microwave frequency of \sim 9.39 GHz.

The chemical composition of bulk quartz samples (dissolved powders) was first analysed using solution ICP-MS. The samples (400–500 mg) for ICP-MS analysis were milled to a grain size of <30 μ m using a pre-cleaned agate mortar. The powdered sample was digested in a glassy carbon vessel with 5 mL concentrated HF and 3 mL concentrated HNO₃ at 50 °C (35 min). Rhenium solution (1 mL of 100 μ g·L⁻¹ concentration) was added as an internal standard for the ICP-MS measurements. The analysis was performed using a Perkin Elmer Sciex Elan 5000 quadrupole instrument (Percin Elmer Inc., Baesweiler, Germany) with a cross-flow nebulizer and a rhyton spray chamber. The precision and accuracy of the ICP-MS measurements were evaluated by analysis of the glass sand reference material UNS-SpS. The relative standard deviations for most analytes were below 10%. The ICP-MS results showed procedural limits of detection ranging from 0.22 μ g·L⁻¹ to 3.1 μ g·L⁻¹ for Na, Mg, Al, K, Ca and Ba. Elements such as Li, Mn and Sr had procedural limits of detection ranging from 0.02 to 0.04 μ g·L⁻¹, whereas these limits range from 1 to 7 μ g·L⁻¹ for the other elements investigated [11].

In addition, 200-um polished thick sections of the samples were prepared for laser ablation inductively-coupled plasma mass spectrometry (LA-ICP-MS) to determine trace elements of individual quartz crystals in situ. Concentrations of Li, Be, B, Na, Al, P, K, Ca, Ti, Mn, Fe, Ge, Rb, Sr, Ga, and Sb were analysed with a double-focusing sector field mass spectrometer ELEMENT XR coupled with a NewWave 193-nm excimer laser probe (Thermo Scientific, Waltham, MA, USA) [12]. The laser had a pulse rate of 20 Hz, a speed of 15 μ m·s⁻¹, a spot size of 50 μ m and energy fluence of 5–7 mJ·cm⁻² on the sample surface. Raster ablation was applied on an area of approximately 150 μ m \times 300 μ m. The approximate depth of ablation was about 50 μm. The carrier gas for transport of the ablated material to the ICP-MS was He mixed with Ar. External calibration was performed using three silicate glass reference materials produced by the National Institute of Standards and Technology, USA (NIST SRM 610, 612 and 614). In addition, the NIST SRM 1830 soda-lime float glass (0.1% m/m)Al₂O₃), the certified reference material BAM No.1 amorphous SiO₂ glass from the Federal Institute for Material Research and Testing in Germany, and the Qz-Tu synthetic pure quartz monocrystal provided by Andreas Kronz from the Geowissenschaftliches Zentrum Göttingen (GZG), Germany, were used. Each measurement comprised 15 scans of each isotope, with a measurement time varying from a 0.15 s/scan for K in high resolution to a 0.024 s/scan of, for example, Li in low resolution. A linear regression model, including several measurements of the different reference materials, was used to define the calibration curve for each element. For the calculation of P concentrations, the procedure of Müller et al. [13] was applied. Ten sequential measurements on the Qz-Tu synthetic pure quartz monocrystal were used to estimate the limits of detection (LOD—3σ of 10 measurements; see Table S3). The analytical error ranges within 10% of the absolute concentration of the element.

Minerals 2017, 7, 189 5 of 19

3. Results

3.1. Cathodoluminescence (CL)

CL imaging revealed heterogeneities, intra-crystal micro-structures and micro-inclusions in the quartz samples. The detected micro-inclusions include carbonate (orange CL) in quartz from Bolotnaya, and feldspar (microcline—bright blue CL, albite—bluish-violet CL) in sample Ku-2136, as well as zircon/monazite (bright radiation halos) and mica (non-luminescent) in sample MT-09 (Figure 2).

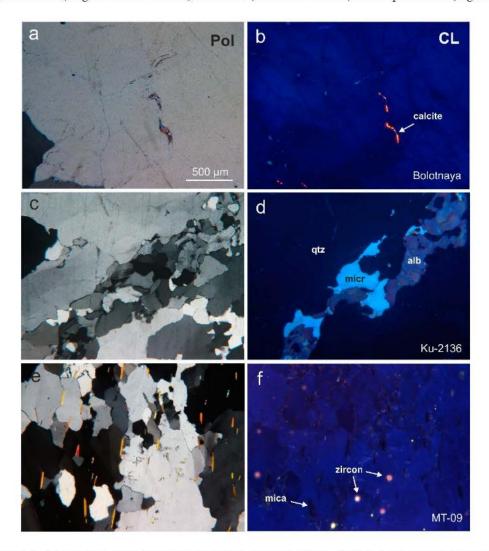


Figure 2. Micrograph pairs in transmitted light (crossed polars—Pol) and cathodoluminescence (CL) showing micro-inclusions of minerals in the quartz samples: (**a**,**b**) calcite in the hydrothermal quartz from Bolothaya (Bolot); (**c**,**d**) microcline (micr) and albite (alb) in metamorphically overprinted hydrothermal quartz from Kuznechikhinsk (Ku-2136; (**e**,**f**) mica (non-luminescent) and zircon with radiation haloes in the quartzite from the Taganai ridge (MT-09).

The micro-inclusions can be related to the composition of the host rocks (e.g., hydrothermal carbonate veins) or the educt material of the metamorphic rocks. Heterogeneities were detected in quartz grains of almost all samples, which appeared homogeneous under polarized light. Moreover, features of alteration and recrystallization/reorganization as well as trails of fluid migration could be revealed by CL (Figure 3).

Minerals 2017, 7, 189 6 of 19

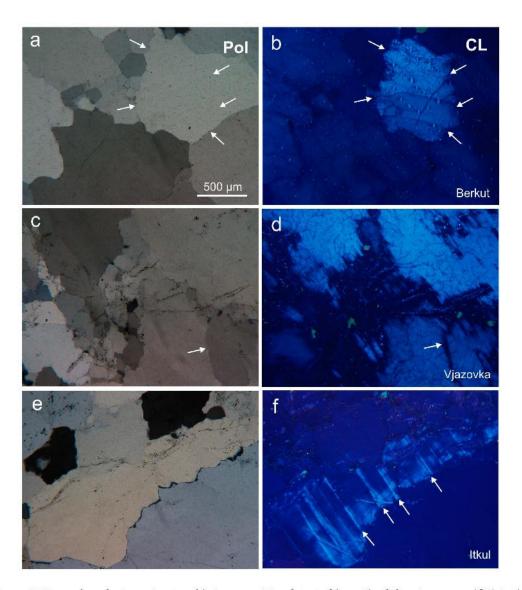


Figure 3. Examples of micro-structural heterogeneities detected by cathodoluminescence (CL) in the investigated quartz samples mostly invisible in transmitted light (crossed polars—Pol): (a,b) brightly luminescing sub-grain areas in the pegmatite quartz from Berkutinskaya (Berkut); (c,d) trails of reduced CL intensity (arrow) due to migration of fluids in the hydrothermal quartz from Vjazovka (Vja); (e,f) dislocation planes in the hydrothermal quartz from Itkulskoe (Itkul).

Pegmatite quartz shows a more or less homogeneous bluish-green CL with a characteristic CL emission band at ca. 500 nm (Figure 4a). Sub-grain areas with strong CL (Figure 3b) have the highest intensities of this 500 nm band indicating the highest amounts of the luminescence related defect(s). The intensity of the 500 nm emission strongly decreases under electron irradiation. The resulting CL spectrum after 5 min of electron bombardment consists of an emission band at 450 nm and a weak band at 650 nm (Figure 4a).

Minerals 2017, 7, 189 7 of 19

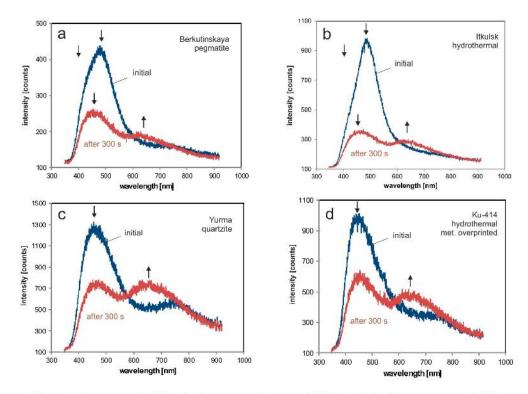


Figure 4. Representative CL emission spectra of quartz of different origin (blue spectrum = initial, red spectrum = after 5 min of electron irradiation): (a) pegmatite quartz; (b) hydrothermal vein quartz; (c) quartzite; (d) tectonically deformed and partially re-crystallized hydrothermal quartz.

Quartz from hydrothermal veins exhibits a typical short-lived blue CL. The initial spectra are mainly composed of a strong band at 500 nm and a second emission band at 390 nm, which is only visible as a shoulder (see arrow in Figure 4b) because of the spectral transmissibility of the used equipment (absorption of the spectral UV region due to glass optics). The CL spectrum after 5 min of electron irradiation is dominated by emission bands at 450 nm and 650 nm, respectively. A conspicuous feature of CL imaging in most hydrothermal quartz samples is a heterogeneous pattern (Figure 3d). Brightly luminescent areas alternate with areas of low CL intensity. Interactions of migrating fluids with the host quartz left their traces in trails of reduced CL intensities (Figure 3d). Moreover, features of deformation are visible during initial electron radiation, but disappear during electron bombardment (Figure 3f).

With increasing deformation degree of hydrothermal quartz the luminescence intensity decreases and the visible CL colour becomes more homogeneous. The typical luminescence emission bands for undeformed hydrothermal quartz at 390 nm and 500 nm are missing. The spectra of deformed hydrothermal quartz are dominated by two bands at 450 nm and 650 nm, respectively (Figure 4d).

Quartzite samples appear commonly heterogeneous under CL and may contain micro-inclusions of minerals probably originating from the primary source rocks (sample MT-09; Figure 2e,f). The quartzite from Yurma does not contain any visible mineral inclusions and represents high-purity material. Quartz from the quartzite samples is characterized by a deep blue CL showing emission bands at 450 nm and 650 nm (Figure 4c).

An orientation-dependent behaviour of the CL during electron irradiation was observed in the hydrothermal quartz from Kyshtym (Ky-175, Figure 5). Sub-grains which are cut perpendicular to the c-axis in thin section (dark in polarized light) show a change of the initial blue CL colour into red-violet

Minerals 2017, 7, 189 8 of 19

(increase of the 650 nm band), whereas sub-grains with other orientations show only a decrease of the initial blue CL (decreasing composite blue emission band).

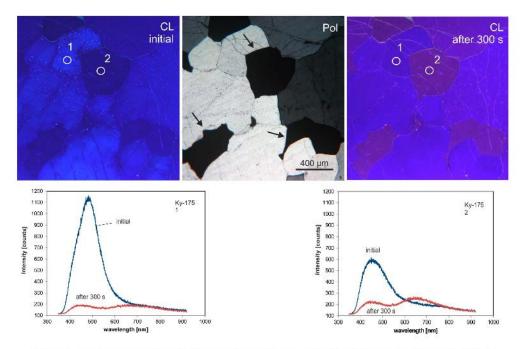


Figure 5. Micrographs in cathodoluminescence (CL) and transmitted light (crossed polars—Pol) of the hydrothermal quartz from Kyshtym (Ky-175); the images and related spectra show the initial CL and the CL after 5 min of electron irradiation. Note the different CL behaviour of quartz sub-grains with varying crystallographic orientation; sub-grains cut perpendicular to the crystallographic c-axis (see arrows) have a lower initial blue CL intensity and develop a reddish CL (650-nm emission band) due to the electron bombardment.

3.2. Electron Paramegnetic Resonance (EPR)

Figures 6 and 7 present the EPR spectra of all quartz samples measured at room temperature. The EPR spectra are essentially featureless, except for the presence of trace and variable amounts of the rhombic Fe^{3+} signal at the effective g value of ~4.38 (Figure 6) [14,15].

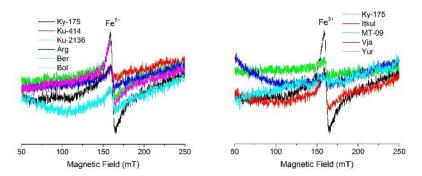


Figure 6. Electron paramagnetic resonance (EPR) spectra of investigated quartz samples taken at room temperature showing the weak rhombic Fe^{3+} signal at $g_{eff} = 4.38$; the intensities are given in arbitrary units.

Minerals 2017, 7, 189 9 of 19

Obviously, the intensity of this signal is low in all samples (i.e., low signal-to-noise ratios) and is variable between samples. Even without a proper standard, it is apparent that the Fe³⁺ signal is exceedingly small in the samples Berkutinskaya (pegmatite), Argazinskoe, Vjasovka (hydrothermal veins), Ku-414 (metamorphically overprinted hydrothermal quartz), MT-09, and Yurma (quartzite). The Fe³⁺ signal is somewhat more elevated in the samples Ky-175, Itkulskoe, Bolotnaja (hydrothermal vein), and Ku-2136 (metamorphically overprinted hydrothermal quartz).

The spectra in Figure 7 show the resonance signals at the central magnetic field region. Again, all spectra have low signal-to-noise ratios. Indeed, none of the radiation-induced defects at the effective g values of ~2.00 are present [16–19]. Even the common E'_1 is exceedingly rare. It should be mentioned that the silica tubes used as sample containers show a very weak E'_1 signal, which contributes to the weak E'_1 signal in the measured spectra (Figure 7).

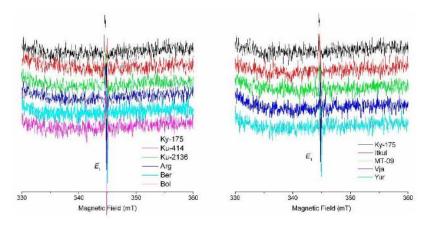


Figure 7. EPR spectra of investigated quartz samples taken at room temperature showing a slight E'_1 but a general absence of other radiation-induced defects at $g_{\rm eff} = 2.0$.

The EPR spectra of gamma-ray-irradiated samples, measured at 85 K, all show the presence of varying amounts of the well-known $[AlO_4]^0$ centre with the characteristic 27 Al hyperfine structure [20] (Figure 8). The paramagnetic $[AlO_4]^0$ centre in quartz has been shown to form from neutral $[AlO_4/M^+]^0$ (M = H, Li, Na, K) precursors (i.e., the monovalent charge compensators migrated away during room-temperature irradiation) [20,21]. Figure 8 compares the individual spectra using the sample Ky-175 as a common reference. The intensities of measured $[AlO_4]^0$ signals of samples Argazinskoje, Bolotnaya and Yurma are notably higher than those of the other samples.

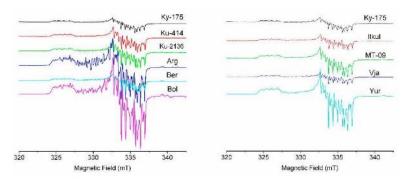


Figure 8. EPR spectra of investigated quartz samples taken at 85 K showing varying quantities of the [AlO₄]⁰ centre.

Minerals 2017, 7, 189 10 of 19

EPR spectra measured at 85 K show again the presence of the Fe³⁺ and the E'₁ centre but a general absence of the Ti- and Ge-associated defects with diagnostic 47 Ti, 49 Ti and 73 Ge hyperfine structures [16,19], confirming the results observed at room temperature.

3.3. Trace Elements

"Bulk" solution ICP-MS: Trace-element concentrations of all investigated quartz samples determined by solution ICP-MS are summarized in Tables S1 and S2. The data illustrate that most quartz samples have low concentrations of most trace elements compared with average concentrations in natural quartz [5,7]. Al concentrations are generally below 100 ppm, and those of Fe and Ti are below 10 ppm. An exception is the quartzite from the Taganai ridge (sample MT-09) which shows elevated concentrations of Al, K, Mg, Ti, Fe, Mn, Zr, U, Th, and Hf. Based on microscopic investigations the elevated concentrations of Al, K, Mg, Ti, Fe and Mn are caused by micro-inclusions of mica and those of Zr, U, Th and Hf by zircon (Figure 2e,f). There are similar effects of micro-inclusions of feldspars (albite, microcline—Figure 2d) in quartz from Kuznechikhinsk (samples Ku-2136—K, Na, Al and Fe) as well as carbonate (Figure 2b) in the sample from Bolotnaja (sample Bolot—Ca, Mg and Fe).

Sodium, Sr, K, Mg, and Rb show positive correlations in the different samples (Figure 9). The abundance of these alkali and alkali earth elements can predominantly be related to the presence of fluid inclusions, although mineral micro-inclusions of feldspar and mica (e.g., samples MT-09, Ku-2136) can also influence these correlations. However, in most of the investigated quartz no mineral inclusions were detected.

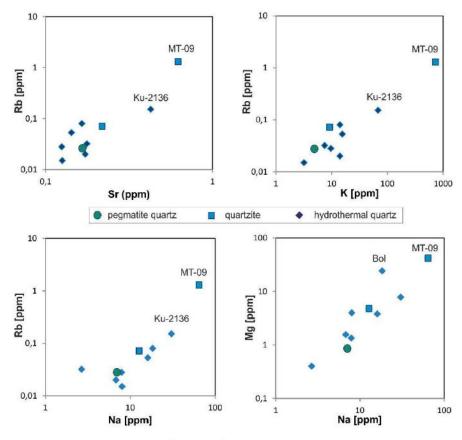


Figure 9. Element ratios of selected alkali and alkali earth elements in the investigated quartz samples (the labelled samples are those with detected mineral inclusions).

Minerals 2017, 7, 189 11 of 19

The rare earth element (REE) concentrations are listed in Table S2 and illustrated in Figure 10. In some samples (Berkutinskaya, Bolotnaya, Ku-414, and Ku-2136) the concentrations of certain rare earth elements are below the detection limit of the applied ICP-MS analysis and, thus, their chondrite-normalized REE distribution patterns are not shown in Figure 10. The REE patterns of the two quartzite samples are different to the patterns of the hydrothermal quartz. In particular, the quartzite sample MT-09 has high absolute REE concentrations with a typical crustal signature of enriched light REE (LREE) and depleted heavy REE (HREE) (Figure 10a). The REE enrichment is most likely be related to micro-inclusions found in this sample. The quartzite from Yurma has much lower REE contents but shows a similar LREE pattern. However, the HREE are slightly enriched.

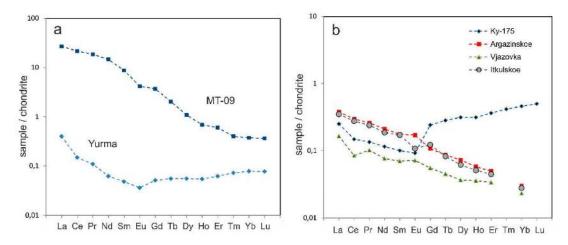


Figure 10. Chondrite-normalized rare earth element (REE) distribution patterns of quartzite (a) and hydrothermal vein quartz (b) (normalization according to data of Anders and Grevesse [22].

Three of the hydrothermal quartz samples (Argazinskoe, Vjasovska, Itkulskoje) are similar both in absolute REE values and in their chondrite-normalized REE patterns, which correspond to the common crustal distribution (Figure 10b). Only a slight negative Ce anomaly (Vjazovka) and negative (Itkulskoe) or positive (Argazinskoe, Vjazovka) Eu anomalies are detectable. Quartz Ky-175 shows comparable LREE patterns but steeply increasing HREE (Figure 10b), which is most likely caused by zircon or xenotime micro-inclusions.

Summarizing, the "bulk" solution ICP-MS provides concentrations of lattice-bound trace elements plus concentrations of elements bound in mineral and fluid micro-inclusions, which could not be removed during sample preparation.

In situ LA-ICP-MS: Element concentrations determined by in situ LA-ICP-MS are generally lower than those determined with solution ICP-MS, except Ge, Ti and Li (Tables S1 and S3). This is mainly due to the fact that during laser ablation the analyses of visible (>0.5 μ m) micro-inclusions can be avoided by choosing clear, inclusion free ablation areas. Thus, concentrations measured by LA-ICP-MS reflect almost the values of lattice-bound trace elements.

Aluminium concentrations analysed by LA-ICP-MS are consistently low (<15 ppm) for all samples except sample Vjazovka (from 21 to 32 ppm). Titanium has more variable concentrations (compared with its general abundance in quartz, e.g., [5]), ranging from <1 ppm to 37 ppm. Lithium concentrations are very low in all samples (<2.3 ppm). Boron and Ge were also found in low concentrations, except in the sample Argazinskoe, which has up to 5.3 ppm B and 1.6 ppm Ge. The Berkutinskaya sample (pegmatite quartz) has high P concentrations, of up to 7.6 ppm.

Minerals 2017, 7, 189 12 of 19

4. Discussion

4.1. Trace Element Incorporation Into Quartz

The applied combination of CL, EPR and ICP-MS methods permits the identification of types of structural defects and provide insights into their incorporation and/or transformation mechanisms during quartz crystal genesis. In addition, the results provide first indications concerning the very low trace-element concentrations and show the potential of the sampled quartz deposits for high-purity applications in the industry. These data are essential for the prediction of theoretical limits of the processing procedure, assuming that impurities from mineral and fluid inclusions could be minimized or completely removed during refinements.

Figure 11 shows the concentrations of Al and Ti measured by laser ablation ICP-MS (LAICP-MS) and the field defining the quartz economically as high-purity quartz (HPQ) in accordance with Harben [3] and Müller et al. [4]. It can be concluded that all quartz samples except MT-09 plot into the HPQ field. The best chemical quality is of quartz of the hydrothermal veins at Kyshtym (Ky-175) and Itkulskoe.

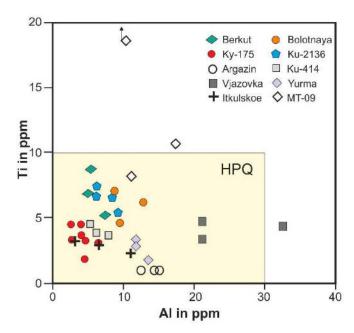


Figure 11. Ti and Al concentrations from laser ablation inductively-coupled plasma mass spectrometry (LA-ICP-MS) analyses of the quartz samples plotted into the field of high-purity quartz (HPQ) according to Harben [3] and Müller et al. [4].

Some elements (Ge, Ti, Li) show more or less constant concentrations when comparing the data from solution ICP-MS analyses of bulk quartz and LA-ICP-MS measurements of selected inclusion-free areas. For these elements it can be concluded that they are preferentially incorporated in the quartz structure. Because of the very low concentrations of these elements no EPR signals were detectable for potential paramagnetic defects.

In contrast to the above mentioned elements, Al concentrations measured by LA-ICP-MS are much lower than those analysed in the bulk quartz by ICP-MS. Although the EPR data show that the paramagnetic $[AlO_4]^0$ centre is the most frequent in the investigated quartz; not all of the Al measured by solution ICP-MS seems to be structurally bound. The paramagnetic $[AlO_4]^0$ centre and its diamagnetic precursors $[AlO_4/M^+]^0$ play an important role as imperfections in quartz. The monovalent

Minerals 2017, 7, 189 13 of 19

ions H^+ , Li^+ , Na^+ commonly charge-compensate the Al defects. However, Na (together with other alkali and alkali earth elements) seems to be mainly related to fluid inclusions (see Figure 9) and the Li content is low in all samples. Data from literature show that hydrothermal quartz mineralization and pegmatite quartz often contain elevated concentrations of Li [23], and Li is a common charge-balancing cation for Al [24]. The data of the present study, however, indicate that the charge compensator of Al^{3+} substituting Si^{4+} is predominantly H^+ . This is in accordance with the results of Miyoshi et al. [25] who detected a preferred incorporation of H^+ as the charge-balancing cation of Al defects in hydrothermal quartz. Müller et al. [26] have already shown that igneous quartz preferentially incorporates H^+ as a charge-balancing cation in lieu of Li, K and Na. Similar findings have been made more recently for pegmatite quartz [27,28].

Although the comparison of EPR and trace-element data reveals a general trend of an increasing number of paramagnetic Fe centres with increasing contents of chemically measured Fe concentrations (with the exception of sample MT-09), there are nevertheless variations in the absolute values. The differences could be explained by two different facts. First, Fe-bearing micro-inclusions are the reason for elevated Fe concentrations in the bulk quartz samples. This is especially true for sample MT-09, where a couple of mineral inclusions (e.g., mica) have been detected by microscopy. Second, Fe is known to occur as both Fe^{2+} and Fe^{3+} in quartz [15,29]. However, Fe^{2+} is not detectable by EPR at X-band frequencies [14]. Therefore, 1:1 correlations of the Fe^{3+} EPR signal with the total Fe contents from chemical analyses are not expected.

4.2. Cathodoluminescence and Structural Defects

Characteristic luminescence colours of quartz with different geological history, and associated spectral CL measurements together with the results from the EPR spectroscopy provided information about the defect structures and incorporated trace elements, primary growth conditions, and processes of secondary overprint. These features not only influence the properties and quality of the potential quartz raw material, but also allow insights into the genetic history of the quartz occurrences.

According to Ramseyer and Mullis [30] and Götze et al. [31] the activation of the visible greenish-blue CL of the pegmatite quartz from Berkutinskaya is associated with cation compensated trace-element centres in the quartz structure. The intensity of the luminescence emission falls off rapidly after electron bombardment within 30–60 s, which can be related to ionization-enhanced diffusion of luminescence centres as was shown by Ramseyer and Mullis [30] with electro-diffusion experiments. However, the absolute concentration of Al in this sample is low (<10 ppm). This is confirmed by the low abundance of paramagnetic trace-element defects of Al, Ti and Ge. Also, the contents of Li and other cations are far below the common abundance of such elements in pegmatite quartz [24,31]. The heterogeneous CL textures of grains indicate a heterogeneous distribution of trace elements responsible for the CL (Figure 3b). Only areas with higher intensity (brighter CL) of the transient CL point to elevated contents of responsible trace elements (e.g., Al, Li). Moreover, a possible role of H⁺ for the 500-nm luminescence signal must be taken into consideration.

All hydrothermal quartz samples show a characteristic short-lived blue CL, which is elicited by two main emission bands at ~390 nm and 500 nm. According to Ramseyer and Mullis [30] and Perny et al. [32] these luminescence bands are activated by cation-compensated [AlO $_4$ /M $^+$]-centres in the quartz structure. The strong decrease of these emission bands during electron irradiation is due to the interaction of the cation-balanced Al centres with the electron beam and indicates elevated trace element contents in areas with high CL intensity [30,33] (Figure 4b). Such heterogeneous pattern is depicted in the quartz from Vjazovka (compare Figure 3d), which has an elevated concentration of Al compared to the other samples but shows no remarkable EPR signal for the [AlO $_4$] 0 centre.

The relatively low contents of Al and charge-balancing cations in some of the investigated hydrothermal quartz suggest that either the $[AlO_4/M^+]$ defects are effective CL activators (i.e., even low abundance of $[AlO_4/M^+]$ can activate the characteristic CL), or that other activators exist for this specific luminescence. Gorton et al. [34] found the typical short-lived blue CL in synthetic

Minerals 2017, 7, 189 14 of 19

quartz with extremely low impurity concentrations and concluded that probably other activators than $[AlO_4/M^+]$ -defects might be additionally responsible for the blue CL. However, the EPR measurements in the present study did not provide any indication for other luminescence-active paramagnetic defects. EPR measurements revealed an almost complete absence of intrinsic lattice defects associated with oxygen or silicon vacancies (e.g., the E' centre, O_2^{3-} centre), and even the abundance of paramagnetic trace-element defects of Al, Ti, Ge is in general low.

Areas of dull CL in hydrothermal quartz can be the result of post-crystallization overprint. For instance, the interaction of migrating fluids with the host quartz left their traces in trails of reduced CL intensity (Figure 3d). Van den Kerkhof and Hein [35] explained this phenomenon with the loss of trace elements during recrystallization of the interacting area with the fluids. Decreased luminescence intensities were also detected along grain boundaries. This can probably be related to the opening of fluid inclusions and the migration of inherited fluids (especially along grain boundaries).

Indications of secondary overprint and deformation are also visible in features of apparent dislocation planes (Figure 3f). Supplementary electron back scattered diffraction (EBSD) measurements provided evidence of Dauphine twinning, which is preferentially initiated by mechanical deformation. In addition, these analyses revealed low-angle tilting of sub-grains due to deformation (Figure 12).



Figure 12. SEM forescattered image showing low-angle tilting of sub-grains due to deformation in the hydrothermal quartz from Kyshtym (Ky-175).

The quartz samples from Kuznechikhinsk (Ku-414, Ku-2136) illustrate that deformation of hydrothermal quartz resulted in a general decrease of the luminescence intensity and a homogenization of the CL pattern. This fact can probably be related to healing of defects and reduction of trace-element impurities due to recrystallization and reorganization processes of the quartz lattice. Measured trace-element contents are low (e.g., Al < 10 ppm, Ti < 2 ppm, Li ~1 ppm) and even the detected intensities of paramagnetic defects of Al and Fe as well as vacancy-related defects are very low.

Minerals 2017, 7, 189 15 of 19

The visible CL colour of both metamorphically overprinted hydrothermal quartz and quartzite is dark blue, and the spectra are dominated by two bands at 450 and 650 nm, respectively (Figure 4c,d). The typical luminescence emission bands at 390 nm and 500 nm that were detected in the hydrothermal quartz samples are missing. The emission observed at ~450 nm is associated with O-deficiency centres (ODC) in quartz [36,37]. It can be related to the recombination of the self-trapped exciton (STE), which involves an irradiation-induced oxygen Frenkel pair consisting of an oxygen vacancy and a peroxy linkage [38].

The 650-nm emission is attributed to non-bridging oxygen-hole centres (NBOHC), which are formed from different precursor defects [39,40]. A number of different precursors of this NBOHC have been proposed, such as H- or Na-impurities, peroxy linkages (O-rich samples), or strained Si-O bonds [38]. The time dependent spectra reveal an increase of the 650 nm band under the electron beam, which points to a conversion of precursor centres into the NBOHC. Considering the mechanical deformation of the samples, strained Si-O bonds may result in bond breaking during electron bombardment and thus, in the formation of NBOHC and the related increase of the 650-nm emission band.

Another conspicuous CL feature is the orientation-dependent CL behaviour that was observed in the hydrothermal quartz from Kyshtym (sample Ky-175; Figure 5). The initial blue CL colour of quartz sub-grains cut perpendicular to the crystallographic c-axis turned into a red-violet CL colour during electron irradiation (due to increasing 650-nm emission intensity). Surprisingly, sub-grains with other orientations do not show the same effect and only the intensity of the initial blue CL decreases (strong decline of the 450-nm emission band).

It cannot be ruled out that the crystallographic orientation of the crystals influences the interaction with the electron beam due to the relatively open structural channels along the c-axis of the quartz lattice. An alignment of the c-axis along the microscope axis would than provide a more intensive interaction with the electron beam, i.e., an increased conversion of precursor centres of the NBOHC associated with a stronger increase of the 650-nm emission. Another explanation is probably the influence of polarization effects of the luminescence light. Walderhaug and Rykkje [41] compared c-axis orientations of quartz grains and related CL colours and found clear indications that the observed colour variations are a function of crystallographic orientation. They concluded that this might be due to selective absorption of light along different crystallographic directions, a phenomenon well known from spectroscopy. Sippel [42] reported similar effects of the quartz CL when observing the luminescence under a nicol prism. The quartz CL showed strong polarization effects with variations of the CL colour from red to blue through a rotating polarizer. He found that the blue oscillators are aligned with the c-axis, whereas the red emission is unpolarized. Such a behaviour might explain the observed colour variations in the investigated quartz sample Ky-175. The effect may be interpreted by anisotropic luminescing centres that have oriented the oscillation in a strong internal crystal field.

4.3. Genetic Implications for the Formation of High-Purity Quartz

The investigated quartz localities in the northern Ural were all formed during multiple metamorphism and related deformation. According to Kelman [9], silica mobilization and formation of quartz veins and bodies can especially be related to the retrograde stage of the two metamorphic events. Although quartz from the different locations may originate from varying processes, all types show in general low concentrations of trace elements and low abundance of other point defects. Elevated trace-element contents in several samples can unambiguously be related to micro-inclusions (e.g., samples MT-09, Ku-2136).

The low abundance of structural point defects such as E'_1 centres in the quartz samples investigated requires a combination of the following two conditions: (1) low intrinsic structural imperfection (i.e., low oxygen and silicon vacancies); and (2) weak natural irradiation. This fact implies that there was sufficient time for crystallization under more or less equilibrium conditions during the formation of these quartz occurrences. On one hand, the metamorphic processes caused

Minerals 2017, 7, 189 16 of 19

the mobilization of silica-rich fluids (hydrothermal veins) and melts (pegmatite), and the precipitation as high-purity quartz. On the other hand, recrystallization, healing of defects or disintegration of fluid inclusions under metamorphic conditions resulted in a natural "purification" of the pre-existing quartz crystals and a lowering of trace-element contents. Larson et al. [43] and Müller et al. [5] found that Li concentrations in quartz can be reduced during recrystallization, and Al contents may both decrease or increase depending on the specific environment. Germanium and Ti seem to be more or less unchanged.

The formation of such metamorphic mobilisates appears to be an appropriate process for the formation of HPQ deposits. Compared with data from the literature, the analysed absolute trace-element concentrations as well as chondrite-normalized REE distribution patterns are similar to those of metamorphic and hydrothermal quartz from other regions [44]. Even the pegmatite quartz from Berkutinskoe (Berkut) follows this trend, with atypical very low concentrations of characteristic elements for pegmatite quartz such as Al, Ge or Li.

The REE patterns mostly show a crustal signature indicating a source of the silica from mobilization processes of crustal material. Only the hydrothermal quartz from Kyshtym (Ky-175) has elevated concentrations of HREE. This unusual pattern is most likely caused by zircon or xenotime micro-inclusions.

In conclusion, the results of the present study show a strong link between metamorphic processes and formation of quartz bodies of high purity. If the quartz bodies are large enough and the abundance of pre- and syn-genetic micro-inclusions is low, they may represent potential HPQ deposits.

5. Conclusions

The investigation of quartz samples of different genetic types (hydrothermal, pegmatite, and quartzite) from 10 localities in the Southern Ural region (Russia) using an analytical combination of CL microscopy and spectroscopy, EPR spectroscopy, and bulk as well as spatially resolved trace-element analysis, proved to characterize the type and abundance of trace elements and structural defects in quartz, and reconstruct processes responsible for their formation. In situ LA-ICP-MS analysis showed cumulative trace-element concentrations of <50 ppm with <30 ppm Al and <10 ppm Ti for almost all samples, defining the quartz economically as high-purity quartz. EPR data confirmed the low abundances of substitutional Ti and Fe and showed Al to be the only significant trace element structurally bound in the investigated quartz samples. Elevated concentrations of selected trace elements that were analysed with "bulk" solution ICP-MS could be related to mineral (Ti, Al, Fe, Mn, Mg, K, Zr, U, Th, Hf) and fluid (Na, K, Rb, Ca, Mg, Sr) micro-inclusions.

CL imaging reveals a heterogeneous distribution of luminescence centres, i.e., varying amounts of activator trace elements in the quartz grains. Hydrothermal and pegmatite quartz exhibit a distinct short-lived greenish-blue CL with main CL emission bands at ~390 and 500 nm, which can be attributed to [AlO₄/M⁺] (M = H, Li, Na, K) defects. Low contents of Li, Na and K indicate that H⁺ is the main charge-balancing cation of Al³⁺-related defects. Accordingly, areas with bright greenish-blue CL could be related to higher abundances of the [AlO₄/M⁺] defects. Moreover, an orientation-dependent behaviour of the CL during electron irradiation was observed that can be related to anisotropy effects of the crystal lattice, which results in an orientation-dependent interaction with the electron beam and the selective absorption of emitted light along different crystallographic directions.

Certain features of alteration, recrystallization/reorganization as well as trails of fluid migration revealed by CL in the quartz samples can be related to metamorphism-related deformation. All quartz bodies were formed during retrograde stages of complex metamorphic processes, resulting in silica mobilization and formation of quartz veins and lenses. Deformation of hydrothermal quartz resulted in a general decrease of the luminescence intensity and a homogenization of the CL pattern. This feature can probably be related to healing of defects and reduction of trace-element impurities due to recrystallization and reorganization processes of the quartz lattice. The geochemical and spectroscopic data demonstrate that the formation of such metamorphic mobilisates is an appropriate process for

Minerals 2017, 7, 189

the formation of high-purity quartz (HPQ) deposits. Also, the quartz occurrences formed prior to the metamorphic events (pegmatite, quartzites) were suggestively purified during regional metamorphism and deformation, resulting in a high-purity quartz province in the Southern Urals.

Supplementary Materials: The following are available online at www.mdpi.com/2075-163X/7/10/189/s1, Table S1: Trace-element concentrations of investigated quartz samples analysed by solution ICP-MS (results in ppm), Table S2: REE concentrations (results in ppm) and chondrite-normalized interelemental ratios of investigated quartz samples analysed by solution ICP-MS, Table S3: Results of spatially resolved trace-element analyses by LA-ICP-MS (in ppm).

Acknowledgments: We gratefully acknowledge analytical efforts by G. Bombach (Freiberg) and B. Flem (Trondheim) during trace-element analyses as well as G. Nolze (Berlin) for EBSD measurements. M. Magnus and G. Geyer (Freiberg) are thanked for their help with sample preparation.

Author Contributions: Jens Götze and Elena Kotova conceived and designed the experiments; Elena Kotova provided the sample material; Jens Götze, Yuanming Pan, Axel Müller, Elena Kotova, and Daniele Cerin performed the experiments; Jens Götze, Yuanming Pan and Axel Müller analysed the data; Jens Götze wrote the paper.

Conflicts of Interest: The authors declare no conflict of interest.

References

- Heaney, P.J.; Prewitt, C.T.; Gibbs, G.V. Silica—Physical Behaviour, Geochemistry and Materials Application. In Reviews in Mineralogy; Mineralogical Society of America: Washington, DC, USA, 1994; Volume 29, p. 606, ISBN 0-939950-35-9.
- Götze, J.; Möckel, R. Quartz: Deposits, Mineralogy and Analytics; Springer: Berlin/Heidelberg, Germany, 2012; p. 360, ISBN 978-3-642-22161-3.
- Harben, P.W. The Industrial Mineral Hand Book—A Guide to Markets, Specifications and Prices, 4th ed.; Industrial Mineral Information: London, UK, 2002; p. 412, ISBN 978-1900663519.
- Müller, A.; Ihlen, P.M.; Wanvik, J.E.; Flem, B. High-purity quartz mineralisation in kyanite quartzites, Norway. Miner. Depos. 2007, 42, 523–535. [CrossRef]
- Müller, A.; Wanvik, J.E.; Ihlen, P.M. Petrological and chemical characterization of high-purity quartz deposits with examples from Norway. In *Quartz: Deposits, Mineralogy and Analytics*, 1st ed.; Götze, J., Möckel, R., Eds.; Springer: Berlin/Heidelberg, Germany, 2012; pp. 71–118.
- Müller, A.; Ihlen, P.M.; Snook, B.; Larsen, R.; Flem, B.; Bingen, B.; Williamson, B.J. The chemistry of quartz in granitic pegmatites of southern Norway: Petrogenetic and economic implications. *Econ. Geol.* 2015, 110, 137–157. [CrossRef]
- Götze, J. Chemistry, textures and physical properties of quartz—Geological interpretation and technical application. *Mineral. Mag.* 2009, 73, 645–671. [CrossRef]
- 8. Melnikov, E.P. Main controlled factors of localization of the granulated quartz in the Southern part of the Ufaleisky anticlinorium. In *Vein Quartz of the Eastern Hang of the Urals*; Melnikov, E.P., Melnikova, N.I., Eds.; Nedra: Moscow, Russia, 1970; Issue No. 80, pp. 41–50. (In Russian)
- 9. Kelman, G.A. Migmatite Complexes of the Mobile Belt; Nedra: Moscow, Russia, 1974; p. 191. (In Russian)
- Neuser, R.D.; Bruhn, F.; Götze, J.; Habermann, D.; Richter, D.K. Kathodolumineszenz: Methodik und Anwendung. Zent. Geol. Paläontologie Teil I 1995, H1, 287–306.
- Monecke, T.; Bombach, G.; Klemm, W.; Kempe, U.; Götze, J.; Wolf, D. Determination of trace elements in the quartz reference material UNS-SpS and in natural quartz samples by ICP-MS. Geostand. Newsl. 2000, 24, 73–81. [CrossRef]
- Flem, B.; Müller, A. In situ analysis of trace elements in quartz using Laser ablation inductively coupled plasma mass spectrometry. In Quartz: Deposits, Mineralogy and Analytics, 1st ed.; Götze, J., Möckel, R., Eds.; Springer: Berlin/Heidelberg, Germany, 2012; pp. 219–236.
- Müller, A.; Wiedenbeck, M.; Flem, B.; Schiellerup, H. Refinement of phosphorus determination in quartz by LA-ICP-MS through defining new reference material values. Geostand. Geoanal. Res. 2008, 32, 361–376. [CrossRef]
- 14. Weil, J.A. EPR of iron centers in silicon dioxide. Appl. Magn. Reson. 1964, 6, 1-16. [CrossRef]
- Sivaramaiah, G.; Lin, J.; Pan, Y. Electron paramagnetic resonance spectroscopy of Fe³⁺ ions in amethyst: Thermodynamic potentials and magnetic susceptibility. *Phys. Chem. Miner.* 2011, 38, 159–167. [CrossRef]

Minerals 2017, 7, 189

 Weil, J.A. A review of electron spin resonance and its applications to the study of paramagnetic defects in crystalline quartz. Phys. Chem. Miner. 1984, 10, 149–165. [CrossRef]

- Nilges, M.J.; Pan, Y.; Mashkovtsev, R. Radiation-damage-induced defects in quartz. I. Single-crystal W-band EPR study of hole centers in an electron-irradiated quartz. Phys. Chem. Miner. 2008, 35, 221–235. [CrossRef]
- Pan, Y.; Nilges, M.J.; Mashkovtsev, R.I. Radiation-indiced defects in quartz. II. Single-crystal W-band EPR study of a natural citrine quartz. Phys. Chem. Miner. 2008, 35, 387–397. [CrossRef]
- Mashkovtsev, R.I.; Pan, Y. Nature of paramagnetic defects in α-quartz: Progresses in the First Decade of the 21st Century. In New Developments in Quartz Research: Varieties, Crystal Chemistry and Uses in Technology; Novak, B., Marek, P., Eds.; Nova Science Publishers: Hauppauge, NY, USA, 2013; pp. 65–104.
- Walsby, C.J.; Lees, N.S.; Claridge, R.F.C.; Weil, J.A. The magnetic properties of oxygen-hole aluminum centres in crystalline SiO₂. VI: A stable AlO₄/Li centre. Can. J. Phys. 2003, 81, 583–598. [CrossRef]
- Botis, S.M.; Pan, Y. First-principles calculations on the [AlO₄/M⁺]⁰ (M = H, Li, Na, K) defects in quartz and crystal-chemical controls on the uptake of Al. Mineral. Mag. 2009, 73, 537–550. [CrossRef]
- Anders, E.; Grevesse, N. Abundances of the elements: Meteoritic and solar. Geochim. Cosmochim. Acta 1989, 53, 197–214. [CrossRef]
- Blankenburg, H.-J.; Götze, J.; Schulz, H. Quarzrohstoffe; Deutscher Verlag für Grundstoffindustrie: Leipzig-Stuttgart, Germany, 1994; p. 296.
- Götze, J.; Plötze, M.; Graupner, T.; Hallbauer, D.K.; Bray, C. Trace element incorporation into quartz: A combined study by ICP-MS, electron spin resonance, cathodoluminescence, capillary ion analysis and gas chromatography. Geochim. Cosmochim. Acta 2004, 68, 3741–3759. [CrossRef]
- Miyoshi, N.; Yamaguchi, Y.; Makino, K. Successive zoning of Al and H in hydrothermal vein quartz. Am. Mineral. 2005, 90, 310–315. [CrossRef]
- Müller, A.; Koch-Müller, M. Hydrogen speciation and trace element contents of igneous, hydrothermal and metamorphic quartz from Norway. *Mineral. Mag.* 2009, 73, 569–583. [CrossRef]
- 27. Baron, M.A.; Stalder, R.; Konzett, J.; Hauzenberger, C.A. OH-point defects in quartz in B- and Li-bearing systems and their application to pegmatites. *Phys. Chem. Miner.* 2015, 42, 53–62. [CrossRef]
- Frigo, C.; Stalder, R.; Hauzenberger, C.A. OH defects in quartz in granitic systems doped with spodumene, tourmaline and/or apatite: Experimental investigations at 5-20 kbar. Phys. Chem. Miner. 2016, 43, 717–723.
 [CrossRef]
- 29. Di Benedetto, F.; Innocenti, M.; Tesi, S.; Romanelli, M.; D'Acapito, F.; Fornaciai, G.; Montegrossi, G.; Pardi, L.A. A Fe K-edge XAS study of amethyst. *Phys. Chem. Miner.* **2010**, *37*, 283–289. [CrossRef]
- Ramseyer, K.; Mullis, J. Factors influencing short-lived blue cathodoluminescence of alpha-quartz. Am. Mineral. 1990, 75, 791–800.
- Götze, J.; Plötze, M.; Trautmann, T. Structure and luminescence characteristics of quartz from pegmatites. Am. Mineral. 2005, 90, 13–21. [CrossRef]
- 32. Perny, B.; Eberhardt, P.; Ramseyer, K.; Mullis, J.; Pankrath, R. Microdistribution of Al, Li, and Na in α-quartz: Possible causes and correlation with short-lived cathodoluminescence. *Am. Mineral.* **1992**, 77, 534–544.
- Götze, J.; Plötze, M.; Habermann, D. Cathodoluminescence (CL) of quartz: Origin, spectral characteristics and practical applications. *Mineral. Petrol.* 2001, 71, 225–250. [CrossRef]
- Gorton, N.T.; Walker, G.; Burley, S.D. Experimental analysis of the composite blue CL emission in quartz. J. Lumin. 1996, 72–74, 669–671.
- 35. Van den Kerkhof, A.M.; Hein, U.F. Fluid inclusion petrography. Lithos 2001, 55, 27-47. [CrossRef]
- Skuja, L. Optically active oxygen-deficiency-related centers in amorphous silicon dioxid. J. Non-Cryst. Solids 1998, 239, 16–48. [CrossRef]
- Pacchioni, G.; Ierano, G. Optical absorption and nonradiative decay mechanism of E' centre in silica. Phys. Rev. Lett. 1998, 81, 377–380. [CrossRef]
- Stevens-Kalceff, M.A.; Phillips, M.R. Cathodoluminescence microcharacterization of the defect structure of quartz. Phys. Rev. B 1995, 52, 3122–3134. [CrossRef]
- Siegel, G.H.; Marrone, M.J. Photoluminescence in as-drawn and irradiated silica optical fibers: An assessment
 of the role of non-bridging oxygen defect centres. J. Non-Cryst. Solids 1981, 45, 235–247. [CrossRef]
- Stevens-Kalceff, M.A. Cathodoluminescence microcharacterization of point defects in α-quartz. Mineral. Mag. 2009, 73, 585–606. [CrossRef]

Minerals 2017, 7, 189

41. Walderhaug, O.; Rykkje, J. Some Examples of the Effect of Crystallographic Orientation on the Cathodoluminescence Colors of Quartz. J. Sediment. Res. 2000, 70, 545–548. [CrossRef]

- Sippel, R.F. Luminescence petrography of the Apollo 12 rocks and comperative features in terrestrial rocks and meteorites. In *Lunar and Planetary Science Conference Proceedings*; The M.I.T. Press: Cambridge, MA, USA; Volume 1, pp. 247–263.
- 43. Larsen, R.B.; Henderson, I.; Ihlen, P.M.; Jacamon, F. Distribution and petrogenetic behavior of trace elements in granitic quartz from South Norway. *Contrib. Mineral. Petrol.* **2004**, *147*, *615–628*. [CrossRef]
- Monecke, T.; Kempe, U.; Götze, J. Genetic significance of the trace element content in metamorphic and hydrothermal quartz: A reconnaissance study. Earth Planet. Sci. Lett. 2002, 202, 709–724. [CrossRef]



© 2017 by the authors. Licensee MDPI, Basel, Switzerland. This article is an open access article distributed under the terms and conditions of the Creative Commons Attribution (CC BY) license (http://creativecommons.org/licenses/by/4.0/).

中文译文

俄罗斯南 Ural 地区高纯石英的微量元素组成及 缺陷结构

摘 要:对来自俄罗斯南 Ural 地区 10 个不同产地的石英样品进行了微量元素组成及缺陷结构研究。通过阴极发光(CL)显微镜和光谱、电子顺磁共振(EPR)光谱以及电感耦合等离子体质谱(ICP-MS)的综合分析,发现几乎所有的石英样品均表现出极低的微量元素含量(总浓度<50ppm,Al<30ppm,Ti<10ppm)和低丰度的顺磁性缺陷,经济地将其定义为适用于高科技应用的"高纯度"石英(HPQ),EPR 和 CL 数据证实了替代的 Ti 和 Fe 丰度较低,并表明 Al 是所研究的石英样品中唯一与结构结合的重要微量元素。CL 显微成像揭示了发光中心(如 Al)的异质分布以及变形与再结晶特征。研究表明,在逆行变质过程中,与变形有关的再结晶和重组过程造成的缺陷愈合导致 CL 活化剂和其他微量元素的低浓度或空位,这是研究区域形成 HPQ 矿床的主要驱动过程。

关键词: 石英; 阴极发光; 电子顺磁共振; 微量元素

1. 引言

石英及其他硅酸盐矿物是地壳中最重要的造岩矿物之一,也是重要的工业原料。由于他们的丰度以及物理化学特性,天然二氧化硅原料具有广泛的工业和技术应用。

尤其是杂质元素总浓度低于 50ppm 的高纯石英 (HPQ),由于较高的经济价值,其价格比低质量的二氧化硅原料高出 20 倍。高纯度石英对高科技行业具有重要的战略意义,用于制造单晶硅生长坩埚 (太阳能电池板与微芯片生产)、高温灯管、通信设备、光学元件及半导体材料。随着全球需求增长,HPQ 矿床的勘探活动日益增多。

由于石英材料中杂质元素的浓度极低(0.1 到 50ppm),这一特性使其特殊的质量要求分析面临挑战。天然二氧化硅材料,尤其是石英,具有特定的特性,包括晶格缺陷、杂质元素丰度、再结晶程度等,这是区域地质历史和相关特定形成条件的结果。因此,遗传条件和石英特性之间的相互关系不仅可以用于地质过程的重建,还可用于矿床位置和质量的预测,也可用于特定的工业应用。特别是,有关缺陷数量和类型的信息对于原材料的加工和潜在的技术应用非常重要。

本研究介绍了对俄罗斯南 Ural 地区 10 个地点不同成因的潜在 HPQ 矿床进行的综合矿物学和地球化学研究的结果。该研究旨在获取这些石英材料的晶格缺

陷类型和丰度以及杂质元素的详细信息,以确定导致 HPQ 矿床形成的关键过程和条件。这一目标是通过结合多种高灵敏度分析技术来实现的,这些技术包括阴极发光(CL)显微镜和光谱、电子顺磁共振(EPR)光谱以及通过电感耦合等离子体质谱(ICP-MS)和激光烧蚀 ICP-MS 进行的微量元素分析。

2. 材料与方法

2.1 地质背景和样品材料

研究样品采自南 Ural 地区 Chelyabinsk 西北部 10 个不同地点的潜在高纯度 石英(图 1,表 1)。样品材料包括来自伟晶岩的石英、热液石英脉、构造变形和部分再结晶的热液石英,以及来自两个石英岩矿床的石英。

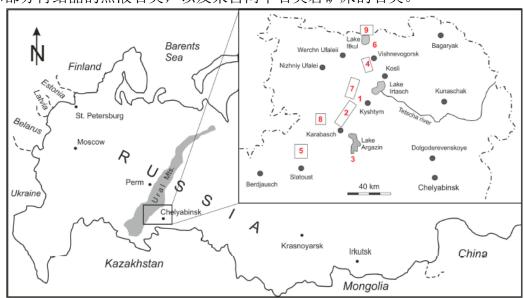


图 1. 南 Ural 地区 Chelyabinsk 西北部调查的石英矿床地形示意图;

- 1—Berkutinskaya(Berkut),2—Kyshtym(sampleKy-175),3—Argazinskoe(Arg),
- 4—Vjasovka(Vja),5—Itkulskoe(Itkul),6—Bolotnaya(Bol),7—Kuznechikhinsk(Ku-414,Ku-2136),8—Yurmaridge(Yur),and9—Taganairidge(MT-09)

数字与表 1 中的位置和石英类型有关

表 1. 南 Ural 地区 (俄罗斯) 的石英样品

| 位置 | 类型 | 样品 |
|------------------|------------|---------|
| 1.Berkutinskaya | 伟晶岩 | Berkut |
| 2.Kyshtym | 热液矿脉 | Ky-175 |
| 3.Argazinskoe | 热液矿脉 | Arg |
| 4.Vjasovka | 热液矿脉 | Vja |
| 5.Itkulskoe | 热液矿脉 | Itkul |
| 6.Bolotnaya | 热液矿脉 | Bol |
| 7.Kuznechikhinsk | 热液矿脉, 变质叠印 | Ku-414 |
| 7.Kuznechikhinsk | 热液矿脉, 变质叠印 | Ku-2136 |
| 8. Yurma ridge | 石英岩 | Yur |

9. Taganai ridge

石英岩

MT-09

所有石英体均产于 Ufalei 变质岩复合体内。该杂岩由两个叠覆的构造-变质单元组成。下部单元为 Ufalei 组的上元古界高度变质岩,构成背斜层核心。热液脉矿床(Kyshtym 样品 Ky-175、Kuznechikhinsk 样品 Ku-414 与 Ku-2136、Argazinskoe 样品 Arg)及 Yurma 山脊与 Taganai 山脊(样品 MT-09)的石英岩体均位于该单元内(表 1)。Berkutinskaya 矿床的伟晶岩体位于 Kyschtym 附近的Berkut 山脊。上部单元由奥陶系与下泥盆片状陆源沉积岩组成,环绕背斜层核心分布,包含 Vjazovka、Bolotnaya 和 Itkulskoe 等热液脉矿床。

所有石英体都是在 Ural 地区长期多级的变质作用中形成的。调查地区的变质作用可分为两个主要阶段: (1)晚寒武纪阶段,该阶段与 Ufalei 背斜层的形成有关,并细分为两个子阶段——进行变质的早期阶段与逆行变质作用; (2)中古生代阶段,其特征是片麻岩芯和片岩框架的变质转变。热液石英脉与石英体的硅迁移和形成可能与这两种变质作用的逆行阶段有关。

2.2 分析方法

使用热阴极 CL 显微镜 HC1-LM 对碳涂层薄片进行 CL 显微镜和光谱分析。该系统在 14kV 和 0.2mA(电流密度~10μA/mm)下使用散焦电子束运行。在 CL 操作期间使用 Peltier 冷却数字摄像机(OLYMPUSDP72,OLYMPUS Deutschland GmbH,Hamburg,Germany)捕获发光图像。使用 Acton ResearchSP-2356 数字三光栅光谱仪和 PrincetonSpec-10 电荷耦合器件(CCD)检测器记录 370-920nm 波长范围内的 CL 光谱,该探测器通过二氧化硅-玻璃纤维导向装置连接到 CL 显微镜。在标准化条件下测量 CL 光谱(通过 Hg 卤素灯进行波长校准,光斑宽度30μm,测量时间 5s)。进行了辐照实验以记录电子辐照下的石英样品。样品在恒定条件下(14kV,0.2mA)辐照 5 分钟,开始和之后每隔 1 分钟测量一次光谱。

使用布鲁克 EMX 波谱仪(Bruker Corporation,Billerica,MA,USA)通过 EPR 波谱研究石英粉末样品的顺磁中心,该波谱仪在室温和液氮温度下以 X 波段微波频率运行。室温 EPR 的实验条件包括~9.63GHz 的微波频率、100kHz 的调制频率、0.1mT 的调制幅度以及 0.02mW 至 20mW 的微波功率。对于宽扫描 50-6500mT,光谱分辨率为~0.146mT,对于窄扫描 300-350mT,光谱分辨率为 0.024mT。室温 EPR 测量后的所有样品在室温下在 Co 电池中以~10kGy 的剂量照射。在伽马射线照射后立即进行低温(85K)EPR 测量,除微波频率为~9.39GHz 外,室温分析使用类似的实验条件。

首先使用溶液 ICP-MS 分析散装石英样品(溶解粉末)的化学成分。使用预清洁的玛瑙砂浆将用于 ICP-MS 分析的样品(400–500mg)研磨成<30μm 的晶粒尺寸。粉末状样品在含 5mL 浓 HF 和 3mL 浓 HNO₃ 的玻璃碳容器中消化,温度

为 50°C (35 分钟)。Re 溶液 (1mL100µg·L)作为 ICP-MS 测量的内标。使用 Perkin Elmer Sciex Elan5000 四极杆仪器(Percin ElmerInc.,Baesweiler,Germany)以及 错流雾化器和 rhyton 雾化室进行分析。通过分析玻璃砂参考材料 UNS-SpS 来评估 ICP-MS 测量的精密度和准确度。大多数分析的相对标准偏差低于 10%。ICP-MS 结果显示程序检测限范围为 $0.22\mu g \cdot L^{-1}$ 至 $3.1\mu g \cdot L^{-1}$ 代表 Na、Mg、Al、K、Ca和 Ba。Li、Mn 和 Sr 等元素的程序检测限范围为 0.02 至 $\mu g \cdot L^{-1}$,而其他被调查元素的检测限为 1 至 7 μ g \bullet L^{-1} 。

此外,还制备了样品的 200 µm 抛光厚切片,用于激光烧蚀电感耦合等离子 体质谱(LA-ICP-MS),以原位测定单个石英晶体的微量元素。使用双聚焦扇形 场质谱仪 ELEMENT XR 与 New Wave 193-nm 准分子激光探针(Thermo Scientific) 联用分析了 Li、Be、B、Na、Al、P、K、Ca、Ti、Mn、Fe、Ge、Rb、Sr、Ga 和 Sb 的浓度。激光器的脉冲频率为 20Hz, 速度为 $15 \,\mu\,\text{m} \cdot \text{s}^{-1}$, 光斑尺寸为 $50 \,\mu\,\text{m}$, 样品表面的能量通量为 5-7mJ·cm⁻²。光栅消融应用于大约 150μ m× 300μ m 的 区域。消融深度约为 50 µm。将烧蚀材料运输到 ICP-MS 的载气是 He 与 Ar 混 合。使用美国国家标准与技术研究所生产的三种硅酸盐玻璃参考材料 (NISTSRM610、612 和 614) 进行外部校准。此外,还使用了 NISTSRM 1830 钠 钙浮法玻璃(0.1%m/mAl₂O₃)、德国联邦材料研究与测试研究所的认证参考材料 BAM No.1 非晶硅玻璃,以及德国哥廷根中心(GZG)的 Andreas Kronz 提供的 Oz-Tu 合成纯石英单晶。每次测量包括对每种同位素的 15 次扫描,测量时间从 高分辨率的 K 的 0.15 秒/扫描到低分辨率的 Li 的 0.024 秒/扫描不等。线性回归 模型(包括不同参考材料的多次测量)用于定义每个元素的校准曲线。为了计算 P浓度,采用了Müller等的程序。对Qz-Tu合成纯石英单晶进行了10次连续测 量,以估计检测限。分析误差范围在元素绝对浓度的10%以内。

3. 结果

3.1 阴极发光(CL)

CL 成像揭示了石英样品中的异质性、晶内微观结构和微包裹体。检测到的 微包裹体包括 Bolotnaya 样品中的碳酸盐(橙色 CL)、样品 Ku-2136 中的长石(微 斜长石一亮蓝色 CL, 钠长石一蓝紫色 CL),以及样品 MT-09 中的锆石/独居石 (亮辐射晕) 和云母 (无发光)(图 2)。

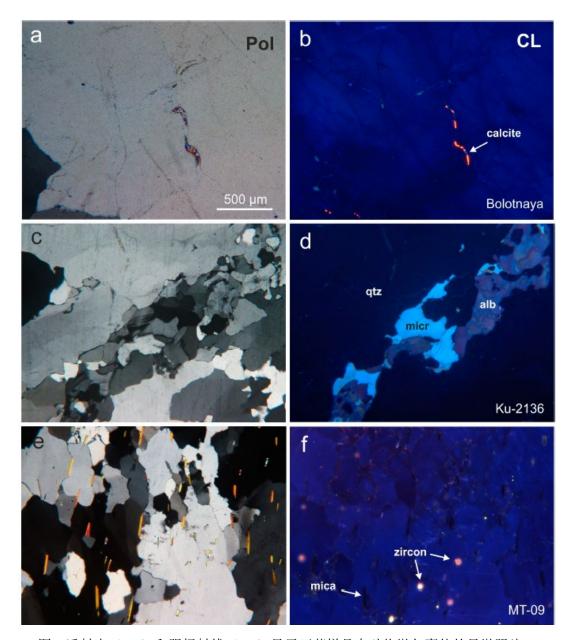


图 2.透射光(Pol)和阴极射线(CL)显示石英样品中矿物微包裹体的显微照片: (a, b)热液石英中的方解石(Bolot); (c, d) Kuznechikhins 的变质叠印热液石英中的微细长石 (micr)和白云石(alb)(Ku-2136); (e, f)云母(不发光)和锆石的辐射晕,Taganai 山脊石英岩中的辐射晕(MT-09)

微包裹体可能与主岩(如热液碳酸盐脉)成分或变质岩的赋存物质有关。几乎所有样品的石英颗粒都检测到异质性,而在偏振光下这些石英颗粒看起来是均质的。此外,CL可以揭示蚀变和再结晶/重组的特征以及流体迁移的痕迹(图 3)。

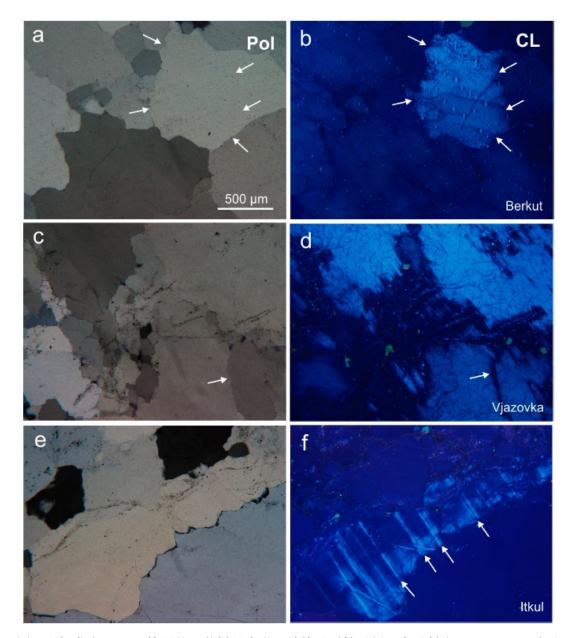


图 3.阴极发光(CL)检测的石英样品中微观结构异质性示例,在透射光(Pol)下几乎不可见: (a, b) 来自 Berkutinskaya(Berkut)的伟晶岩石英中明亮的亚晶粒区域; (c, d) 由于 Vjazovka(Vja)热液石英中流体迁移而导致 CL 强度降低的轨迹(箭头); (e, f) 来自 Itkulskoe(Itkul)的热液石英中的位错面

伟晶岩石英呈现均匀的蓝绿色 CL, 在大约 500nm 处具有特征性的 CL 发射带 (图 4a)。强 CL 的亚晶粒区域 (图 3b) 具有 500nm 波段的最高强度,表明与发光相关的缺陷数量最高。在电子辐照下,500nm 波段的发射强度会强烈下降。电子轰击 5 分钟后得到的 CL 光谱由 450nm 的发射带和 650nm 的弱发射带组成 (图 4a)。

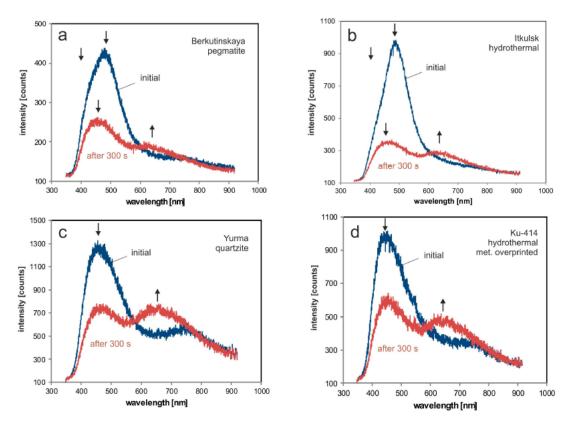


图 4.不同来源石英的代表性 CL 发射光谱 (初始光谱为蓝色、电子辐照 5 分钟后为红色): (a)伟晶岩石英; (b)热液矿脉石英; (c)石英岩; (d)构造变形和部分再结晶的热液矿脉石英

热液矿脉中的石英显示出典型的短寿命蓝色 CL。最初的光谱主要由波长为500nm 的一个强波段和波长为390 nm 的发射波段组成。由于所使用设备的光谱透射率(玻璃光学元件对光谱紫外线区域的吸收),该发射带只能以肩的形式出现(见图4b中的箭头)。电子辐照5min后的CL光谱分别以450nm和650nm的发射带为主。在大多数热液石英样品中,CL成像的一个显著特点是异质模式(图3d)。强发光区域与低CL强度区域交替出现。迁移流体与主石英的相互作用在CL强度降低的区域留下了痕迹(图3d)。此外,在初始电子辐射过程中变形特征清晰可见,但在电子轰击过程中,变形特征就会消失。

随着热液石英变形程度的增加,发光强度降低,可见的 CL 颜色变得更加均匀。未变形热液石英在 390nm 和 500nm 处的典型发光发射带缺失。变形热液石英的光谱分别由 450nm 和 650nm 的两个波段主导(图 4d)。

在 CL 下,石英岩样品通常呈非均质性,并且可能包含可能来自原生岩的矿物微包裹体(样品 MT-09;图 2e, f)。Yurma 的石英岩不含任何可见的矿物包裹体,代表着高纯度材料。石英岩样品中的石英的特征是深蓝色 CL, 在 450nm 和650nm 处显示发射带(图 4c)。

在 Kyshtym 的热液石英中观察到 CL 在电子照射过程中的方向依赖性行为 (Ky-175, 图 5)。垂直于 c 轴切割成薄片的亚晶粒 (在偏振光下较暗)显示初始

蓝色 CL 颜色变为红紫色(650nm 波段的增加),而具有其他取向的亚晶粒仅显示初始蓝色 CL 的减小(复合蓝色发射带减小)。

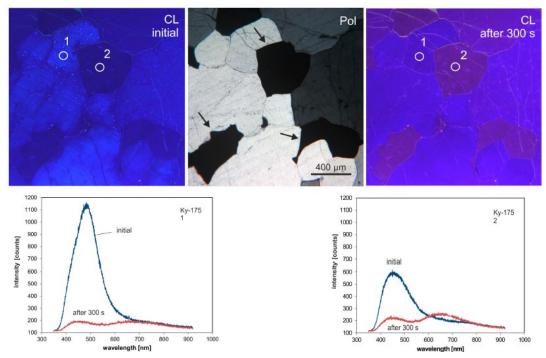


图 5.来自 Kyshtym 的热液石英(Ky-175)的阴极发光(CL)和透射光(交叉极性-Pol)的显微照片;图像和相关光谱显示了初始 CL 和电子照射 5min 后的 CL。注意不同晶体取向的石英亚晶粒的不同 CL 表现;垂直于晶体学 c 轴切割的亚晶粒(见箭头)具有较低的初始蓝色 CL 强度,并且由于电子轰击而产生微红色的 CL(650nm 发射带)

3.2. 电子配位共振(EPR)

图 6 和图 7 显示了在室温下测量的所有石英样品的 EPR 光谱。除了在有效 g 值约为 4.38 时存在微量的菱形 Fe³⁺信号外, EPR 光谱基本上没有其他特征 (图 6)。

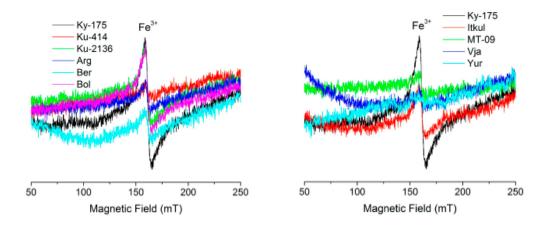


图 6.在室温下采集的石英样品的电子顺磁共振(EPR)光谱。显示在 geff=4.38 处有微弱的 菱形 Fe³⁺信号;强度以任意单位表示

显然,该信号的强度在所有样本中都很低,并且在样本之间是可变的。很明

显,在Berkutinskaya (伟晶岩)、Argazinskoe、Vjasovka (热液矿脉)、Ku-414 (变质叠印热液石英)、MT-09 和 Yurma (石英岩) 样品中,Fe³⁺信号非常小。Fe³⁺信号在样品 Ky-175、Itkulskoe、Bolotnaja (热液矿脉) 和 Ku-2136 (变质叠印热液石英)中略高。

图 7 中的光谱显示了中心磁场区域的共振信号。同样,所有光谱都具有低信噪比。事实上,在~2.00 的有效 g 值下,不存在任何辐射诱导缺陷,即使是普通的 E'1 也极为罕见。值得一提的是作为样品容器的二氧化硅管显示出非常微弱的 E'1 信号,这导致测量光谱中的 E'1 信号较弱(图 7)。

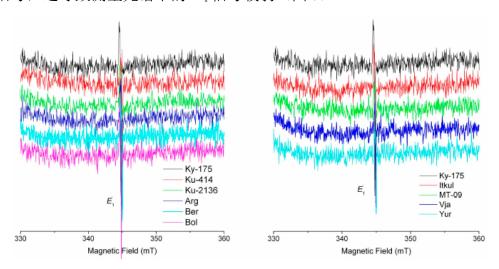


图 7.研究的石英样品在室温下的 EPR 波谱显示轻微的 E'1, 但在 geff=2.0 时通常不存在其他 辐射诱导缺陷

在 85K 温度下测量的伽马射线辐照样品的 EPR 光谱均显示存在不同数量的 众所周知的[AlO4]⁰, 具有特征性的 Al 超精细结构(图 8)。石英中的顺磁性[AlO4]⁰ 中心已被证明是由中性的[AlO4/M⁺]⁰(M=H、Li、Na、K)前驱体形成。图 8 比较了以 Ky-175 样品作为共同参考的各个光谱。样品 Ky-175 作为公共参考。样品 Argazinskoje、Bolotnaya 和 Yurma 测得的[AlO4]⁰ 信号强度明显高于其他样品。

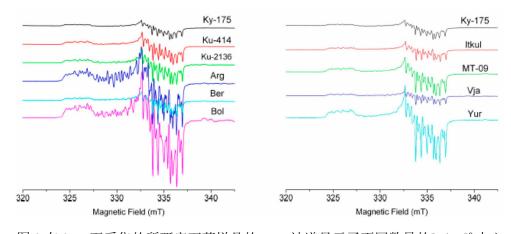


图 8.在 85K 下采集的所研究石英样品的 EPR 波谱显示了不同数量的[AlO₄]⁰中心

在 85K 下测得的 EPR 波谱再次显示 Fe 和 E'_1 中心的存在,但通常不存在 Ti 和 Ge 相关缺陷,具有诊断性的 Ti、Ti 和 Ge 超精细结构,证实了在室温下观察 到的结果。

3.3. 微量元素

表 S1 和 S2 汇总了通过溶液 ICP-MS 测定得出的结果。数据表明,与天然石英的平均浓度相比,大多数石英样品中的大多数微量元素浓度较低。铝浓度通常低于 100ppm,Fe 和 Ti 的浓度低于 10ppm。一个例外是来自 Taganai 山脊的石英岩(样品 MT-09),该石英岩的 Al、K、Mg、Ti、Fe、Mn、Zr、U、Th 和 Hf 的浓度较高。根据显微镜分析,Al、K、Mg、Ti、Fe 和 Mn 浓度升高是由云母的微包裹体引起的,而 Zr、U、Th 和 Hf 的浓度是由锆石引起的(图 2e,Kuznechikhinsk的石英(样品 Ku-2136—K、Na、Al 和 Fe)中的长石(钠长石、微斜长石——图2d)以及 Bolotnaja 样品(样品 Bolot——Ca、Mg 和 Fe)中的碳酸盐(图 2b)的微夹杂物也有类似的影响。

钠、Sr、K、Mg和Rb在不同样品中呈正相关(图9)。这些碱和碱土元素的丰度主要与流体包裹体的存在有关,尽管长石和云母的矿物微包裹体(例如,样品 MT-09、Ku-2136)也会影响这些相关性。然而,在大多数研究的石英中没有检测到矿物包裹体。

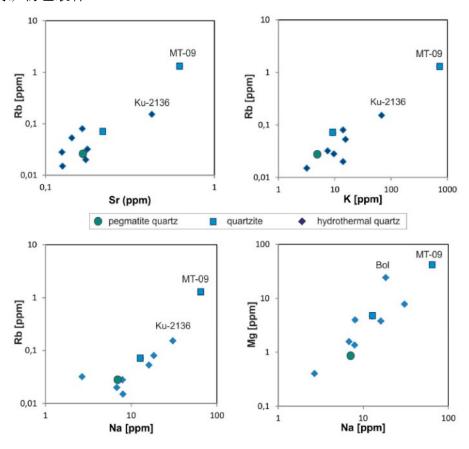


图 9.研究的石英样品中选定的碱元素和碱土元素的元素比例(标记的样品是那些检测到矿物夹杂物的样品)

表 S2 列出了稀土元素(REE)的浓度,如图 10 所示。在一些样品(Berkutinskaya、Bolotnaya、Ku-414 和 Ku-2136)中,某些稀土元素的浓度低于 ICP-MS 分析法的检测限,因此,图 10 中没有显示它们。两个石英岩样本的 REE 分布图与热液石英的分布图不同。特别是石英岩样本 MT-09 的 REE 绝对浓度较高,具有富集轻REE(LREE)和重 REE(HREE)的典型地壳特征(图 10a)。富集的 REE 很可能与该样品中发现的微包裹体有关。Yurma 的石英岩的 REE 含量要低得多,但显示出类似的 LREE 模式。然而,HREE 略微富集。

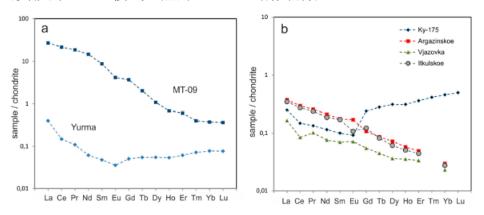


图 10.石英岩的稀土元素(REE)规范化分布模式(a)热液矿脉石英(b)(根据 Anders 和 Grevesse 的数据规范化

其中三个热液石英样品(Argazinskoe、Vjasovska、Itkulskoje)在绝对 REE 值和 REE 规范化分布模式上都相似,这与常见的地壳分布相对应(图 10b)。只能检测到轻微的阴性 Ce 异常(Vjazovka)和阴性(Itkulskoe)或阳性(Argazinskoe,Vjazovka)Eu 异常。石英 Ky-175 显示出类似的 LREE 模式,但 HREE 急剧增加(图 10b),这很可能是由锆石或微包裹体引起的。

总而言之,ICP-MS 提供晶格结合微量元素的浓度以及矿物和液体微包裹体中结合的元素浓度,这些元素在样品制备过程中无法去除。

原位 LA-ICP-MS:除 Ge、Ti 和 Li 外,原位 LA-ICP-MS 测定的元素浓度通常低于溶液 ICP-MS 测定的元素浓度(表 S1 和 S3)。这主要是因为在激光烧蚀过程中,通过选择清晰、无夹杂物的烧蚀区域,可以避免对可见(>0.5μm)微夹杂物的分析。因此,通过 LA-ICP-MS 测量的浓度几乎反映了晶格结合微量元素的值。

通过 LA-ICP-MS 分析的所有样品的铝浓度始终较低(<15ppm),样品 Vjazovka (从 21 到 32ppm)除外。钛的浓度变化更大,范围从<1ppm 到 37ppm。 所有样品中的锂浓度都非常低(<2.3ppm)。 硼和锗的浓度也很低,但样品 Argazinskoe 除外,其 B 含量高达 5.3ppm,Ge 含量高达 1.6ppm。Berkutinskaya

样品(伟晶岩石英)的P浓度很高,高达7.6ppm。

4.讨论

4.1 石英中的微量元素

将 CL、EPR 和 ICP-MS 三种方法结合使用,可以确定石英中微量元素的结构缺陷类型,并深入了解它们在石英晶体形成过程中的掺入和/或转化机制。此外,结果提供了有关极低微量元素浓度的初步迹象,并显示了采样石英矿床在工业中高纯度应用的潜力。这些数据对于预测加工过程的理论极限至关重要,假设在精炼过程中可以最大限度地减少或完全去除矿物和液体夹杂物中的杂质。

图 11 显示了通过激光烧蚀 ICP-MS(LAICP-MS)测量的铝和钛浓度,以及根据 Harben 和 Müller 等人经济地将石英定义为高纯度石英(HPQ)的领域。可以得出结论,除 MT-09 外,所有石英样品都属于高纯度石英。化学质量最好的是 Kyshtym(Ky-175)和 Itkulskoe 的热液矿脉的石英。

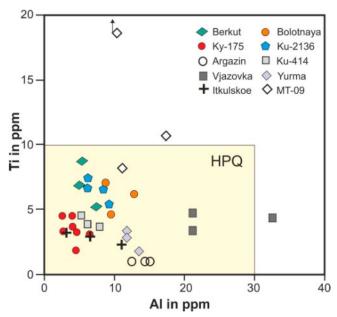


图 11.根据 Harben 和 Müller 等人对石英样品进行激光烧蚀电感耦合等离子体质谱(LA-ICP-MS)分析的 Ti 和 Al 浓度

在比较块状石英的溶液 ICP-MS 分析数据与选定无夹杂物区域的 LA-ICP-MS 测量数据时,一些元素(Ge、Ti、Li)显示出或多或少的恒定浓度。对于这些元素,可以得出结论,它们优先掺入石英结构中。由于这些元素的浓度非常低,因此无法检测到潜在的顺磁缺陷的 EPR 信号。

与上述元素相反,LA-ICP-MS 测量的 Al 浓度远低于 ICP-MS 在块石英中测量的 Al 浓度。尽管 EPR 数据显示顺磁性[AlO₄]⁰ 中心在所研究的石英中最为常见;但并非所有通过 ICP-MS 测量的 Al 都是结构结合的。顺磁[AlO₄]⁰ 中心及其抗

磁前驱体[AlO₄/M+]⁰ 在石英中作为缺陷起着重要作用。一价离子 H、Li、Na 通常对 Al 缺陷进行电荷补偿。然而,Na(以及其他碱和碱土元素)似乎主要与流体包裹体有关(见图 9),并且所有样品中的 Li 含量都很低。文献数据显示,热液石英矿化和伟晶岩石英通常含有高浓度的 Li,而 Li 是 Al 的常见电荷平衡阳离子。然而,本研究的数据表明,Al 取代 Si⁴⁺的电荷补偿器主要是 H⁺。这与 Miyoshi等人的研究结果一致,在热液石英中检测到 H⁺作为 Al 缺陷的电荷平衡阳离子的优先结合。Müller 等已经表明,火成石英优先掺入 H⁺作为电荷平衡阳离子来代替 Li、K 和 Na。最近对伟晶岩石英也有类似的发现。

尽管 EPR 和微量元素数据的比较揭示了顺磁性 Fe 中心数量的总体趋势,即随着化学测量的 Fe 浓度的增加(样品 MT-09 除外),顺磁性铁中心的数量绝对值仍然存在变化。这些差异可以用两个不同的事实来解释。首先,含铁的微包裹体是块状石英样品中 Fe 浓度升高的原因。对于样品 MT-09 尤其如此,因为通过显微镜检测到了一些矿物夹杂物(例如云母)。其次,已知 Fe 同时以 Fe²⁺和 Fe³⁺的形式在石英中存在。然而,EPR 在 X 波段频率下无法检测到 Fe²⁺。因此,Fe³⁺EPR信号与化学分析得出的总 Fe 含量之间不可能存在 1:1 的相关性。

4.2. 阴极发光和结构缺陷

具有不同地质历史的石英的特征发光颜色,以及相关的光谱 CL 测量和 EPR 波谱的结果,提供了有关缺陷结构和掺入微量元素、初级生长条件和二次 叠印过程的信息。这些特征不仅影响潜在石英原料的特性和质量,而且还有助于 深入了解石英矿床的遗传历史。

根据 Ramseyer 和 Mullis 以及 Götze 等人的研究,来自 Berkutinskaya 的伟晶岩石英可见的蓝绿蓝色 CL 的活化与石英结构中的阳离子补偿微量元素中心有关。电子轰击后,发光发射的强度在 30-60s 内迅速下降,这可能与发光中心的电离增强扩散有关,如 Ramseyer 和 Mullis 在电扩散实验中所示。然而,该样品中Al 的绝对浓度很低(<10ppm)。Al、Ti 和 Ge 的顺磁性微量元素缺陷的低丰度证实了这一点。此外,Li 和其他阳离子的含量远低于伟晶岩石英中此类元素的常见丰度。晶粒的异质 CL 纹理造成 CL 的微量元素的异质分布(图 3b)。只有瞬时CL 强度较高(CL 较亮)的区域表明相关微量元素(例如 Al、Li)的含量较高。此外,必须考虑 H⁺对 500nm 发光信号的可能作用。

所有热液石英样品都显示出特征性的短寿命蓝色 CL,这是由~390nm 和500nm 的两个主要发射带引起的。根据 Ramseyer 和 Mullis 以及 Perny 等人的研究,这些发光带被石英结构中的阳离子补偿[AlO₄/M+]⁰中心激活的。在电子辐照过程中,这些发射带的强烈衰减是由于阳离子平衡的 Al 中心与电子束的相互作用所致,这表明在 CL 强度高的区域,微量元素含量较高(图 4b)。Vjazovka 石

英(对比图 3d)中也显示了这种异质模式。与其他样品相比,它的 Al 浓度更高,但 [AlO₄]⁰中心没有显示出明显的 EPR 信号。

在一些研究的热液石英中,Al 和电荷平衡阳离子的含量相对较低,这表明 [AlO₄/M+]⁰ 缺陷是有效的 CL 活化剂(即低丰度的[AlO₄/M+]⁰ 也可以激活特征 CL),或者这种特定发光还存在其他活化剂。Gorton 等在合成中发现了典型的短寿命蓝色 CL 石英具有极低的杂质浓度,并得出结论,可能除[AlO₄/M+]⁰ 缺陷之外的其他活化剂可能是导致蓝色 CL 的原因。然而,本研究中的 EPR 测量没有为其他发光活性顺磁性缺陷提供任何指示。EPR 测量显示,几乎完全不存在与氧或硅空位相关的固有晶格缺陷,甚至 Al、Ti、Ge 的顺磁性微量元素缺陷的丰度也普遍较低。

热液石英中暗淡的 CL 区域可能是结晶后叠印的结果。例如,迁移流体与主石英的相互作用在 CL 强度降低的位置中留下了痕迹(图 3d)。Van den Kerkhof和 Hein 解释这种现象是由于与流体相互作用区域再结晶过程中微量元素的损失造成的。沿晶界还检测到发光强度降低。这可能与流体包裹体的打开和遗传流体的迁移(尤其是沿晶界)有关。

在明显的位错平面特征上也可以看到二次叠印和变形的迹象(图 3f)。补充性电子背散射衍射(EBSD)测量提供了 Dauphine 孪晶的证据,它优先由机械变形引发。此外,这些分析还揭示了亚晶粒因变形而产生的低角度倾斜(图 12)。

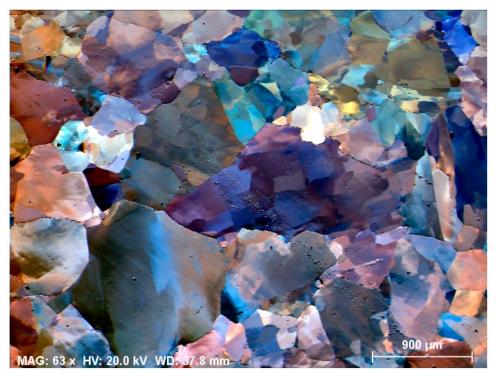


图 12.SEM 前散射图像显示,由于 Kyshtym(Ky-175)热液石英的变形,亚晶粒出现小角度倾斜

来自 Kuznechikhinsk 的石英样品(Ku-414、Ku-2136)表明, 热液石英的变

形导致发光强度普遍降低,CL 图案趋于均匀。这可能与由于石英晶格的再结晶和重组过程而导致的缺陷愈合和微量元素杂质的减少有关。测得的微量元素含量很低(例如,Al<10ppm,Ti<2ppm,Li~1ppm),甚至检测到的 Al 和 Fe 顺磁性缺陷以及空位相关缺陷的强度也非常低。

变质叠印热液石英和石英岩的可见 CL 颜色均为深蓝色,光谱分别由 450nm 和 650nm 的两个波段主导(图 4c、d)。在热液石英样品中检测到典型 390nm 和 500nm 发光发射带缺失。在~450nm 处观察到的发射与石英中的 O 缺陷中心(ODC) 有关。这可能与自捕获激子(STE)的重组有关,该激子涉及由氧空位和过氧键组成的辐照诱导的氧 Frenkel 对。

650nm 的发射归因于非桥接氧空穴中心 (NBOHC),它由不同的前驱体缺陷组成。人们提出了许多不同的 NBOHC 前体,例如 H-或 Na-杂质、过氧键 (富含O的样品)或应变的 Si-O键。随时间变化的光谱显示在电子束的作用下,650nm波段有所增加,这表明前驱体中心转化为 NBOHC。考虑到样品的机械变形,应变的 Si-O键可能会在电子轰击过程中导致键断裂,,从而导致 NBOHC 的形成和650nm 发射带的相关增加。

另一个明显的 CL 特征是在 Kyshtym 热液石英 (Ky-175 样品;图 5)中观察到的取向依赖性 CL 行为。垂直于晶体学 c 轴切割的石英亚晶粒最初呈蓝色,但在电子辐照过程中(由于 650nm 发射强度的增加),其 CL 颜色变成了紫红色。令人惊讶的是,其他取向的子晶粒并没有表现出同样的效果,只有初始蓝色 CL的强度下降 (450nm 发射带的强度下降)。

由于石英晶格的 c 轴具有相对开放的结构通道,因此不能排除晶体的晶向会影响与电子束的相互作用。如果 c 轴沿显微镜轴线排列,则与电子束的相互作用会更加强烈,即 NBOHC 前驱体中心的转化率会提高,同时 650nm 波长的发射也会增强。另一种解释是光的偏振效应的影响。Walderhaug 和 Rykkje 比较了石英晶粒的 c 轴取向和相关的 CL 颜色,发现有明确迹象表明颜色变化是晶体取向的函数。这可能是由于沿不同晶体学方向对光的选择性吸收造成的,这是光谱学中众所周知的现象。Sippel 在尼科尔棱镜下观察石英 CL 的发光时,也发现了类似的效果。石英 CL 显示出强烈的偏振效应,通过旋转偏振器,CL 颜色从红色变为蓝色。他发现蓝色振子与 c 轴对齐,而红色发射则是非偏振的。这种行为可能解释了在所研究的石英样品 Ky-175 中观察到的颜色变化。这种效应可解释为各向异性发光中心在强大的内部晶体场中定向振荡。

4.3. 高纯度石英的地质成因

Ural 北部石英矿区都是在多次变质作用和相关变形过程中形成的。根据 Kelman 的说法,硅的移动和石英脉及石英体的形成尤其与两次变质作用的逆行 阶段有关。尽管来自不同位置的石英可能源于不同的过程,但所有类型的石英普遍显示出低浓度的微量元素和其他点缺陷的低丰度。一些样品中微量元素含量较高,可能与微包裹体(如样品 MT-09、Ku-2136)相关。

在所研究的石英样品中,E'1 中心等结构点缺陷的丰度较低,这需要以下两个条件的共同作用: (1) 低内部结构缺陷(即低氧和硅空位); (2) 弱自然辐照。这一事实意味着在这些石英矿点的形成过程中,有足够的时间在大致平衡的条件下进行结晶。一方面,变质过程导致富含二氧化硅的流体(热液矿脉)和熔体(伟晶岩)的移动并沉淀为高纯度石英。另一方面,变质条件下的再结晶、缺陷愈合或流体包裹体的解体导致了原有石英晶体的自然"净化"和微量元素含量的降低。Larson等人和 Müller 等人发现,石英中的 Li 含量在再结晶过程中会降低,而 Al 含量则会根据具体环境的不同而降低或增加。Ge 和 Ti 的含量基本保持不变。

这种变质移动体的形成似乎是高纯度石英矿床形成的适当过程。与文献数据相比,所分析的微量元素绝对浓度以及规范化的 REE 分布模式与其他地区的变质石英和热液石英相似。即使是来自 Berkutinskoe (Berkut) 的伟晶岩石英也遵循这一趋势,伟晶岩石英的特征元素(如 Al、Ge 或 Li)的浓度非常低。

REE 模式大多显示地壳特征,表明二氧化硅的来源是地壳物质的移动过程。 只有来自 Kyshtym (Ky-175)的热液石英具有较高的 HREE 浓度。这种不寻常的 模式很可能是由锆石或包裹体造成的。

总之,本研究结果表明,变质过程与高纯度石英体的形成之间存在密切联系。如果石英体足够大,且前生和同生微包裹体的丰度较低,则可能代表潜在的高纯度石英矿床。

5. 结论

对来自南 Ural 地区 10 个地方的不同成因类型(热液岩、伟晶岩和石英岩)的石英样品进行了调查,采用了 CL 显微镜和光谱分析、EPR 光谱分析以及空间分辨微量元素分析的组合,证明了石英中微量元素和结构缺陷的类型和丰度特征,并重建了其形成过程。原位 LA-ICP-MS 分析表明,几乎所有样品中的微量元素累积浓度都小于 50ppm,其中 Al 小于 30ppm,Ti 小于 10ppm,这些石英在经济上被定义为高纯度石英。EPR 数据证实了取代 Ti 和 Fe 的低丰度,并表明 Al 铝是所研究的石英样品中唯一在结构上结合的重要微量元素。用溶液 ICP-MS 分析的某些微量元素浓度升高可能与矿物(Ti、Al、Fe、Mn、Mg、K、Zr、U、Th、Hf)和流体(Na、K、Rb、Ca、Mg、Sr)微包裹体有关。

CL 成像揭示了发光中心的异质分布,即石英颗粒中不同数量的活化剂微量元素。热液石英和伟晶岩石英表现出明显的短寿命绿蓝色 CL,主要 CL 发射带

位于~390 和 500nm 处,这可归因于[AlO₄/M+]⁰(M=H, Li, Na, K)缺陷。Li、Na 和 K 含量低表明 H⁺是 Al³⁺相关缺陷的主要电荷平衡阳离子。因此,具有亮绿蓝色 CL 的区域可能与[AlO₄/M+]⁰ 缺陷的丰度较高有关。此外,在电子照射过程中观察到 CL 的取向依赖性行为,这可能与晶格的各向异性效应有关,这种效应导致与电子束的取向依赖性相互作用以及沿不同晶体学方向对发射光的选择性吸收。

石英样品中 CL 揭示的蚀变、再结晶/重组的某些特征以及流体迁移的痕迹可能与变质作用相关的变形有关。所有石英体都是在复杂变质过程的逆行阶段形成的,导致硅移动并形成石英脉和晶体。热液石英的变形导致发光强度普遍降低和 CL 均匀化。这一特征可能与由于石英晶格的再结晶和重组过程引起的缺陷愈合和微量元素杂质的减少有关。地球化学和光谱学数据表明,这种变质移动产物的产生是形成高纯度石英(HPQ)矿床的适当过程。此外,变质事件之前形成的石英矿床(伟晶岩、石英岩)在区域变质和变形过程中被提纯,从而在南 Ural 地区形成了一个高纯度石英矿区。